Physics | Lancaster University

Quantum Control of the Electronic and Thermal properties of Fullerenes and Exohedral Fullerenes

By

Nasser Majed S Almutlaq

B.Sc., M.Sc.

July 2017

A thesis Submitted in part fulfilment for the degree of Doctor of Philosophy at Lancaster University

UK

Declaration

Except where stated otherwise, I hereby declare that the thesis is my own work and has not been submitted in substantially the same form for the award of a higher degree elsewhere. Where other sources of information have been used, they have been acknowledged. This thesis' results and documents work carried out between July 2012 and June 2016 at Lancaster University.

Nasser Majed Sallal Almutlaq

July 2017

Abstract

In recent years, driven by the need to downsize to the molecular level, advances in technology has made the manufacture of nanoscale devices possible. In this thesis I will investigate the theoretical electronic and thermal properties of a carbon based class of nanoscale materials by examining the possibility of using fullerenes and decachlorofullerenes as building blocks towards viable molecular scale devices. In particular I have looked at ways to enhance the electronic communication between fullerenes through introducing exohedral varients, which I found to have a positive effect on the electronic and thermoelectric properties. The methods used in this work are based on density functional theory, combined with quantum transport calculations using Greens functions.

Fullerenes are promising building blocks for nano-scale electronics, as they have relatively large spherical surface area and are geometrically symmetric. If fullerene-based thermoelectricity is to become a viable technology, then fullerenes exhibiting both positive and negative Seebeck coefficients will be needed and therefore I also calculate the thermoelectric properties of the naturally occurring fullerene C60 known as the buckyball together with an exohedral example namely C50Cl10.

C_{60} is known to have a negative Seebeck coefficient of S which varies in the range of -18 to -23 $\mu V/K$ and therefore in this thesis I address the challenge of identifying a fullerene with a positive-Seebeck-coefficient. I investigated the thermoelectric properties of single-molecule junctions of the exohedral fullerene $C_{50}Cl_{10}$ connected to gold electrodes and found that it has a positive Seebeck coefficient. Furthermore, in

common with C_{60}, the Seebeck coefficient can be increased by placing more than one $C_{50}Cl_{10}$ in series.

For a single $C_{50}Cl_{10}$, I find S=+8 µV/K and for two $C_{50}Cl_{10}$'s in series I find S=+30 µV/K. I also find that the $C_{50}Cl_{10}$ monomer and dimer have power factors of 0.5×10^{-5} W/m.K^2 and 6.0×10^{-5} W/m.K^2 respectively. These results demonstrate that exohedral fullerenes could provide a new class of thermoelectric materials with desirable properties, which complement those of all-carbon fullerenes, thereby enabling the boosting of the thermovoltage in all-fullerene tandem structures.

I calculate the structural and electronic and thermoelectrics properties of carbon nanotube peapods. In contrast with carbon-only peapods, the magnitude of this effect is sensitive to the orientation and spacing of the fullerenes and exohedral fullerenes as a consequence, a rotation or translation of the $C_{50}Cl_{10}$ can cause the zero-bias electrical conductance to switch, as a result of that the new possibilities of engineering the transport properties of carbon nanotube peapods.

Acknowledgements

Contents

Chapter 1

1.1. Introduction

Carbon is an element which can form a number of different allotropes ranging from amorphous to crystalline. Diamond and fullerenes are common allotropic forms which are purely crystalline in nature. Carbon is the sixth element of the periodic table and listed as the first element at the top of column IV and its name came originally from Latin carbo which means coal and its symbol is C. It is the fourth most abundant chemical element in the universe by mass after hydrogen, helium, and oxygen. Each carbon atom has six electrons; the first two electrons occupy the *1s* orbital revolving around nucleus which has six protons and six neutrons. They are strongly bound electrons whereas the remaining four are valence electrons in the next energetic orbitals which are *2s, 2p* are more weakly bound , as shown in Figure1.1[1,2]. Carbon atoms with sp^2-hybridisation (for more information about carbon *sp*-hybridisation see [1]) will form either fullerenes (zero-dimension), carbon nanotubes CNT (one-dimension), graphene (two-dimensions) or graphite and diamond (three-dimensions) [2,4].
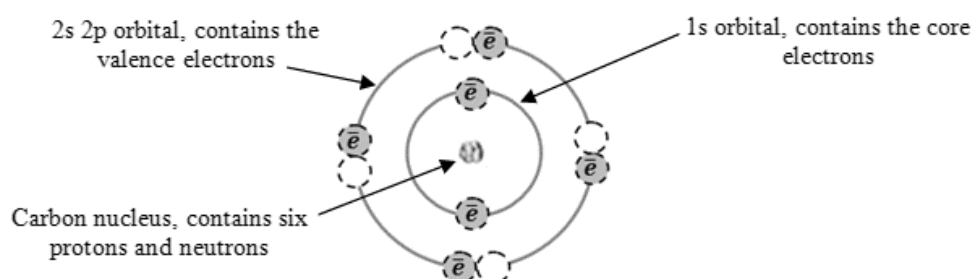
Figure 1.1 Carbon atom which has six electrons, two electrons in 1s orbital which are called core electrons and the rest four electrons occupied the 2s 2p orbital which called valence electrons.

Carbon has received a huge interest due to the discovery and synthesis of fullerenes and the subsequent identification of carbon nanotubes and graphene, which has led to intensive experimental and theoretical studies making this field of research one of the most exciting areas in materials science [5,6,7,8].

Using geometry to fold a graphene sheet one can produce the atomic structure of the fullerenes and carbon nanotubes studied in this thesis and therefore I will now give a short introduction to graphene.

Graphene

Graphene is an sp^2-hybridised state of carbon and the valence electrons occupy the $2s^2$ and $2p^2$ orbitals which form covalent bonds [9]. The formation of sp^2 hybridised bonds is illustrated in Figure 1.1a below.

$$S \qquad p_x + p_y \qquad sp^2 \qquad p_z$$
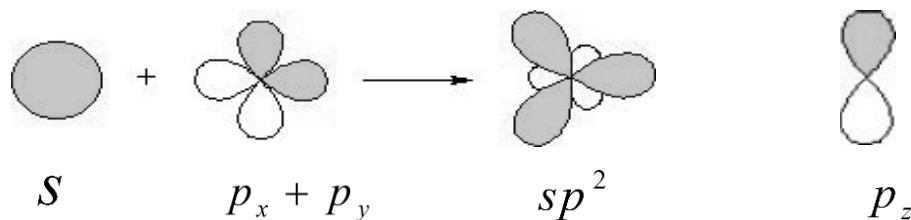
Figure 1.1a The shape of the sp^2-hybridised orbitals.*[1]*

The wave functions of the outer electrons can mix with each other and the occupation of *2s²* and *2p²* orbitals leads to the formation of covalent bonds forming between the carbon atoms.

Graphene has revealed some unique electric and physical properties since it was isolated in 2004, for instance high mobility of carriers at room temperature and potential for a wide range of applications. Graphene is a single layer of carbon atoms which can form a two-dimensional honeycomb crystal structure (hexagonal lattice) [9].

The graphene lattice

Graphene has a honeycomb lattice represented in Figure 1.2 using a ball-and-stick model. The balls represent carbon atoms and the sticks symbolize the σ-bonds between atoms. The carbon-carbon bond length is approximately $a_{C-C} \approx 1.42$ Å. The honeycomb lattice can be characterized as a Bravais lattice with a basis of two atoms, indicated as A and B in Figure 1.2, and these contribute a total of two π electrons per unit cell to the electronic properties of graphene. The underlying Bravais lattice is a hexagonal lattice and the primitive unit cell can be considered an equilateral parallelogram with side $a = \sqrt{3}\, a_{C-C} = 2.46$ Å. The primitive unit vectors as defined in Figure 1.4 are

$$a_1 = \left(\frac{\sqrt{3}\,a}{2}, \frac{a}{2}\right), \qquad a_2 = \left(\frac{\sqrt{3}\,a}{2}, \frac{a}{-2}\right) \qquad\qquad 1.1$$

With $|a_1| = |a_2| = a$. Each carbon atom is bonded to its three nearest neighbours and the vectors describing the separation between a types A atom and the nearest neighbour type B atoms as shown in Figure 1.2 are

$$R_1 = \left(\frac{a}{\sqrt{3}}, 0\right), \quad R_2 = \left(-\frac{a}{2\sqrt{3}}, -\frac{a}{2}\right), \quad R_3 = \left(-\frac{a}{2\sqrt{3}}, \frac{a}{2}\right) \qquad 1.2$$

With $|R_1| = |R_2| = |R_3| = a_{C-C}$.
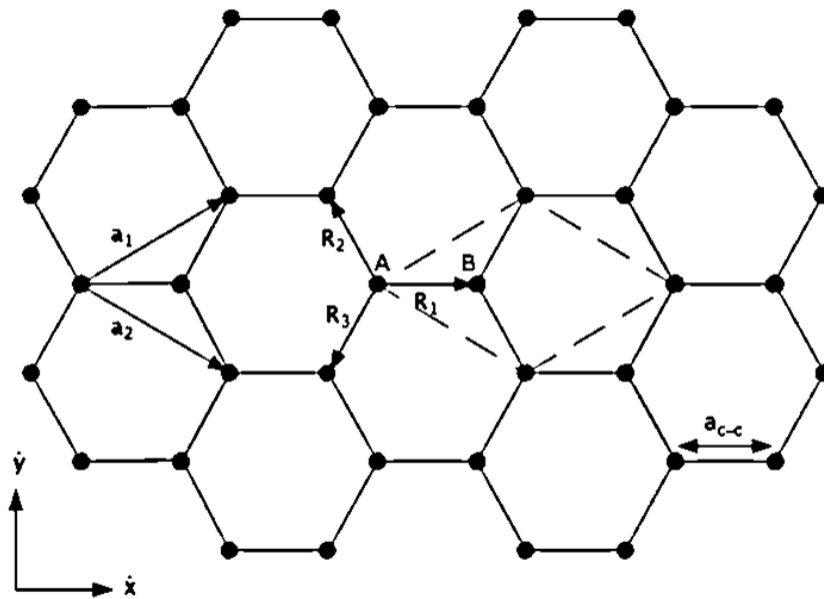
Figure. 1.2 *The honeycomb lattice of graphene. The primitive unit cell is the equilateral parallelogram (dashed lines) with a basis of two atoms denoted as A and B.*

The planar honeycomb structure of graphene has been observed experimentally and is shown in Figure 1.3. Graphene can be considered the mother of carbon the sp^2-hybridised allotropes. As illustrated in Figure 1.3, wrapping graphene into a sphere produces fullerenes, folding into a cylinder produces carbon nanotubes. As a result,

understanding the electronic properties of graphene is of central importance in

explaining, for example, the electronic properties of carbon fullerenes.
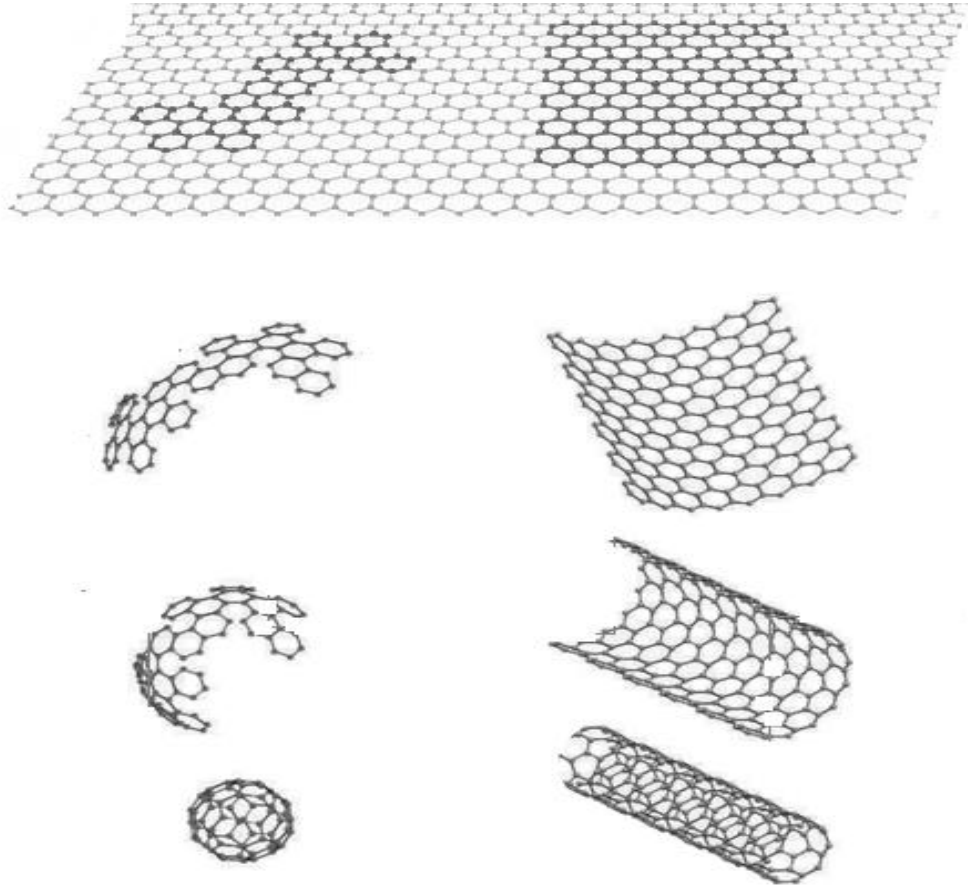
Figure 1.3 Two-dimensional graphene can be considered the building block of several carbon allotropes in all dimensions, including the zero-dimensional fullerene C60 (buckyball) and one dimensional nanotubes.

In graphene, the *2s* orbital interacts with the *2px* and *2py* orbitals to form three *sp2*

hybrid orbitals with the electron arrangement shown in Figure 1.1. The *sp2*

interactions result in three bonds called σ-bonds, which are the strongest type of

covalent bond. The σ-bonds have the electrons localized along the plane connecting

carbon atoms and are responsible for the great strength and mechanical properties of graphene and CNTs. The *2pz* electrons forms covalent bonds called π-bonds, where the electron cloud is distributed normal to the plane connecting carbon atoms. The *2pz* electrons are weakly bound to the nuclei and, hence, are relatively delocalized. These delocalized electrons are the ones responsible for the electronic properties of graphene and CNTs and as such will occupy much of our attention.

Carbon Nanotubes

The carbon nanotube (CNT) was discovered accidentally by Sumio Iijima in 1991[7,12]. There are two families of CNTs, namely single-wall CNTs and multi-wall CNTs (MWCNT). A single-wall CNT is a hollow cylindrical structure of carbon atoms with a diameter that ranges from about 0.5 to 5 nm and lengths of the order of micrometres to centimeters. A MWCNT is similar in structure to a single-wall CNT but has multiple nested or concentric cylindrical walls with the spacing between walls comparable to the interlayer spacing in graphite, approximately 0.34 nm. Carbon nanotubes are considered 1D nanomaterials as electrons move along their length confined within the 1 dimensional CNT walls[9].

Chirality in carbon nanotubes

Chirality is the key concept used to identify and describe the different configurations of CNTs and their resulting electronic band structure. Since the concept of chirality is

of fundamental importance I will introduce the concept before discussing how it is applied to describe CNT structure. The term chirality is derived from the Greek term for hand, and it is used to describe the reflection symmetry between an object and its mirror image. Formally, a chiral object is an object that is not superimposable on its mirror image; and conversely, an achiral object is an object that is superimposable on its mirror image.
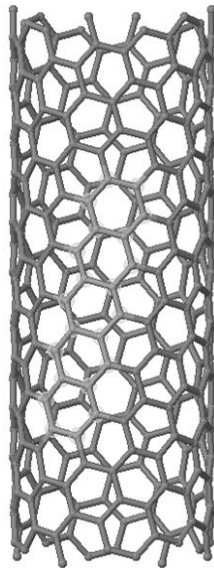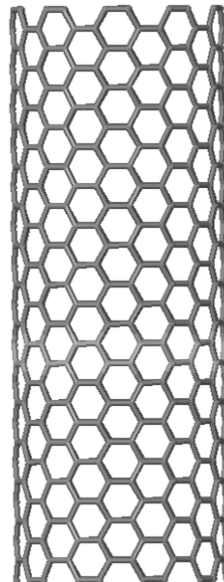
a) Chiral   b) Armchair   c) Zigzag

Figure 1.4 *The three types of single-wall CNT: (a) A chiral CNT, (b) an armchair CNT, and (c) a zigzag CNT.*

Buckyballs

The fullerenes can be used as an electric insulator because the absence of electronic coupling between the molecules. The molecules in fullerenes are held together by covalent bonds and the force existing between individual molecules is due to weak van der Waals forces which give it a soft and slippery texture. The brittleness of fullerenes is due to the weak crystalline structure resulting from covalent bonds which can form between the molecules. The smallest fullerene discovered exists as small buckyball clusters in which no two pentagons are sharing a common edge. There are many members of buckyballs clusters but the most stable is the buckyball C_{60}, which is similar to a soccer ball having twenty hexagons and twelve pentagons. C_{60} is a naturally occurring material found in soot and coal. The first fullerene C_{60} was synthesized in 1985 by R. Smalley, R. Curl, J. Heath, S. C. O'Brien, and Kroto at Rice University [13.14,15]. Figure 1.5 shows fullerene C_{60}.
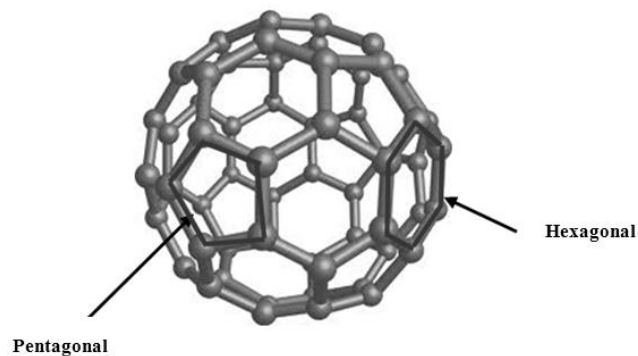
Figure 1.5 *Structure of fullerene C_{60}, which contains pentagonal and hexagonal rings. The bond lengths between a hexagon and a pentagon are 1.45 Å and between two hexagons 1.4 Å.*

C_{60} molecules represent one of the purest forms of carbon known, with no dangling bonds that would directly interact with its surroundings.

C_{60} satisfies the isolated pentagon rule IPR, fullerenes are kinetically much more stable than their pentagon counterparts, and consists of hexagons and 12 pentagons. Due to presence of adjacent pentagons C_{60} has unusual properties and high curvature. One unique property of $C_{50}Cl_{10}$ is that they are highly soluble in organic solvents and hybridized carbon atoms are have sp^3 carbon bonds with chlorine. C_{60} has additional magnetic, electronic and mechanical properties due to high curvature of molecular structure. $C_{50}Cl_{10}$ was found, isolated and identified from the soot of graphite arc-discharge in the presence of CCl_4, but the yield is very low. C_{50} includes members that belonging to fullerene family along with smaller non IPR fullerenes. CCl_4 graphite results in formation of C_{56} and C_{54} and these components can be changed under methanol and mild conditions [21].
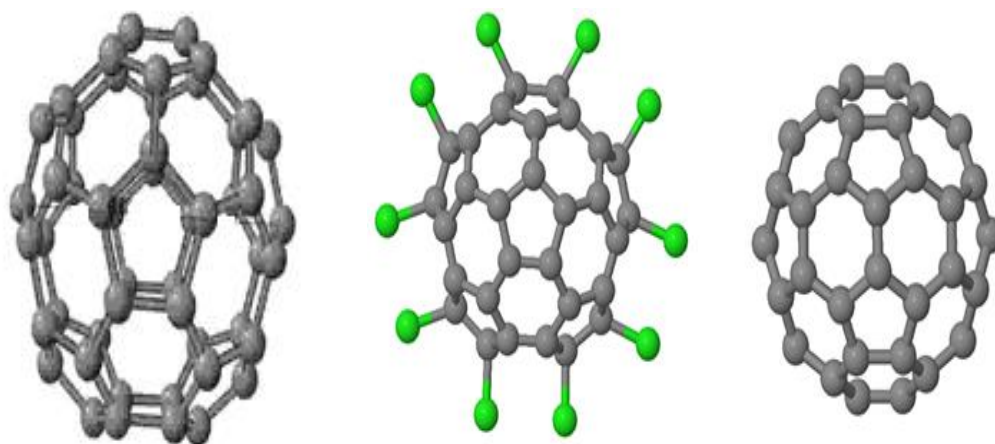
Figure 4.1 *Optimized geometries for C_{50} D_{5h} fullerene C_{50} (left), optimized geometries for exohedral-fullerene $C_{50}Cl_{10}$ (middle) and fullerene C60 (right)*

C_{50} is the isomeric structure of carbon, which about 271 classical fullerene isomers of C_{50}, that is optimized after using functional theory of first principle density. The exohedral subsidization of fullerenes is $C_{50}Cl_{10}$ and when bonds are removed chemically, they are known as open cage fullerenes. Electronic and spectroscopic properties of C_{50} reveal the derivatives that are presented as $C_{50}Cl_{10}$ (see their optimized in figure 1.7). The ground state of C_{50} has a D_3 (with six pentagon adjacencies) symmetry and a spheroid shape that is highly aromatic and the singlet nanoaromatic is presented as $D_{5h}C_{50}$ (with five pentagon adjacencies). The isomers of C_{50} are D_{5h} and D_3. Chemical properties of C50 make it susceptible to additional reactions including chlorination, dimerization and polymerization. The active sites for chemical reactions are explained as pentagon- pentagon functions D_{5h} and C_{50}. It also has high electronic affinity that makes it an electron acceptor in photovoltaic applications [20].

In this thesis I shall examine exohedral fullerenes and adding some changes in fullerenes to formed from exohedral fullerenes, namely C_{50}, C_{60} and $C_{50}Cl_{10}$. These nano-sized objects could be used as anchor groups in molecular electronic circuits and or utilised as thermoelectric materials.

Fullerenes and carbon nanotubes are fundamental building blocks for engineering exotic nanostructures such as carbon nanotube peapods (CNPs). CNPs are of interest, because nanostructures with tailored electronic properties promise to underpin a range of future low-power and high-density devices. This suggests that it may be fruitful to look beyond carbon-only CNPs for engineering transport properties of CNTs and therefore in this thesis, we explore an alternative class of CNPs formed by

encapsulating $C_{50}Cl_{10}$ as a figure 1.8. I demonstrate that of new classes of CNT peapods with switchable electronic properties.
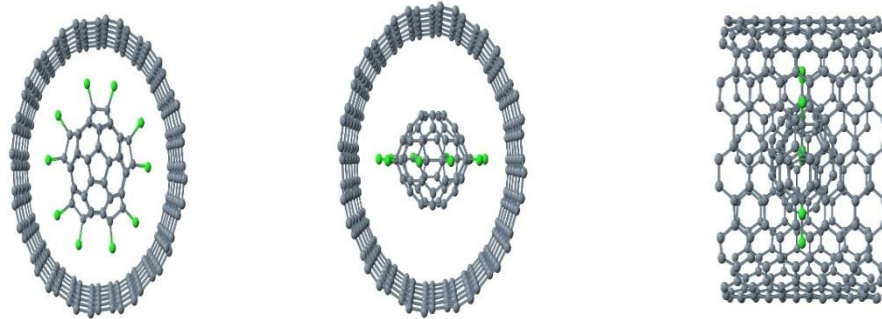
Figure 1.8 *Optimized geometries for $C_{50}Cl_{10}\perp$@CNT) left and right and $C_{50}Cl_{10}\parallel$@CNT in the middle*

1.2. Molecular Electronics

The major topic of this thesis is to investigate the electronic and thermoelectric properties of some isolated fullerenes [22] and then calculate the quantum transport properties of fullerenes and exohedral fullerenes. A huge amount of research work has already been directed in to finding a reliable technique to manipulate electronic components on a molecular scale and use molecules as an active region to design the electronics devices in 1959 when Richard Feynman presented a talk entitled "There's plenty of room at the bottom," where, he discussed the possibility of manoeuvring substances atom by atom. Based these motivational studies scientists made ways to create new structures with improved properties, dependent upon their size and miniaturization [23]. In 1965, Gordon Moore predicted in his so-called Moore's law

[24], stating that the number of transistors per chip would double every 18-24 months and furthermore he suggested that the trend could be continuing for ten years [25]. However, it lasted for nearly four decades with rapid development and it lasted for nearly four decades with rapid development. Then, the transistor becomes the essential building block of all electronic devices and becomes recognised as one of the most important inventions of the last centuries. The transistor is now a few tens of nanometers in size. This trend and this astonishing development has led to densities of more than two billion transistors per CPU in modern commercial processors, the size of each transistor is not more than few nanometres [26,27]. This gives manufactures possibilities to produce smaller and faster devices with more energy efficient but one of the biggest obstacles in molecular electronics remains to find a reliable method to contact each end of the molecule to the electrodes, presenting a good challenge to research workers. Over the past few years, many studies have been directed to investigate the electronic properties of molecules using several techniques, such as break junction, scanning probe tips, nanoprobes and nanolithography [28-31]. The molecular electronics field is used to bridge the gap between physics and chemistry and hence allows theory and experiment to work side-by-side. This led to establish collaboration between theory and experiment in two senses, firstly it is very difficult for researchers to measure the size because the molecule's size is too minute and it is even difficult to study the behaviour of molecules from the point of view of the orientation or connection to electrodes. However, this can be resolved by modelling the structure using Density Functional Theory and providing an explanation of the experimental data from theoretical calculations. Secondly theorists can predict the molecular structure before the experiment is carried out. Furthermore, the molecular electronics field might

lead to synthesis and discovery of new materials. Therefore, the most versatile and promising materials of interest recently are carbon based low dimensional materials such as graphene and its derivatives for example fullerenes and carbon nanotubes.

1.3. Outline of the thesis

This thesis strives to demonstrate predictions with a family of carbon structures and thus investigate the electronic and thermoelectric properties of some of them. Furthermore, I will examine one of these structures to design a sensing device.

One of the main result is that the direct conversion of temperature difference to electric voltage and the conversion of electric voltage into temperature difference is known as thermoelectric effect. A thermoelectric device is used for this purpose which creates voltage when there is temperature difference on each side. Similarly, the temperature difference is created when electric voltage is applied to it. The temperature difference causes the charge carriers to move and diffuse from the hot side to the colder side. Generally, this effect is used to measure temperature difference, generate electricity or to change the temperature of an object.

The thermoelectric effect is associated with three separate effects namely the Seebeck effect, Peltier effect and Thomson effect and sometimes it is generally known as Peltier-Seebeck effect. Joule heating, on the other hand describes the heat which is generated because of passing current. However, the Joule heating is not thermodynamically reversible contrary to Peltier-Seebeck and Thomson effects.

As a build up of this thesis the first step is the introduction of fullerenes and their electronic and thermoelectric properties. In Chapter 2 and 3, I will introduce the theory starting discussion on Density Functional Theory and SIESTA DFT package. After, Green's Function, methods used for quantum transport calculations are introduced. Next, overview on scattering theory, in Chapter 4, I will use these two methods to study and compare between C_{50}, C_{60} and $C_{50}Cl_{10}$ molecules and their electronic properties. Then, in chapter 5, I will describe my research work on C_{60} and $C_{50}Cl_{10}$ which will present some of the results on the conductance of C_{60} and $C_{50}Cl_{10}$ molecule against the changes in the system geometry and how they are employed in electronic devices. Afterwards the thermoelectric properties of single, double C_{60}-s and $C_{50}Cl_{10}$-s have been described where we observed an increase or decrease of thermopower when going from one to two fullerenes and towards the end I will provide a thermoelectric material with a positive Seebeck coefficient of opposite sign to that of C_{60}. Finally, in Chapter 6, I will summarize findings and conclusions then give recommendations for future research work in this topic. One interesting study would be using buckyballs and exohedral buckyballs in peapods systems, as in the appendix, which should increase their electronic communication.

Chapter 2

Density Functional Theory

2.1. Introduction

Density Functional Theory (DFT) is widely used by physicists and chemists to investigate the ground-state properties of interacting many-particle systems such as atoms, molecules and crystals. It is actually a computational quantum mechanical modelling method and it is used to transform the many-body system into one of non-interacting fermions in an effective field. Typically the many-body system is used for those physical problems pertaining to microscopic level systems and these systems are generally made of numerous interacting particles. In other words, the electrical properties of many interacting particle systems can be described as a function of the ground-state density of the system [32,33]. DFT is a reliable methodology which has been applied to a large variety of molecular systems with a huge number of books and articles in the literature giving detailed descriptions of the principles of DFT and its application [32-37]. The importance of DFT can also be recognised by the fact that the 1998 Nobel Prize in Chemistry was awarded to Walter Kohn for his development of density functional theory. The beginnings of DFT were founded upon the Thomas-Fermi model back in the 1920s which provided the basic steps to obtain the density functional for the total energy based on wavefunctions [32,37-39]. Further improvement was made by Hartree, Dirac, Fock and Slater and nearly four decades after the Thomas-Fermi work. The Hohenberg-Kohn theorems and Kohn-Sham method further paved the foundations [32,34,35,38-42].

In this chapter a brief introduction to DFT is given outlining the main formalism as a method of finding the solution of the non-relativistic many-particle time independent Schrödinger equation (TISE), since the properties of a many-electron system can be determined by using functionals of the electron density. A brief summary of the DFT code 'SIESTA' has also been discussed which have been used extensively throughout this research work as a theoretical tool to optimise the structures.

2.2. The Schrödinger Equation and Variational Principle

If the analytic solution of Schrodinger equation cannot be found then a mathematical trick known as the variational principle is used that allows estimating the energy of the ground state of a system. Any given non-relativistic many particles system can be described by the time independent, non-relativistic Schrödinger equation:

$$\text{H}\Psi_i(\vec{r}_1, \vec{r}_2, \ldots, \vec{r}_N, \vec{R}_1, \vec{R}_2, \ldots, \vec{R}_M) = E_i \Psi_i(\vec{r}_1, \vec{r}_2, \ldots, \vec{r}_N, \vec{R}_1, \vec{R}_2, \ldots, \vec{R}_M) \qquad (2.1)$$

here H represents time-independent Hamiltonian operator of a system consisting of *N*-electrons and *M*-nuclei which describes the interaction of particles with each other, where Ψ_i is the wavefunction of the ith state of the system and E_i is the numerical value of the energy of the ith state described by Ψ_i. The Hamiltonian operator of such a system can be written as a sum of five terms given by [33,34,43]:

$$H = -\overbrace{\frac{\hbar^2}{2m_e}\sum_{i=1}^{N}\nabla_i^2}^{T_e} - \overbrace{\frac{\hbar^2}{2m_n}\sum_{n=1}^{M}\nabla_n^2}^{T_n} - \overbrace{\frac{1}{4\pi\varepsilon_o}\sum_{i=1}^{N}\sum_{n=1}^{M}\frac{1}{\left|\vec{r}_i - \vec{R}_n\right|}Z_n e^2}^{U_{en}}$$

$$+\overbrace{\frac{1}{4\pi\varepsilon_o}\frac{1}{2}\sum_{i=1}^{N}\sum_{i\neq j}^{N}\frac{e^2}{\left|\vec{r}_i - \vec{r}_j\right|}}^{U_{ee}} + \overbrace{\frac{1}{4\pi\varepsilon_o}\frac{1}{2}\sum_{n=1}^{M}\sum_{n\neq n'}^{M}\frac{1}{\left|\vec{R}_n - \vec{R}_{n'}\right|}Z_n Z_{n'} e^2}^{U_{nn}}$$

(2.2)

here i and j denote the N-electrons while n and n' run over the M-nuclei in the system

m_e and m_n are the mass of electron and nucleus respectively

e and Z_n are the electron and nuclear charge respectively

$\vec{r}_i$ and $\vec{R}_n$ represent the position of the electrons and nuclei respectively, and ∇_i^2 is the Laplacian operator which is defined in Cartesian coordinates as:

$$\nabla_i^2 = \frac{\partial^2}{\partial x_i^2} + \frac{\partial^2}{\partial y_i^2} + \frac{\partial^2}{\partial z_i^2}$$

In (2.2), the first two terms, namely T_e and T_n represent the kinetic energy of electrons and nuclei respectively while the last three terms represent the potential part of the Hamiltonian. The U_{en} term defines the attractive electrostatic interaction between electrons and nuclei. The electron-electron, U_{ee} and nuclear-nuclear, U_{nn} describe the repulsive part of the potential respectively [32,34,37,40,44].

The Born-Oppenheimer approximation known as the clamped nuclei approximation can be applied due to the fact that about 99.9% of atom's mass is concentrated in the nucleus (for example, the hydrogen nucleus weighs approximately 1800 times more than an electron) and the nuclei can be considered as a fixed point relative to the electrons

hovering around the nucleus. In this case, if the nuclei of the treated atoms are fixed, their kinetic energy is zero and they do not contribute to the full wavefunction anymore. The outcome of this assumption is that the Hamiltonian of the electron system reduces the Hamiltonian to the electronic Hamiltonian H_{ele} which in the fixed nuclear picture can be rewritten as [32,34,37,44-46]:

$$
H_{ele} = \overbrace{-\frac{\hbar^2}{2m_e}\sum_{i=1}^{N}\nabla_i^2}^{T_e} - \overbrace{\frac{1}{4\pi\varepsilon_o}\sum_{i=1}^{N}\sum_{n=1}^{M}\frac{1}{|\vec{r}_i - \vec{R}_n|}Z_n e^2}^{U_{en}} + \overbrace{\frac{1}{4\pi\varepsilon_o}\frac{1}{2}\sum_{i=1}^{N}\sum_{i\neq j}^{N}\frac{e^2}{|\vec{r}_i - \vec{r}_j|}}^{U_{ee}}
$$

(2.3)

For such a system, the Schrödinger equation for 'clamped-nuclei' is given as

$$
H_{ele}\Psi_{ele} = E_{ele}\Psi_{ele}
$$

(2.4)

Ψ_{ele} depends on the electron coordinates, while the nuclear part enters only parametrically and does not explicitly appear in Ψ_{ele}.

The wavefunction itself is not an observable quantity while its modulus squared can be written as:

$$
n(\vec{r}) = |\Psi(\vec{r}_1, \vec{r}_2, \ldots, \vec{r}_N)|^2 \int d\vec{r}_1 \, d\vec{r}_2 \ldots d\vec{r}_N
$$

(2.5)

The virtue of density functional theory is that it expresses the physical quantities in terms of the ground-state density. The electronic density of a general many body state, characterized by a wave function $\Psi(r_1, r_2, \ldots r_i \ldots)$, is defined as

24

$$\rho(r) = \int dr_2 dr_3 \ldots dr_i \ldots \left| \Psi(r_1, r_2, \ldots r_i \ldots) \right|^2 \tag{2.6}$$

This represents the probability that electrons 1, 2,....., N are found in the volume elements $d\vec{r}_1, d\vec{r}_2 \ldots d\vec{r}_N$. Since by their nature electrons are indistinguishable, this probability is unchangeable if the coordinates of any two electrons (here i and j) are swapped [43]:

$$\left| \Psi(\vec{r}_1, \vec{r}_2, \ldots \vec{r}_i, \vec{r}_j, \ldots, \vec{r}_N) \right|^2 = \left| \Psi(\vec{r}_1, \vec{r}_2, \ldots \vec{r}_j, \vec{r}_i, \ldots, \vec{r}_N) \right|^2 \tag{2.7}$$

Since electrons are fermions with spin of a half then Ψ must be antisymmetric with respect to the interchange of the spatial and the spin coordinates of any two electrons:

$$\Psi(\vec{r}_1, \vec{r}_2, \ldots \vec{r}_i, \vec{r}_j, \ldots, \vec{r}_N) = -\Psi(\vec{r}_1, \vec{r}_2, \ldots \vec{r}_i, \vec{r}_j, \ldots, \vec{r}_N) \tag{2.8}$$

A logical consequence of the probability interpretation of the wavefunction is that the integral of equation (2.6) over the full range of all variables equals one. Therefore the probability of finding the N-electron anywhere in space must be unity,

$$\int \ldots \int \left| \Psi(\vec{r}_1, \vec{r}_2, \ldots, \vec{r}_N) \right|^2 d\vec{r}_1 \, d\vec{r}_2 \ldots d\vec{r}_N = 1 \tag{2.9}$$

A wavefunction which satisfies equation (2.9) is a normalized wavefunction.

Hartree and Hartree-Fock etc. are the theories which have been developed to solve the Schrödinger equation since it has no exact solution. These theories were based on an important theoretical principle called the variational principle of the wavefunction where a suitable trial wave-functions Ψ_{Tri} is used. This principle is useful to study the ground state, but is not very useful for the study of excited states. When a system is in the state Ψ_{Tri}, the expectation value of the energy is given by [32-37,40,43]:

$$\langle E_{Tri}\rangle = \frac{\int \Psi_{Tri}\, \text{H}\, \Psi_{Tri}^*\, d\vec{r}}{\int \Psi_{Tri}\, \Psi_{Tri}^*\, d\vec{r}} \qquad (2.10)$$

This means the energy is obtained from the expectation value of the Hamiltonian operator from any Ψ_{Tri} (presumed wave-function) which is an upper bound to the true ground-state energy Ψ_{GS}. If Ψ_{Tri} is normalized according to equation (2.9), and Ψ_{Tri} equals to the ground state ($\Psi_{Tri} = \Psi_{GS}$). This means E_{Tri} equals to the exact ground state energy E_{GS}, now we can rewrite equation (2.10) for the ground state as:

$$\langle E_{GS}\rangle = \int \Psi_{GS}\, \text{H}\, \Psi_{GS}^*\, d\vec{r} \qquad (2.11)$$

The normalized Ψ_{Tri} can show that $E_{Tri} > E_{GS}$ or $E_{Tri} = E_{GS}$. Therefore the best choice of E_{Tri} is the one in which E_{Tri} is minimized [34,35,37].

2.3. The Thomas-Fermi (T-F) Model

For obtaining information about the electronic structure the earliest attempts to use the electron density rather than the wavefunction were made when quantum mechanics was emerging itself. The work of Llewellyn Thomas in 1926 and Enrico Fermi in 1928 was the earliest attempts who created independently the same idea of trying to construct a model to approximate the kinetic and potential energy as a function of the electron density. The T-F model is a quantum mechanical model defined by the energy function for the ground state level of the system with a specific number of orbitals in the atom and particular charge. Therefore, it is the first attempt to use the electron density instead of the wavefunction to solve the ground state Schrödinger equation for many body systems [38,39,43,47,48]. Despite the fact that electrons are distributed non-uniformly in an atom, it is assumed that they are distributed uniformly (based on the uniform electron gas) in each small element of volume ΔV locally, while the electron density $n(\vec{r})$ could be varied from ΔV to the next. By using this approximation for the kinetic energy which is given by:

$$T_{T-F}[n(\vec{r})] = C_F \int [n(\vec{r})]^{5/3} \ d\vec{r} \tag{2.12}$$

Here C_F is constant and is given by

$C_F = \frac{3}{10} (3\pi^2)^{2/3} = 2.8712$

$n(\vec{r})$ represents the electron density

An approximation can also be proposed to determine the internal potential energy U_{en}

due to the attractive interaction of N-electrons with M-nuclei:

$$U_{en} = \int n(\vec{r}) \, V_n(\vec{r}) \, d\vec{r} \tag{2.13}$$

where $V_n(\vec{r})$ is the potential energy of an electron due to the nucleus electric field (external potential) and is given by:

$$V_n(\vec{r}) = -\frac{1}{4\pi\varepsilon_o} \sum_{i=1}^{N} \sum_{n=1}^{M} \frac{1}{|\vec{r}_i - \vec{R}_n|} Z_n e^2 \tag{2.14}$$

here Z and e are electron number and the electron charge approximately. The approximate electron-electron repulsive energy is given by:

$$U_{ee} = \frac{1}{4\pi\varepsilon_o} \frac{1}{2} e^2 \int \frac{n(\vec{r})n(\vec{r'})}{|\vec{r} - \vec{r'}|} \, d\vec{r} \, d\vec{r'} \tag{2.15}$$

The equations (2.12), (2.13) and (2.15) with U_{nn} term give the T-F model:

$$F_{T-F}[n(\vec{r})] = T_{T-F} + U_{en} + U_{ee} + U_{nn} \tag{2.16}$$

The fourth term U_{nn} in equation (2.16) is the nuclear-nuclear repulsion and it is an important determined constant in both cases either the nuclei are binding or not, for M-nuclei in the system, it is given by [32,34,38,39,43]:

$$U_{nn} = \frac{1}{4\pi\varepsilon_o} \frac{1}{2} \sum_{n=1}^{M} \sum_{n \neq n'}^{M} \frac{1}{|\vec{R}_n - \vec{R}_{n'}|} Z_n Z_{n'} \, e^2 \tag{2.17}$$

2.4. The Hohenberg-Kohn Theorems

DFT is based on Hohenberg-Kohn theorems proposed by Hohenberg and Kohn in 1964 where the electron density $n(\vec{r})$ is used to calculate the ground state energy [37,48,49]. Theorem (1) states that for any interacting many particle system with an applied external potential $V_{ext}(\vec{r})$, the density is uniquely determined. In other words, it demonstrates that the density $n(\vec{r})$ may be used instead of the potential as a basic function uniquely characterising the system, and be stated as the ground state density $n_{GS}(\vec{r})$ which uniquely determines the potential up to an arbitrary constant [37,41,48,50]. This theorem is proven for densities with non-degenerate ground states and the proof is elementary and by contradiction. Let us consider two different external potentials $V_{ext}(\vec{r})_{(1)}$ and $V_{ext}(\vec{r})_{(2)}$ which differ by more than a constant and yield the same ground state density $n_{GS}(\vec{r})$. Clearly the above two potentials correspond to distinct Hamiltonians which are $H_{ext}[(\vec{r})]_{(1)}$ and $H_{ext}[(\vec{r})]_{(2)}$, these Hamiltonians give rise to distinct wavefunctions which are $\Psi_{ext}[(\vec{r})]_{(1)}$ and $\Psi_{ext}[(\vec{r})]_{(2)}$.

Since the ground state is same and according to the variational principle there is no wavefunction that gives energy less than that of $\Psi_{ext}[(\vec{r})]_{(1)}$ for $H_{ext}[(\vec{r})]_{(1)}$, that is:

$$\langle E_{(1)} \rangle = \int \Psi_{(1)} H_{(1)} \Psi_{(1)}^* \, d\vec{r} < \int \Psi_{(2)} H_{(2)} \Psi_{(2)}^* \, d\vec{r} \qquad (2.18)$$

For non-degenerate ground state and because of the identical ground state densities for two Hamiltonians, the equation (2.18) becomes:

$$\int \Psi_{(2)} H_{(1)} \Psi_{(2)}^* \, d\vec{r} = \overbrace{\int \Psi_{(2)} H_{(2)} \Psi_{(2)}^* \, d\vec{r}}^{\langle E_{(2)} \rangle} + \int \{ [V_{ext}(\vec{r})]_{(1)} - \tag{2.19}$$

$$[V_{ext}(\vec{r})]_{(2)} \} n_{GS}(\vec{r}) \, d\vec{r}$$

By exchanging the labels in equation (2.19), we have:

$$\int \Psi_{(1)} H_{(2)} \Psi_{(1)}^* \, d\vec{r} = \overbrace{\int \Psi_{(1)} H_{(1)} \Psi_{(1)}^* \, d\vec{r}}^{\langle E_{(1)} \rangle} + \int \{ [V_{ext}(\vec{r})]_{(2)} - \tag{2.20}$$

$$[V_{ext}(\vec{r})]_{(1)} \} n_{GS}(\vec{r}) \, d\vec{r}$$

Adding (2.19) and (2.20) gives:

$$\langle E_{(1)} \rangle + \langle E_{(2)} \rangle < \langle E_{(2)} \rangle + \langle E_{(1)} \rangle \tag{2.21}$$

This clearly shows a contradiction and therefore the theorem has been proven by reductio ad absurdum.

Theorem (2) provides a variational ansatz for obtaining $n(\vec{r})$, i.e. searching for $n(\vec{r})$ so as to minimise the energy. It states that, in terms of the density $n(\vec{r})$, a universal functional for the energy $E[n(\vec{r})]$ can be defined. The exact ground state energy of the system in particular $(V_{ext}(\vec{r}))$ is the global minimum value of this functional and the density $n(\vec{r})$ which minimizes the functional and represents the exact ground state density $n_{GS}(\vec{r})$ [32]. Proof (2), the first theorem states that the total energy of system is a functional of the density $n(\vec{r})$ and is given by [32,37,41,48,50]:

30

$$E_{total}[n(\vec{r})]$$

$$= \overbrace{T_{int}[n(\vec{r})] + \underbrace{U_{ee}[n(\vec{r})]}_{\substack{=zero, \ for \\ non-interacting \\ system}}}^{F_{H-K}[n(\vec{r})]} + \int V_{ext}(\vec{r}) \, n(\vec{r}) \, d\vec{r} \qquad (2.22)$$

In this equation the kinetic energy is given by the first two terms ($F_{H-K}[n(\vec{r})]$) as (T_{int}) and the electron-electron interaction energy (U_{ee}) is the same for the whole system. Thus $F_{H-K}[n(\vec{r})]$ is a universal functional, described as the Holy Grail of density functional theory. Assuming that the system is in the ground state, the energy can be uniquely defined by the ground state density $n_{GS}(\vec{r})$ such as:

$$\langle E_{GS} \rangle = \langle E[n_{GS}(\vec{r})] \rangle = \int \Psi_{GS} \, H_{GS} \, \Psi_{GS}^{*} \, d\vec{r} \qquad (2.23)$$

According to the variational principle any different density will correspond to a higher energy because the ground state energy corresponding to the ground state density is the minimum energy:

$$\langle E_{GS} \rangle = \langle E[n_{GS}(\vec{r})] \rangle = \int \Psi_{GS} \, H_{GS} \, \Psi_{GS}^{*} \, d\vec{r} < \int \Psi \, H \, \Psi^{*} \, d\vec{r}$$
$$= \langle E[n(\vec{r})] \rangle = \langle E \rangle \qquad (2.24)$$

In (2.22) the total energy can be minimized with respect to variations in the density function when the functional $F_{H-K}[n(\vec{r})]$ is known. This leads to finding the exact ground state properties of the system since for most practical calculations, the direct

minimization will not provide the ground state energy, but by the simpler procedure due to Kohn-Sham.

2.5. Kohn-Sham Method and Self-Consistent Field SFC

This is well known that DFT avoids the interacting many particle problem. However over the interacting system the non-interacting system has one great advantage since finding the ground-state energy for such system is relatively easier. In 1965, Kohn and Sham discovered the possibility to replace the original Hamiltonian of the system by an effective Hamiltonian (H_{eff}) of the non-interacting system in an effective external potential $V_{eff}(\vec{r})$. This gives rise to the same ground state density as the original system. The Kohn-Sham method is considered as an ansatz because there is no clear recipe for calculating this. However it is a lot easier to solve than the non-interacting problem. Hohenberg-Kohn theory is applicable to both interacting and non-interacting systems. The Kohn-Sham method is based on the Hohenberg-Kohn universal density [37,40,41,51]:

$$F_{H-K}[n(\vec{r})] = T_{int}[n(\vec{r})] + U_{ee}[n(\vec{r})] \tag{2.25}$$

For non-interacting electrons the Hohenberg-Kohn functional is reduced to only the kinetic energy. The energy functional of the Kohn-Sham ansatz $F_{K-S}[n(\vec{r})]$, in contrast to (2.22), is given by:

$$F_{K-S}[n(\vec{r})] = T_{non}[n(\vec{r})] + E_{Hart}[n(\vec{r})] + \int V_{ext}(\vec{r}) \, n(\vec{r}) \, d\vec{r}$$

$$+E_{xc}[n(\vec{r})] \tag{2.26}$$

T_{non} is the kinetic energy of the non-interacting system and is different from T_{int} (for interaction system) in equation (2.22), while E_{Hart} is the classical electrostatic energy or classical self-interaction energy of the electron gas associated with density $n(\vec{r})$. The fourth term E_{xc} is the exchange-correlation energy functional and given by:

$$E_{xc}[n(\vec{r})] = F_{H-K}[n(\vec{r}) - \overbrace{\frac{1}{2}\int \frac{n(\vec{r}_1)n(\vec{r}_2)}{|\vec{r}_1 - \vec{r}_2|}d\vec{r}_1 d\vec{r}_2}^{E_{Hart}[n(\vec{r})]} - \; T_{non}[n(\vec{r})] \tag{2.27}$$

In equation (2.26) the first three terms can be cast into functional form. In contrast, however there is no exact functional form for E_{xc}. Recently much research work has been directed into finding a better approximation to E_{xc}. Currently, the functionals can investigate and predict the physical properties of a wide range of solid state systems and molecules. For the last three terms in equation (2.26), we take the functional derivatives to construct the effective single particle potential $V_{eff}(\vec{r})$:

$$V_{eff}(\vec{r}) = V_{ext}(\vec{r}) + \frac{\partial E_{Hart}[n(\vec{r})]}{\partial n(\vec{r})} + \frac{\partial E_{xc}[n(\vec{r})]}{\partial n(\vec{r})} \tag{2.28}$$

Now, this potential can be used to give the Hamiltonian of the single particle:

$$H_{K-S} = T_{non} + V_{eff} \qquad (2.29)$$

The Schrödinger equation becomes pretty simple when this Hamiltonian is used:

$$[T_{non} + V_{eff}]\Psi_{K-S} = E\Psi_{K-S} \qquad (2.30)$$

Equation (2.30) is known as Kohn-Sham equation. The ground state density $n_{GS}^{K-S}(\vec{r})$ corresponds to the ground state wavefunction Ψ_{GS}^{K-S} which minimizes the Kohn-Sham functional subject to the orthonormalization constraints $\langle \Psi_i | \Psi_j \rangle = \delta_{ij}$; it is found by a self-consistent calculation [32,35,45,52].

E_{Hart} and E_{xc} can be accurately determined in DFT where a self-consistent field procedure is used. However V_{eff} cannot be calculated until the correct ground state density is known. In addition to that the correct density cannot be obtained from the Kohn-Sham wavefunctions until equation (2.30) is solved with the correct V_{eff}. Therefore the circular problem can be solved by carrying out a self-consistent cycle as shown in figure 2.1 [34,43,53].
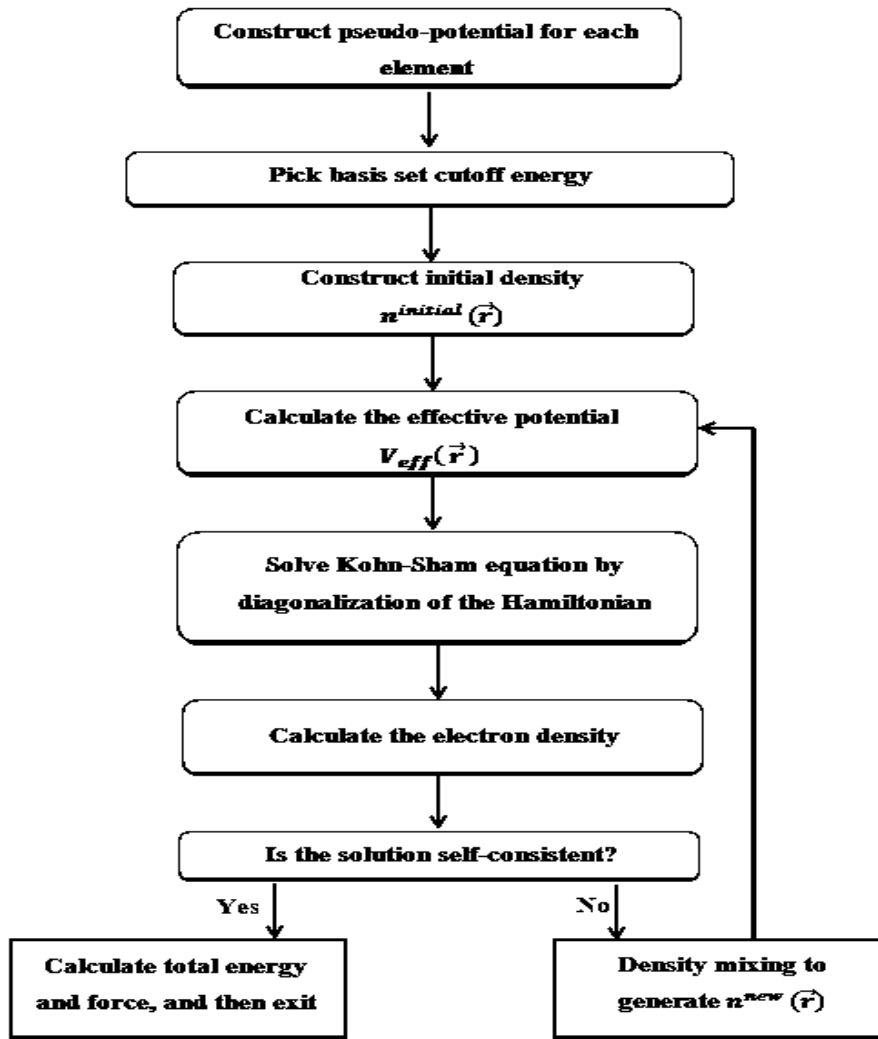
Figure 2.1 A Schematic illustration of the self-consistent DFT cycle.

The procedure is shown in figure 2.1, where the first step is to generate the pseudo-potential. The pseudo-potential represents the electrostatic interaction between the valence electrons and the nuclei and core electrons. The basis set with a selected kinetic energy cutoff to be inserted in the basis set is built up in the next step. This is needed to expand the density functional quantities.

The energy functional is fully determined if the density is known. A trial electronic density $n^{initial}(\vec{r})$ is made as an initial guess to calculate the following quantity:

$$G = E_{Hart}[n^{initial}(\vec{r})] + E_{xc}[n^{initial}(\vec{r})] \qquad (2.31)$$

$\frac{\partial G}{\partial n^{initial}(\vec{r})}$ and the effective potential V_{eff} are then calculated and the later is used to solve the Kohn-Sham equation (2.30). This leads to find the electron Hamiltonian and after that it is diagonalised in order to find the eigenfunctions and the new electron density $n^{new}(\vec{r})$. Hopefully, this $n^{new}(\vec{r})$ will be closer to true ground state and is checked.

The end of the loop is, for self-consistency, if this new updated electron density $n^{new}(\vec{r})$ agrees numerically with the density $n^{initial}(\vec{r})$ used to build the Hamiltonian at the beginning of the SCF cycle. After exit, all the desired converged quantities, such as the total energy, the electronic band structure, density of states *etc.* are calculated. Otherwise, the new density $n^{new}(\vec{r})$ does not agree with the starting density $n^{initial}(\vec{r})$, one generates a new input density and starts another SCF cycle: build the new density-dependent Hamiltonian, solve and compute the density, and check for self-consistency [34,48,54].

A complicated many-body system can be mapped onto a set of simple non-interacting equations exactly if the exchange correlation functional is known according to Kohn-Sham approach. However, the exchange-correlation functional is not known exactly so approximations need to be made.

2.6. The Exchange-Correlation Potential

Although DFT is very reliable and proven method, but for kinetic energy functional and the exchange-correlation functional in terms of the density it still uses an approximation. Much research work has been directed to find reliable expressions for those functionals. The Local Density Approximation (LDA) are the most commonly exchange-correlation functional approximations, which depends only on the density. The more complicated, however are Generalised Gradient Approximation (GGA), which includes the derivative of the density and also contains information about the environment and hence it is semi-local.

Local Density Approximation (LDA)

It is possible to calculate the functional E_{xc} functional in a homogenous electron gas to approximate the many body particle problem as a simpler system based on Kohn-Sham method [42]. By slowly varying the density of a system, the E_{xc} functional at point $\vec{r}$ can be considered as acting in a uniform density. E_{xc} can be represented by a uniform electron gas $E_{xc}^{homo}[n(\vec{r})]$ with a density $n(\vec{r})$.

LDA typically will not work for those systems which are dominated by electron-electron interactions. An assumption, however is made that the density is considered a constant in the local region around any considered position and it is given by [37,43]:

$$E_{xc}^{LDA}[n(\vec{r})] = \int E_{xc}^{homo}[n(\vec{r})]n(\vec{r})d\vec{r} \tag{2.32}$$

It is possible to split the exchange-correlation energy $E_{xc}^{homo}[n(\vec{r})]$ into two terms such as the sum of the exchange $E_x^{homo}[n(\vec{r})]$ and the correlation energies $E_c^{homo}[n(\vec{r})]$ which can be found separately as:

$$E_{xc}^{homo}[n(\vec{r})] = E_x^{homo}[n(\vec{r})] + E_c^{homo}[n(\vec{r})] \qquad (2.33)$$

The first term can be found analytically. It is well known (see [37,43]) and is given by:

$$E_x^{homo}[n(\vec{r})] = -\frac{3}{4}\left(\frac{3n(\vec{r})}{\pi}\right)^{1/3} \qquad (2.34)$$

However, $(E_c^{homo}[n(\vec{r})])$ cannot be obtained analytically, but numerical methods can be used to calculate it accurately. The most common and accurate method was proposed by **C**eperly and **A**lder **(CA)** [55] using quantum Monte-Carlo simulations. There are several different interpretations of the Monte Carlo data, for example, the most used was calculated by **P**erdew and **Z**unger (PZ), who fitted this numerical data to an analytical expression and obtained [56,57]:

$$E_c^{homo}[n(\vec{r})] = \begin{cases} -0.048 + 0.031\,ln(r_o) - 0.0116\,r_o + 0.002\,ln(r_o) & if\ r_o < 1 \\ -\dfrac{0.1423}{(1 + 1.9529\sqrt{r_o} + 0.3334\,r_o} & if\ r_o > 1 \end{cases} \qquad (2.35)$$

here r_o is the average distance between the electrons in the homogenous electron gas and defined as $\left(\frac{3}{4\pi n}\right)^{1/3}$.

It can be seen that the LDA is a simple and well known powerful functional and is considered to be accurate for graphene and carbon nanotubes or where the electron density is not rapidly changing. In case of atoms with *d* and *f* orbitals, a larger error is expected. This functional to some extent has many pitfalls, for example the band gap in semiconductors and insulators is usually not accurate with a large error (typically in the range of 0.5 to 2eV or 10-30%). Therefore, it is highly advisable to seek better functionals [56,58,59].

Generalized Gradient Approximation (GGA)

All systems are considered as the homogenous systems in LDA, but the real systems are inhomogeneous. A step may be taken beyond the LDA and extend it by including the derivative information of the density into the exchange-correlation functional in order to take this into account. This is done by including the gradient and the higher spatial derivatives of the total charge density ($|\nabla n(\vec{r})|, |\nabla^2 n(\vec{r})|, ...$) into the approximation. Such a functional is called the generalized gradient approximation (GGA). It has to be calculated along with the correlation contributions using numerical methods because there is no closed expression for the exchange part of the functional. Exactly as in the case of the LDA many parameterizations exist for the exchange-correlation energies in the GGA [60-63].

The proposed functional form which is presented by **P**erdew, **B**urke and **E**rnzerhof (PBE) [60] is discussed in this section. There are two separate expressions in this parameterization, the first expression is the exchange $E_x^{GGA}[n(\vec{r})]$ and is given by:

$$E_x^{GGA}[n(\vec{r})] = \int n(\vec{r}) \, E_x^{homo}[n(\vec{r})] \, F_x(s) d\vec{r}, \qquad (2.36)$$

$$F_x(s) = 1 + \kappa - \frac{\kappa}{(1+\mu s^2)/\kappa}$$

$F_x(s)$ is called the enhancement factor,

$\kappa = 0.804, \ \mu = 0.21951$

$s = |\nabla n(\vec{r})/2k_s n(\vec{r})|$ is the dimensionless density gradient, where $k_s = \sqrt{\frac{4 \, k_{T-F}}{\pi a_o}}$ and

$k_{T-F} = \frac{(12/\pi)^{1/3}}{\sqrt{r_s}}$ is the Thomas-Fermi screening wavenumber whereas r_s is the local

Seitz radius.

The second expression is the correlation energy $E_x^{GGA}[n(\vec{r})]$ and given by:

$$E_c^{GGA}[n(\vec{r})] = \int (E_c^{homo}[n(\vec{r})] + \chi[n(\vec{r})]) d\vec{r}, \qquad (2.37)$$

$$\chi[n(\vec{r})] = \frac{e^2}{a_o} \gamma \, ln \left(1 + \frac{\beta}{\gamma} \, t^2 \, \frac{1+At^2}{1+At^2+A^2t^4}\right),$$

$$A = \frac{\beta}{\gamma} \left[e^{\left(\frac{E_c^{homo}[n(\vec{r})]}{\gamma}\right)-1} \right]^{-1}$$

where $\gamma = (1 - ln(2)/\pi^2, \ t = |\nabla n(\vec{r})/2k_{T-F}n(\vec{r})|$ is another dimensionless

density gradient, $\beta = 0.066725$, and $a_0 = \frac{\hbar}{me^2}$.

The two most commonly used approximations for the approximation of exchange-correlation energies in the DFT are LDA and GGA as discussed above. There are several other functionals, which go beyond LDA and GGA. However, there is not a single robust theory of the validity of these functionals. It is determined via testing the functional for various materials over a wide range of systems and comparing results with reliable experimental data.

2.7. SIESTA

In this research work all calculations were carried out by the implementation of DFT in the SIESTA code. SIESTA is an acronym derived from the **S**panish **I**nitiative for **E**lectronic **S**imulations with **T**housands of **A**toms. It is used to obtain the relaxed geometry of the structures discussed here and also to carry out the calculations to investigate their electronic properties. It is a self-consistent density functional theory technique and to perform efficient calculations it uses norm-conserving pseudo-potentials and a **L**inear **C**ombination of **A**tomic **O**rbital **B**asis **s**et (LCAOB). For more theoretical details, the reader is referred to [64]. There are two different modes to perform DFT simulations using SIESTA [65,66]. One mode is a conventional self-consistent field diagonalisation method to solve the Kohn-Sham equations and the second is by direct minimization of a modified energy functional [67]. This section will describe some of SIESTA's components and how they are implemented within the code.

The pseudo-potential approximation

The distribution of the valence electrons in any system is a very good description of physical properties of that system. The spread of electrons around the nucleus are generally categorized as core and valence electrons. Investigating the electronic properties is typically expensive in terms of time and computer memory for a system containing a large number of atoms containing complex potentials. It is possible to reduce the number of electrons involved in the simulation by introducing an approximation known as a pseudo-potential or effective potential. This way an effort is made to replace the complicated effects of the motion of the non-valence electrons (core electrons) of an atom and the nucleus by pseudo-potential. Actually the core electrons do not participate in chemical bonding since they are spatially localised about the nucleus, and there is a weak overlap of their wavefunctions with the core electron wavefunctions from neighbouring atoms. Only the valence electrons contribute to the formation of the molecular orbital because only these electron states overlap in most systems. It is therefore understandable to assume that the core electrons can be removed and replaced by pseudo-potential. The coulombic potential term for the core electrons in Schrodinger equation is replaced by a modified effective potential term. Fermi in 1934 and Hellmann in 1935 introduced the first pseudo-potential approximation [66-69]. Some advantages of using pseudo-potentials in the computational calculations are discussed here. It can be used:

- To reduce the number of the electrons which are participating in the calculations by not considering the core electrons for calculations and this significantly reduces both time and memory required to run the ab-initio simulation.

- To reduce the total energy scale by not considering the core electrons from calculation making the numerical calculation of energy differences between atomic configurations much more stable.

- To exactly match the true valence wave-functions outside of the core or cut-off radius r_c, but are nodeless inside, and replacing the true valence wave-functions by pseudo-wavefunctions. These pseudo-wavefunctions can be expanded using a much smaller number of the plane wave basis states.

- To add easily the relativistic effects into the pseudo-potential whilst further treating the valence electrons non–relativistically.

When the Kohn-Sham equation is solved, firstly the energy eigenvalues for the pseudo-potential must be matched those that would be found from the real potential in order to obtain a reasonable pseudo-potential. Secondly, the long range effect of the pseudo-potential must be the same as that of the real potential. This is resolved by ensure that the two potentials are coincided outside of the core radius (r_c).

The pseudo-potential is different than the real potential within the core radius and how once the Kohn-Sham equation is solved using the pseudo-potential, the resulting

pseudo-wavefunction will not match the real wavefunction inside r_c. The pseudo-potential is constructed in such a way that there are no radial nodes in the pseudo-wavefunction inside the core region, and clearly that the pseudo-wavefunctions and pseudo-potential coincide with their real corresponding outside of the core region, as shown in figure 2.2 .
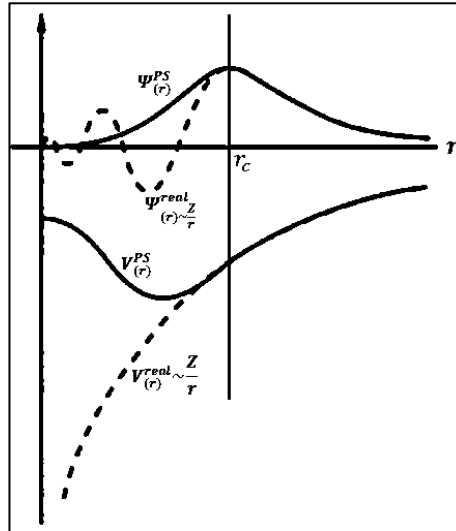
Figure 2.2 Schematic illustration of the comparison between a wavefunction in the Coulomb potential of the nucleus (dashed blue) and the one in the pseudo-potential (red). The real wavefunction and pseudo-wavefunction match above a certain cutoff radius r_c (the core radius).

The pseudo-potentials are considered within the scheme of the orthogonalized plane wave (OPW) atomic calculations. The obtained pseudo-potentials are strongly repulsive near the nuclei and the corresponding wavefunctions generally present the correct shape outside of the atomic core and differ from the correct eigenfunctions by a normalization factor [68]. In 1979, D. R. Hamann, M. Schlüter, and C. Chiang proposed a model (HSC model) to avoid these problems and allows to obtain pseudo-wavefunctions which are the same as the real wavefunctions outside of a chosen core radius (r_c) and the eigenvalues agree with the real energy eigenvalues. This property is well-known as

norm-conservation which assures that electrostatic potential caused by pseudo and real charge densities are equal when $r > r_c$ (outside of the core radius) [69]. There is a special type of ab-intio pseudo-potential which is the norm-conserving pseudo-potential (Pseudo-potentials with angular momentum dependence) in their fully non-local (Kleinman-Bylander,1982) form, which is used within SIESTA code [66,67]. For an isolated atom, the true all-electron valence wavefunctions can be expressed as:

$$\Psi_{nlm}^{R-S}(\vec{r}) = \frac{1}{r} R_{nl}^{radial}(\vec{r}) Y_{lm}^{spherical}(\vec{r}) \tag{2.38}$$

here $n, l \; and \; m$ are the quantum numbers, where $n = 1,2, \ldots$, $l = 0, \ldots, n-1$ and $m = -l, \ldots, l$. In equation 2.38, the first term is the radial harmonic wavefunction and second term is the spherical harmonic wavefunction. The first part R_{nl}^{radial} is the solution to the radial Schrödinger equation which contains the all-electron potential $V_{nl}^{all-electron}$, it includes all interactions with the remaining core and valence electrons in the atom. The radial Schrödinger equation can be written as [70]:

$$-\frac{1}{2}\frac{\partial^2}{\partial r^2} R_{nl}^{radial}(r) + \left[\frac{l(l+1)}{2r^2} + V_{nl}^{all-electron}(r)\right] R_{nl}^{radial}(r) \\ = \varepsilon_{nl}^{radial} R_{nl}(r) \tag{2.39}$$

From equation (2.39) the size of the system will reduce by removing the core electrons and replacing all of the electrons potential ($V_{nl}^{all-electron}$) by the pseudo-potential (V_{nl}^{PS}), whilst the valence electrons feel the same interaction as if they were still present. This will change the solution of (2.39) to the radial pseudo-wavefunction (R_{nl}^{PS}). The logical steps of finding this pseudo-potential are firstly to construct the pseudo-wavefunctions

from the all-electron wavefunction and then secondly to determinate the pseudo-potential by taking the inverse of the radial Schrödinger equation given by:

$$V^{PS} = \varepsilon_{nl}^{PS} - \frac{l(l+1)}{2r^2} + \frac{1}{2rR_{nl}^{PS}} \frac{\partial^2}{\partial r^2} (rR_{nl}^{PS}) \qquad (2.40)$$

Now there is a need to explain how the radial pseudo-potential is calculated, although there are many different ways of parameterising the pseudo-wavefunction.

Troullier-Martine method is another pseudo-potential used in SEISTA which is applied [70,71], where the pseudo-wavefunction is defined when $r > r_c$ as a function of a polynomial in r^2:

$$P(\vec{r}) = a_o + a_2 r^2 + a_4 r^4 + a_6 r^6 + a_8 r^8 + a_{10} r^{10} a_{12} r^{12} \qquad (2.41)$$

and it is shown as the following equation:

$$R_{nl}^{PS} = \begin{cases} R_{nl}^{radial} & \text{if } r > r_c \\ r^l e^{p(\vec{r})} & \text{if } r < r_c \end{cases} \qquad (2.42)$$

The following conditions (the conditions must be obeyed by the radial part of the pseudo-wavefunction, equation 2.43) must be satisfied by pseudo-potentials to be classified as norm-conserving pseudo-potentials:

1- The valence eigenvalues of the true all-electron potential and the pseudo-potential are the same. It is a certain condition which guarantees that for single atomic configuration, the true all-electron potential and the pseudo-potential will give the same eigenenergies :

$$\varepsilon_{nl}^{real} = \varepsilon_{nl}^{PS} \qquad (2.43)$$

The valence eigenfunctions of the true all-electron potential and the pseudo-potential must be same for a chosen core radius (r_c) and when $r > r_c$. This condition is a guarantee that in the bonding region (core region) and away from the core, the wavefunctions match as well:

$$R_{nl}^{real} = R_{nl}^{PS} \quad when \quad r > r_c \qquad (2.44)$$

The pseudo-wavefunction should be smooth and nodeless in order to obtain a smooth pseudo-potential. This can be achieved by taking the first four derivatives continuous at the cutoff radius (r_c) for the pseudo-wavefunction.

$$\left[\frac{d^i R_{nl}(\vec{r})}{dr^i}\right]_{r=r_c} = \left[\frac{d^i R_{nl}^{PS}(\vec{r})}{dr^i}\right]_{r=r_c}, \qquad \forall\, i = 1, \dots, 4$$

2- The total charge of the true and pseudo all-electron eigenfunctions when $r < r_c$ are the same.

$$\int_0^{r_c} r^2 \left|R_{nl}^{real}(\vec{r})\right|^2 d\vec{r} = \int_0^{r_c} r^2 \left|R_{nl}^{PS}(\vec{r})\right|^2 d\vec{r} \quad when \quad r < r_c \qquad (2.45)$$

By substituting equation (2.43) into the inverted Schrödinger equation (2.41) the unknown coefficient can be calculated which dives the explicit of the pseudo-potential as:

$$V_{nl}^{PS} = \begin{cases} V_{nl}^{real} & if \ r > r_c \\ \varepsilon_{nl}^{PS} - \dfrac{(l+1)p'(\vec{r})}{2r^2} + \dfrac{[p'(\vec{r}) + p''(\vec{r})]}{2} & if \ r < r_c \end{cases} \qquad (2.46)$$

In equation (2.47) the pseudo-potential is defined as *screened pseudo-potential* as it includes effects of the core and the valence electrons. In order to make the resulting pseudo-potential reliable, it should be transferable (i.e. it is possible to use it in molecules and other complicated environments) and to achieve this, any screening from the valence electrons has to be removed by subtracting the Hartree and exchange-correlation potentials. Therefore it is possible to write the ion pseudo-potential as:

$$V_{nl}^{ion}[n^{PS}(\vec{r})] = V_{nl}^{PS}[n^{PS}(\vec{r})] - V_{Hartree}[n^{PS}(\vec{r})] - V_{xc}[n^{PS}(\vec{r})] \qquad (2.47)$$

Localised Atomic Orbital Basis Sets (LAOBs)

The type of the basis function employed in the calculations is one of the most important aspects of the SIESTA code. It uses a basis set composed of localised atomic orbitals which compare well with other DFT schemes which may use a plane wavefunction basis set [66]. LAOBs provide a closer representation of the chemical bond; they can allow order-N calculations to be performed and also it gives a good base from which generate a tight-binding Hamiltonian. SIESTA uses confined orbitals, i.e. orbitals are constrained to be zero outside of a certain radius (cutoff radius r_c). This produces the desired sparse form of the Hamiltonian as the overlap between basis functions is

reduced. The atomic orbitals inside this radius are products of a numerical radial function and a spherical harmonic.

The single-ζ (also called minimal) is the simplest form of the atomic basis set for an atom (labelled as I) which represents a single basis function per electron orbital and is given by the following equation:

$$\Psi^{I}_{nlm}(\vec{r}) = \frac{1}{r} R^{I}_{nl}(\vec{r}) Y^{I}_{lm}(\vec{r}) \qquad (2.48)$$

Here the single basis function $\Psi^{I}_{nlm}(\vec{r})$ consists of two parts, the first part is the radial R^{I}_{nl} and the second part is the spherical harmonic Y^{I}_{lm}. Minimal or single zeta basis set are constructed by using one basis function of each type occupied in the separate atoms that comprise a molecule. If at least one *p-type* orbital is occupied in the atom, then the complete set (*3p-type*) of the functions must be included in the basis set. For example, in the carbon atom, the electron configuration is $1s^2\ 2s^2\ 2p^2$, therefore, a minimal basis set for carbon atom consists of $1s, 2s, 2p_x, 2p_y$ and $2p_z$ orbitals which means the total basis functions are five as shown in table 2.1.

Multiple-ζ are called higher accuracy basis sets and they are formed by adding another radial wavefunctions for each included electron orbital. Double basis sets are constructed by using two basis functions of each type for each atom. For carbon atom, a double zeta basis contains ten basis functions corresponding to ten orbitals which are $1s, 1s', 2s, 2s', 2p_x, 2p_x', 2p_y, 2p_y',\ 2p_z$ and $2p_z'$. For further accuracy, polarisation effects are included in double-ζ polarised basis sets obtained by including wavefunctions with different angular momenta corresponding to orbitals which are

unoccupied in the atom. A polarization function is any higher angular momentum orbital used in a basis set which is unoccupied in the separated atom. For instance, the hydrogen atom has only one occupied orbital type that is *s*-type. Therefore, if *p*-type or *d*-type basis functions were added to the hydrogen atom they would be known as polarization functions. Carbon atoms with polarization functions include *d*-type and *f*-type basis functions.

$$H^1/\ 1s$$

$$C^6/\ 1s,\ 2s,\ 2p_x2p_y2p_z$$

$$Cl^{17}\ /\ 1s, 2s, 2p_x, 2p_y, 2p_z\ ,3s, 3p_x, 3p_y, 3p_z$$
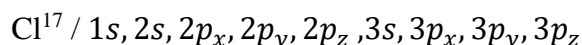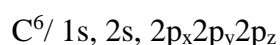
Table 2.1 Examples of the radial basis sets functions per atom used in SIESTA code for different precisions of the split valence basis sets.

Atom/Basis Functions	Single-ζ (SZ)	Double-ζ (DZ)	Single-ζ Polarised (SZP)	Double-ζ Polarised (DZP)
$H^1/1s$	1	2	4	5
$C^6/1s\ 2s\ 2p_x2p_y2p_z$	4	8	9	13

The split valence basis set is formed when the core electrons (non-valence electrons) of an atom are less affected by the chemical environment than the valence electrons. Take carbon atom, for example, a split valence double zeta basis set would consist of a single $1s$ orbital, along with $2s, 2s'$ and $2p_x, 2p_x', 2p_y, 2p_y',\ 2p_z, 2p_z'$ orbitals, for a total of 17 basis functions like Chlorine. The basis functions in a split valence double zeta basis set are denoted

$$1s, 2s, 2s', 2p_x, 2p_x', 2p_y, 2p_y', 2p_z\ ,2p_z', 3s, 3s', 3p_x, 3p_x', 3p_y, 3p_y',\ 3p_z\ ,3p_z'$$
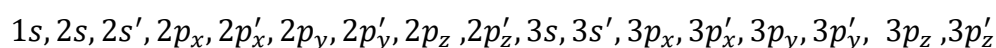
In case of molecules, molecular orbitals can be represented as Linear Combinations of Atomic Orbitals (LCAO-MO) given by:

$$\varphi_i(\vec{r}) = \sum_{v=1}^{L} a_{vi}\ \Psi_v(\vec{r})\qquad(2.49)$$

where φ_i represents the molecular orbitals (basis functions), Ψ_v are atomic orbitals, a_{vi} are numerical coefficients and L is the total number of the atomic orbitals.

Basis Set Superposition Error Correction (BSSE) and Counterpoise Correction (CP)

In the case of localized basis sets, as it is in SIESTA, there is basis set superposition error (BSSE) present and we have to correct for different basis sets of the two configurations. In quantum chemistry, calculations using finite basis sets are susceptible to BSSE. As the atoms of interacting molecules (or of different parts of the same molecule) approach one another, their basis functions overlap. Each monomer "borrows" functions from other nearby components, effectively increasing its basis set and improving the calculation of derived properties such as energy. If the total energy is minimized as a function of the system geometry, the short-range energies from the mixed basis sets must be compared with the long-range energies from the unmixed sets, and this mismatch introduces an error. Other than using infinite basis sets, two methods exist to eliminate the BSSE.

In this research work the SIESTA implementation of DFT means that the BSSE occurs when using the linear combination of the atomic orbitals formalism which consists of a finite basis set centred on the nuclei, when atoms are close enough to each other so that their basis functions will overlap. This might cause artificial strengthening of the atomic interaction and artificial shortening of the atomic distances and therefore this can affect the total energy of the system.

A technique to eliminate the BSSE in molecular complexes composed of two geometric configurations so-called the counterpoise correction (CP) scheme, was proposed by Boys and Bernardi in 1970 [72,74]. Suppose that two molecular systems labelled as A and B are separated by a distance R. The overall energy of the supersystem ΔE_{inter}^{AB} of the interaction may be expressed as [75]:

$$\Delta E_{inter}^{AB}(\vec{R}) = E^{AB}(\vec{R}) - E^A - E^B \tag{2.50}$$

where E^A and E^B are the energies of the isolated subsystems.

The form of equation 2.51 shows the counterpoise correction [72]. Figure 2.3 highlights the counterpoise correction for a dimer which are A and B.
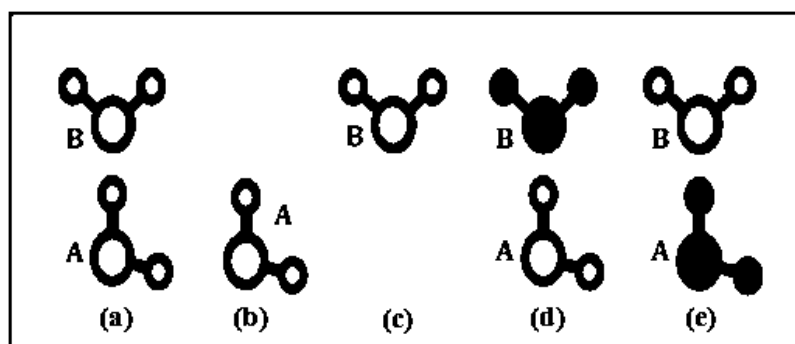
Figure 2.3 Illustrating the Counterpoise method to calculate the binding energy. (a) Represents the basis functions for total system where atoms are white colour and the basis functions of the atoms are black. (b) and (c) show the basis function for the individual monomers whereas (d) and (e) represent the counterpoise correction, every single molecule is evaluated with the same basis function as the total system in (a)[73].

Parts a, b and c in figure 2.3 represent the two isolated molecules with their individual and corresponding basis functions while the shaded gray atoms in parts d and e represent the ghost states (basis set functions which have no electrons or protons). The BSSE is obtained by recalculating using the mixed basis sets realised by introducing the ghost orbitals, and then subtracting the error from the uncorrected energy to calculate the binding energy E_{Bin} given by:

$$E_{Bin} = E_a - (E_d + E_e) \qquad (2.51)$$

where E_a, E_d and E_e are the total energy of (a), (d) and (e) systems in figure 2.3, respectively. This is an important concept that has been successfully implemented in many systems to give reliable and realistic results [73,76,77].

Structure Optimisation

In this thesis, the SIESTA code is used to obtain the ground state energy of different atomic configurations, and then obtain the relaxed structure of the systems. SIESTA can provide the energy as a function of the atomic coordinates (position of atoms). The structure optimisation which is also known as geometry optimisation contains three

options; relaxing atomic coordinates, allowing periodic cell shapes and volumes to change. For full optimisation, the three options can be employed together, which then will lead to the minimum energy of the atoms in the system and the equilibrium lattice parameters of the systems. Performing the relaxation of the atomic positions allows atoms to move until the residual force between all atoms is smaller than the required convergence tolerance in eV/Å. In structural optimisation the key quantity is the force which could be calculated numerically by taking the approximate numerical derivatives of the total energy with respect to the positions. This method is applied in SIESTA using the Hellmann-Feynman theorem [78]. Consider a Hamiltonian $H_{(\vec{R})}$ which depends on position $\vec{R}$ of an atom and $\left| \Psi_{(\vec{R})} \right\rangle$ is the wavefunction, then the Schrödinger equation can be written as:

$$H_{(\vec{R})} \left| \Psi_{(\vec{R})} \right\rangle = E \left| \Psi_{(\vec{R})} \right\rangle \tag{2.52}$$

The Hellmann-Feynman theorem relates the derivative of the total energy which can be obtained by calculating the expectation value of the derivative of the Hamiltonian $H_{(\vec{R})}$ with respect to $\vec{R}$. This can be written as in the following:

$$\frac{\partial}{\partial \vec{R}} E = \frac{\partial}{\partial \vec{R}} \left\langle \Psi_{(\vec{R})} \middle| H_{(\vec{R})} \middle| \Psi_{(\vec{R})} \right\rangle =$$

$$\left\langle \frac{\partial}{\partial \vec{R}} \Psi_{(\vec{R})} \middle| H_{(\vec{R})} \middle| \Psi_{(\vec{R})} \right\rangle + \left\langle \Psi_{(\vec{R})} \middle| \frac{\partial}{\partial \vec{R}} H_{(\vec{R})} \middle| \Psi_{(\vec{R})} \right\rangle + \left\langle \Psi_{(\vec{R})} \middle| H_{(\vec{R})} \middle| \frac{\partial}{\partial \vec{R}} \Psi_{(\vec{R})} \right\rangle =$$

$$E \left\langle \frac{\partial}{\partial \vec{R}} \Psi_{(\vec{R})} \Big| \Psi_{(\vec{R})} \right\rangle + \left\langle \Psi_{(\vec{R})} \Big| \frac{\partial}{\partial \vec{R}} H_{(\vec{R})} \Big| \Psi_{(\vec{R})} \right\rangle + E \left\langle \Psi_{(\vec{R})} \Big| \frac{\partial}{\partial \vec{R}} \Psi_{(\vec{R})} \right\rangle =$$

$$E \underbrace{\frac{\partial}{\partial \vec{R}} \left\langle \Psi_{(\vec{R})} \Big| \Psi_{(\vec{R})} \right\rangle}_{\substack{\left\langle \Psi_{(\vec{R})} \mid \Psi_{(\vec{R})} \right\rangle = 1, \\ \frac{\partial}{\partial \vec{R}} \left\langle \Psi_{(\vec{R})} \mid \Psi_{(\vec{R})} \right\rangle = 0}} + \left\langle \Psi_{(\vec{R})} \Big| \frac{\partial}{\partial \vec{R}} H_{(\vec{R})} \Big| \Psi_{(\vec{R})} \right\rangle = \left\langle \Psi_{(\vec{R})} \Big| \frac{\partial}{\partial \vec{R}} H_{(\vec{R})} \Big| \Psi_{(\vec{R})} \right\rangle$$

$$\therefore \quad \frac{\partial}{\partial \vec{R}} E = \left\langle \Psi_{(\vec{R})} \Big| \frac{\partial}{\partial \vec{R}} H_{(\vec{R})} \Big| \Psi_{(\vec{R})} \right\rangle \tag{2.53}$$

Since the acting force (F) is the derivative of the total energy with the respect to $\vec{R}$ it can be written as:

$$F = -\frac{\partial}{\partial \vec{R}} E = -\left\langle \Psi_{(\vec{R})} \Big| \frac{\partial}{\partial \vec{R}} H_{(\vec{R})} \Big| \Psi_{(\vec{R})} \right\rangle \tag{2.54}$$

Although, the wavefunction does depend on the atomic coordinates, due to normalisation, the terms containing the wavefunction derivatives with respect to $\vec{R}$ vanish, yielding the Hellmann-Feynman theorem.

Chapter 3

Green's Function and Single Electron Transport

3.1. Introduction

In this chapter a theory of single particle transport is discussed, which forms the main numerical tool for studying transport through buckyballs. The aim is to understand, the electrical and thermoelectrical properties of molecular junctions where a molecule (or sufficiently small structure) is bound to bulk electrodes. The coupling strength between the leads and the molecule is usually small compared to the intra-electrode or intra-molecule bond strengths. The electronic properties are no longer well described by the band structure since this system is not periodic. Hence a general approach is needed to understand the scattering process in the electrode junction and the molecular bridge. This can be achieved through the Green's function formalism described below.

First this chapter describes a brief overview of the Landauer formula. Following this, the simplest formula of a retarded Green's function for a one-dimensional tight binding chain is discussed. Afterwards the periodicity of this lattice at a single connection is broken to show that the Green's function is related directly to the transmission coefficient across the scattering region. Negligible interaction between carriers and the absence of inelastic processes are assumed in the method presented in this chapter.

3.2. The Landauer Formula

The standard way to describe elastic transport phenomena in mesoscopic systems is the Landauer formula and is applicable for phase coherent systems, where to describe the electronic flow a single wavefunction is sufficient [79,80]. It relates the conductance of a mesoscopic sample to the transmission properties of electrons passing through it. The method used to calculate the transmission properties will be discussed later in this Chapter.
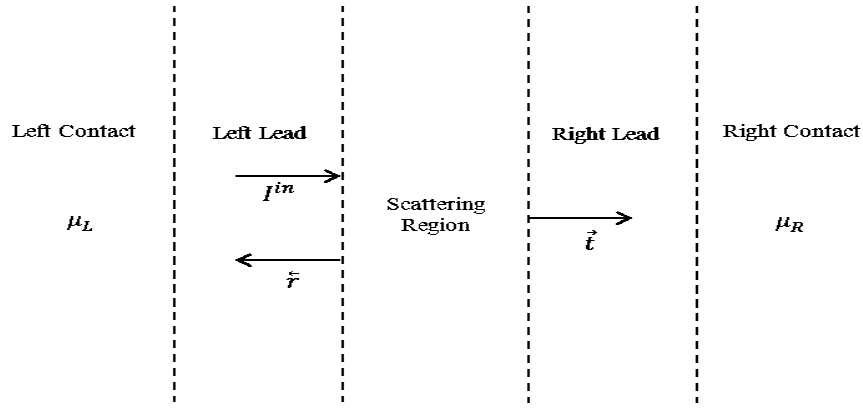
Figure 3.1: A 1-dimensional mesoscopic scatterer connected to contacts by ballistic leads. The chemical potentials in the left and right contacts are μ_L and μ_R respectively. If an incident wave packet hits the scatterer from the left, it will be transmitted to the right with probability $T = \left|\vec{t}\right|^2 = \vec{t}\vec{t}^*$ and reflected with probability $R = |\overleftarrow{r}|^2 = \overleftarrow{r}\overleftarrow{r}^*$. Since incident electrons must be either reflected or transmitted, probability conservation implies $R + T = 1$.

In figure 3.1 a 1-dimensional mesoscopic scatterer is connected to the two contacts, which behave as electron reservoirs, by means of two ideal ballistic leads. All inelastic relaxation processes are limited to the reservoirs [81]. The chemical potentials in the reservoir are $\mu_L > \mu_R \implies \mu_L - \mu_R = \delta E = e\delta V > 0$, which are slightly different and

will drive electrons from the left reservoir to the right one. Initially, the solution for one open channel will be discussed (*i.e.* where only one electron is allowed to travel in a given direction).

The first step is to analyse the incident electric current (δI^{in}) generated by the chemical potential difference to calculate the current in such a system:

$$\delta I^{in} = e v_g \frac{\partial n}{\partial E} \delta E = e v_g \frac{\partial n}{\partial E} (\mu_L - \mu_R) \qquad (3.1)$$

here e is the electronic charge

v_g is the group velocity

$\partial n / \partial E$ is the density of states (DOS) per unit length in the lead in the energy window defined by the chemical potentials of the contacts:

$$DOS = \frac{\partial n}{\partial E} = 2 \left(\frac{\partial n}{\partial k} \frac{\partial k}{\partial E} \right) \qquad (3.2)$$

where the factor of 2 accounts for spin.

In one dimension, $\partial n / \partial k = 1/2\pi$ and $\partial k / \partial E = 1/\hbar v_g$ which will simplify equation (3.1) to:

$$\delta I^{in} = \frac{2e}{h} (\mu_L - \mu_R) = \frac{2e^2}{h} \delta V \qquad (3.3)$$

δV is the voltage associated with the chemical potential mismatch. It is clear from equation (3.3) that in the absence of a scattering region, the conductance of a quantum wire with one open channel is $2e^2/h$ which is approximately 77.5 μS (or alternatively

a resistance of $12.9k\Omega$). Typically it appears on the circuit boards of everyday electrical appliances and therefore it can be said that it is reasonable quantity;

Now the current collected in the right contacts (δI^{out}) will be, if a scattering region is considered:

$$\delta I^{out} = \delta I^{in} T = \frac{2e^2}{h} T \, \delta V \Longrightarrow \frac{\delta I^{out}}{\delta V} = \frac{2e^2}{h} T = \mathcal{G} \qquad (3.4)$$

This is the well-known Landauer formula that relates the conductance ($\mathcal{G}$) of a mesoscopic scatterer to the transmission probability (T) of the electrons traveling through it. The linear response conductance is described by this, hence it only holds for small bias voltages, $\delta V \approx 0$ and voltage different between electrode.

Büttiker has generalized the above formula to the case of more than one open channel [80]. The transmission coefficient has been replaced by the sum of all the transmission amplitudes in this case which is describing electrons incoming from the left contact and arriving to the right contact. The Landauer formula that is equation (3.3) for the open channels hence becomes:

$$\frac{\delta I^{out}}{\delta V} = \mathcal{G} = \frac{2e^2}{h} \sum_{ij} \left| \vec{t}_{ij} \right|^2 = \frac{2e^2}{h} Trace\left(\vec{t}\vec{t}^{\dagger}\right) \qquad (3.5)$$

In equation (3.5) $\vec{t}_{ij}$ is the transmission amplitude describing scattering from the jth channel of the left lead to the ith channel of the right lead. The reflection amplitudes

$\overleftarrow{r}_{ij}$ can also be introduced with the definition of the transmission amplitudes which describe scattering processes where the particle is scattered from the jth channel of the left lead to the ith channel of the same lead. An S matrix can be defined combining reflection and transmission amplitudes connecting states coming from the left lead to the right lead and vice versa:

$$S = \begin{pmatrix} \overleftarrow{r} & \overleftarrow{t} \\ \overrightarrow{t} & \overrightarrow{r} \end{pmatrix} \qquad (3.6)$$

here $\overleftarrow{r}$ and $\overrightarrow{t}$ describe electrons coming from the left, while $\overrightarrow{r}$ and $\overleftarrow{t}$ describe electrons coming from the right. Also $\overleftarrow{r}, \overrightarrow{t}, \overrightarrow{r}$ and $\overleftarrow{t}$ are matrices for more than one channel, and could be complex (in the presence of a magnetic field for example) as suggested by equation (3.5). The S matrix must be unitary; $SS^\dagger = I$ as required by charge conservation which a central object of scattering theory. In the linear response regime it is useful in describing transport. It is also useful in other problems, such as adiabatic pumping [82].

It is well known since the early 19th century that there is a strong connection between heat, current, temperature and voltage with the discovery of the Seebeck, Peltier and Thompson effects. Due to a temperature difference the electric current is produced described by Seebeck effect. Peltier and Thompson effects describe the heating or cooling of a current carrying conductor [83]. Due to a temperature $\Delta\mathcal{T}$ and potential drop ΔV across the system, both charge and heat currents could be caused to flow.

For both the charge (I) and heat (Q) currents in the linear bias and temperature regime the generalised Landauer-Büttiker formulae is shown which is used to find an expressions of the thermoelectric coefficients of a two terminal device. A system consisting of a scattering region connected to two leads which are in turn connected to two electron reservoirs. According to a chemical potential μ_L and μ_R, temperature $\mathcal{T}_L$ and $\mathcal{T}_R$, and Fermi distribution function define each reservoir [83]:

$$f_i(L, R)(E) = (1 + e^{\frac{E - \mu_i}{k_{\text{BT}} \mathcal{T}_i}})^{-1} \tag{3.7}$$

It is reasonable to assume that the reservoirs are connected to the leads in a way such that there is no scattering at their interface, so all scattering effects are caused by the central scattering region. The right moving charge current of a single k-state emanating from the left reservoir can be written in terms of the number of electrons per unit length n, Fermi distribution f_L, group velocity v_g and transmission coefficient T of the scattering region. (Here T represents the transmission probability, and $\mathcal{T}$ is the temperature).

$$I_k^+ = n e v_g(E(k)) \, T\big(E(k)\big) \, f_L(E(k)) \tag{3.8}$$

By summing over all positive k states and converting to the integral form the total charge current from the right moving states can be found, where $n = 1/L$ for the density of electrons and $v_g = \frac{1}{\hbar} \frac{\partial E(k)}{\partial k}$.

$$I_k^+ = \sum_k e \, \frac{1}{L} \frac{1}{\hbar} \frac{\partial E(k)}{\partial k} \, T(E(k)) \, f_L(E(k)) = \int_{-\infty}^{+\infty} \frac{2e}{h} \, T(E) f_L(E) \, dE \tag{3.9}$$

For the left moving states:

$$I_k^- = \int_{-\infty}^{+\infty} \frac{2e}{h} T(E) f_R(E) \, dE$$

(3.10)

The total current moving to the right is hence:

$$I = I^+ - I^- = \frac{2e}{h} \int_{-\infty}^{+\infty} T(E) \left(f_L(E) - f_R(E) \right) dE$$

(3.11)

The famous Landauer- Büttiker formula is given in equation (3.11).

For the heat / energy current, a similar derivation can be carried out of the same system by starting with the relation $Q = Env_g$ rather than $I = nev_g$. The result contains two extra energy terms, however.

$$Q = Q^+ - Q^- = \frac{2}{h} \int_{-\infty}^{+\infty} T(E) \left((E - \mu_L) f_L(E) - (E - \mu_R) f_R(E) \right) dE$$

(3.12)

where:

$$f_L(E) = \left[1 + e^{\frac{E - \mu - \frac{\Delta\mu}{2}}{k_b \left(\mathcal{T} + \frac{\Delta\mathcal{T}}{2} \right)}} \right]^{-1}, \quad f_R(E) = \left[1 + e^{\frac{E - \mu + \frac{\Delta\mu}{2}}{k_b \left(\mathcal{T} - \frac{\Delta\mathcal{T}}{2} \right)}} \right]^{-1}$$

(3.13)

and

$$\mu_L = \mu + \frac{\Delta\mu}{2}, \quad \mu_R = \mu - \frac{\Delta\mu}{2}$$

(3.14)

3.3. One-Dimension

It is useful to calculate the scattering matrix for a simple one-dimensional structure before presenting the generalized methodology to give a clear outline of the methodology used in this thesis. In the derivation Green's functions is used, so for a simple one dimensional discretised lattice, the form of Green's function is discussed first (section perfect 1D lattice). Afterwards the calculations for the scattering matrix of a one-dimensional scatterer will be discussed (section 1D scattering).

Perfect One-Dimensional Lattice

The form of the Green's function for a simple infinite one-dimensional chain with on-site energies (ε_o) is discussed in this section, along with hopping parameters ($-\gamma$) as shown in Figure 3.2.
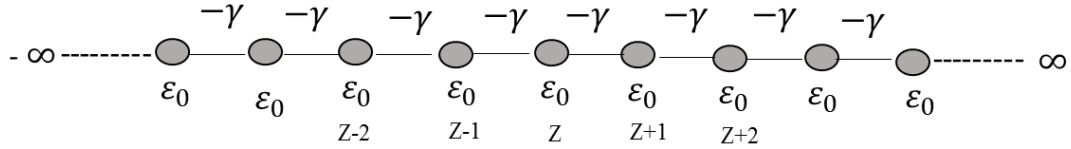
Figure 3.2: Tight-binding approximation of a one-dimensional periodic lattice with on-site energies ε_o and couplings $-\gamma$.

The Hamiltonian is constructed with the on-site energies (ε_o) along the diagonal and is of infinite extent, and the hopping elements ($-\gamma$) along the first off-diagonal. The Hamiltonian in matrix form is given as:

$$H = \begin{pmatrix} \bullet & \bullet & 0 & 0 & 0 & 0 & 0 & 0 \\ \bullet & \bullet & \bullet & 0 & 0 & 0 & 0 & 0 \\ 0 & \bullet & \varepsilon_o & -\gamma & 0 & 0 & 0 & 0 \\ 0 & 0 & -\gamma^* & \varepsilon_o & -\gamma & 0 & 0 & 0 \\ 0 & 0 & 0 & -\gamma^* & \varepsilon_o & -\gamma & 0 & 0 \\ 0 & 0 & 0 & 0 & -\gamma^* & \varepsilon_o & \bullet & 0 \\ 0 & 0 & 0 & 0 & 0 & \bullet & \bullet & \bullet \\ 0 & 0 & 0 & 0 & 0 & 0 & \bullet & \bullet \end{pmatrix} \qquad (3.15)$$

Within the tight-binding approximation and substituting equation (3.15) and the wavefunction into the Schrödinger equation $(E - H)\Psi_{(z)} = 0$:

$$\begin{pmatrix} \bullet & \bullet & \bullet & \bullet & \bullet & \bullet & \bullet & \bullet \\ \bullet & \bullet & \bullet & \bullet & \bullet & \bullet & \bullet & \bullet \\ \bullet & -\gamma^* & (E - \varepsilon_o) & -\gamma & 0 & 0 & 0 & \bullet \\ \bullet & 0 & -\gamma^* & (E - \varepsilon_o) & -\gamma & 0 & 0 & \bullet \\ \bullet & 0 & 0 & -\gamma^* & (E - \varepsilon_o) & -\gamma & 0 & \bullet \\ \bullet & 0 & 0 & 0 & -\gamma^* & (E - \varepsilon_o) & -\gamma & \bullet \\ \bullet & \bullet & \bullet & \bullet & \bullet & \bullet & \bullet & \bullet \\ \bullet & \bullet & \bullet & \bullet & \bullet & \bullet & \bullet & \bullet \end{pmatrix} \begin{pmatrix} \bullet \\ \bullet \\ \Psi_{(z-1)} \\ \Psi_{(z)} \\ \Psi_{(z+1)} \\ \Psi_{(z+2)} \\ \bullet \\ \bullet \end{pmatrix} = \begin{pmatrix} \bullet \\ \bullet \\ 0 \\ 0 \\ 0 \\ 0 \\ \bullet \\ \bullet \end{pmatrix} \qquad (3.16)$$

For row $'z'$ of the hamiltonian (H) the Schrödinger equation can be written as:

$$-\gamma^*\Psi_{(z-1)} + (E - \varepsilon_o)\Psi_{(z)} - \gamma\Psi_{(z+1)} = 0 \qquad (3.17)$$

For any function $\Psi_{(z)}$ to be a wave function it must satisfy the Schrödinger equation given above in (3.17). The wavefunction for this perfect lattice takes the form of a propagating Bloch state (equation (3.18)), normalised by its group velocity (v_g) in order for it to carry unit current flux. After substituting into equation (3.17) (assuming that $\gamma = \gamma^*$, if γ is real), it leads to one-dimensional energy dispersion relation given in equation (3.19)):

$$\Psi_{(z)} = \frac{1}{\sqrt{v_g}} e^{ikz} \tag{3.18}$$

$$E = \varepsilon_o - 2\gamma \cos k \tag{3.19}$$

The quantum number (k) is introduced which is commonly referred to as the wavenumber. The retarded Green's function $\mathcal{G}(z, z')$ is the solution to an equation very similar to that of the Schrödinger equation and is closely related to the wave-function:

$$(E - H)\,\mathcal{G}(z, z') = \delta_{(z,z')} \;\;\Rightarrow$$

$$-\gamma^*\mathcal{G}(z - 1, z') + (E - \varepsilon_o)\,\mathcal{G}(z, z') - \gamma\,\mathcal{G}(z + 1, z') = \delta_{(z,z')} \tag{3.20}$$

Here

$$\delta_{(z,z')} = 1, \qquad if \; z = z'$$

$$\delta_{(z,z')} = 0, \qquad if \; z \neq z'$$

The response of a system at a point z due to an excitation at a point z' describes the retarded Green's function, $\mathcal{G}(z, z')$. Such an excitation is expected to give rise to two waves, traveling outwards from the point of excitation, with amplitudes $\mathcal{B}$ and $\mathcal{D}$ as shown in figure 3.3.
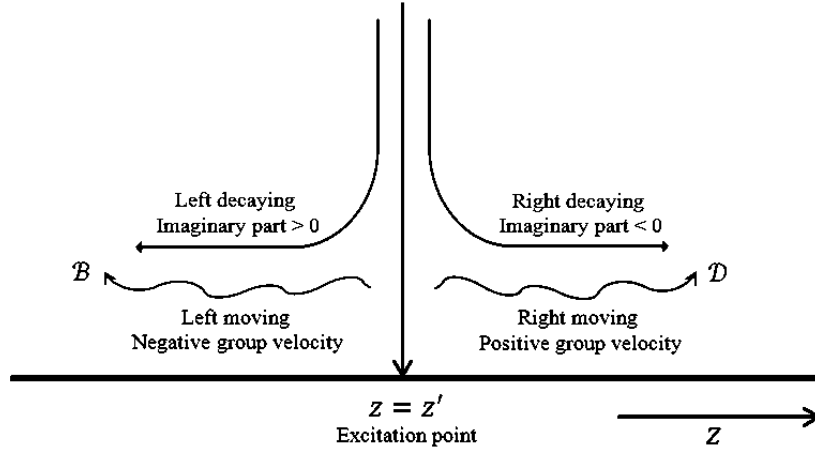
Figure 3.3: The structure of Retarded Green's Function of an infinite one-dimensional lattice. The excitation at $z = z'$ causes wave to propagate left and right (the blue modes are the open channels) with amplitudes $\mathcal{B}$ and $\mathcal{D}$ respectively, while the red represent the decaying modes.

These waves can be expressed as:

$$\mathcal{g}(z, z') = \begin{cases} \mathcal{D}\, e^{ikz}, & z > z' \\ \mathcal{B}\, e^{-ikz}, & z < z' \end{cases} \tag{3.21}$$

This solution satisfies equation (3.20) at every point, except at $z = z'$. The Green's function must be continuous (equation (3.22)) to overcome this, so the two equations are equated at $z = z'$

$$[\mathcal{g}(z, z')]_{Left} = [\mathcal{g}(z, z')]_{Right} \tag{3.22}$$

$$\mathcal{B}e^{-ikz'} = \mathcal{D}e^{ikz'} \tag{3.23}$$

$$\mathcal{B} = \mathcal{D}e^{2ikz'} \tag{3.24}$$

Substituting equation (3.11) into (3.21) gives:

$$g(z, z') = \begin{cases} \mathcal{D}\, e^{ikz} & , \quad z \geq z' \\ \mathcal{D}e^{2ikz'}e^{-ikz} = \mathcal{D}e^{ikz'}e^{ik(z'-z)}, & z \leq z' \end{cases} \tag{3.25}$$

A re-writing of the equation (3.25) of these reveals a useful symmetry:

$$g(z, z') = \begin{cases} \mathcal{D}e^{ikz'}e^{ik(z-z')}, & z \geq z' \\ \mathcal{D}e^{ikz'}e^{ik(z'-z)}, & z \leq z' \end{cases} \tag{3.26}$$

It is simply clear that the power of complex exponent is always positive, therefore the latter equation can be written such as:

$$g(z, z') = \mathcal{D}e^{ikz'}e^{ik|z'-z|}, \qquad \forall z \tag{3.27}$$

The Green's equation (3.20) should be considered to define the constant $\mathcal{D}$. H can be written as $-\frac{\hbar^2}{2m}\nabla^2$, or $-\frac{\hbar v_g}{2k}\nabla^2$ (where $v_g = \frac{\hbar k}{m}$ is the group velocity), and substitute in the Green's function (3.26), hence:

$$\left(E + \frac{\hbar v_g}{2k}\frac{\partial^2}{\partial z^2}\right)\left(\mathcal{D}e^{ikz'}e^{ik|z'-z|}\right) = \delta_{(z,z')} \tag{3.28}$$

If the function is integrated over a small distance, centred on z', of width $2\omega^+$, then:

$$\int_{z'-\omega^+}^{z'+\omega^+} \left(E + \frac{\hbar v_g}{2k}\frac{\partial^2}{\partial z^2}\right)\left(\mathcal{D}e^{ikz'}e^{ik|z'-z|}\right) dz = 1 \tag{3.29}$$

$$\mathcal{D}e^{ikz'}\left(\overbrace{E\int_{z'-\omega^+}^{z'+\omega^+} e^{ik|z'-z|}\,dz}^{=\text{\textbf{Zero}}} + \int_{z'-\omega^+}^{z'+\omega^+} \frac{\hbar v_g}{2k}\frac{\partial^2}{\partial z^2}e^{ik|z'-z|}\,dz\right) = 1 \qquad (3.30)$$

$$\mathcal{D}e^{ikz'}\left(\frac{\hbar v_g}{2k}\frac{\partial}{\partial z}e^{ik|z'-z|}\right)\Bigg|_{z'-\omega^+}^{z'+\omega^+} = \mathcal{D}e^{ikz'}\left(\frac{\hbar v_g}{2k}ike^{ik|z'-z|}\right)\Bigg|_{z'-\omega^+}^{z'+\omega^+} = 1 \qquad (3.31)$$

$$\mathcal{D}e^{ikz'}\frac{\hbar v_g}{2k}2ik = 1 \implies \mathcal{D}e^{ikz'} = \frac{1}{i\hbar v_g} \qquad (3.32)$$

hence the retarded Green's function:

$$\mathscr{g}^R(z,z') = \frac{1}{i\hbar v_g}e^{ik|z-z'|} \qquad (3.33)$$

From differentiating the dispersion relation the group velocity was founded which can be given as:

$$v_g = \frac{1}{\hbar}\frac{\partial E(k)}{\partial k} = \frac{2\gamma sink}{\hbar} \qquad (3.34)$$

However an alternate solution can be found to this problem [81,84,85]. Above, the retarded Green's function, $g^R(z, z')$ has been shown. The advanced (or source) Green's function, $g^A(z, z')$, is an equally valid solution:

$$g^A(z, z') = \frac{-1}{i\hbar v_g} e^{-ik|z-z'|} = \frac{i}{\hbar v_g} e^{-ik|z-z'|}$$

(3.35)

The retarded Green's function describes outgoing waves from the excitation point ($z = z'$), however the advanced Green's function describes two incoming waves that disappear at the excitation point. The retarded Green's function is used in this work and for the sake of simplicity, the ^{R} is dropped from its representation. So $g(z, z')$ $= g^R(z, z')$.

One-Dimensional Scattering

Consider the case where two pieces of one dimensional tight binding semi-infinite leads are connected by a coupling element ($-\alpha$). As shown in figure 3.4 both leads have equal on-site potentials (ε_o) and hopping elements ($-\gamma$). This system is deceptive because, though it looks simple, all one-dimensional setups can be reduced back to this topology. Therefore the analytical solutions for the transmission and reflection coefficients would be very valuable.
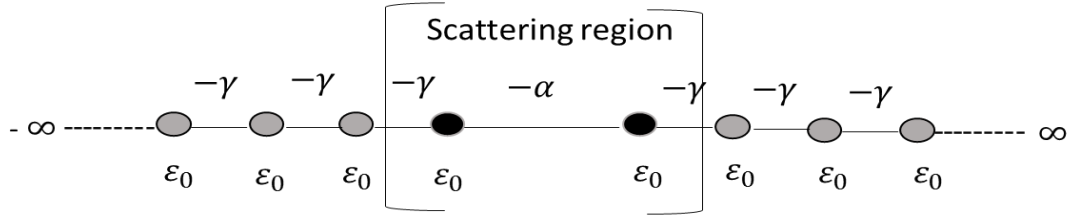
Figure 3.4: Simple tight-binding model of a one dimensional scatterer attached to one dimensional leads.

The Hamiltonian for this structure takes the form of an infinite matrix.

$$H = \begin{pmatrix} \bullet & \bullet & 0 & 0 & 0 & 0 & 0 & 0 \\ \bullet & \bullet & -\gamma & 0 & 0 & 0 & 0 & 0 \\ 0 & -\gamma^* & \varepsilon_o & -\gamma & 0 & 0 & 0 & 0 \\ 0 & 0 & -\gamma^* & \varepsilon_o & -\alpha & 0 & 0 & 0 \\ 0 & 0 & 0 & -\alpha^* & \varepsilon_o & -\gamma & 0 & 0 \\ 0 & 0 & 0 & 0 & -\gamma^* & \varepsilon_o & -\gamma & 0 \\ 0 & 0 & 0 & 0 & 0 & -\gamma^* & \bullet & \bullet \\ 0 & 0 & 0 & 0 & 0 & 0 & \bullet & \bullet \end{pmatrix} = \begin{pmatrix} H_L & V_c \\ V_c^\dagger & H_R \end{pmatrix} \tag{3.36}$$

H_L and H_R denote Hamiltonians for the leads which are the semi-infinite equivalent of the Hamiltonian shown in equation (3.7) and V_c denotes the coupling parameter. For real γ, the dispersion relation corresponding to the leads introduced above was given in equation (3.19) and the group velocity was given in equation (3.32):

$$E(k) = \varepsilon_o - 2\gamma \cos k \tag{3.37}$$

and

$$v_g = \frac{1}{\hbar} \frac{\partial E}{\partial k} \tag{3.38}$$

The Green's function of the system needs to be defined in order to obtain the scattering amplitudes and can be written as:

$$(E - H)G = I \implies G = (E - H)^{-1} \tag{3.39}$$

Equation (3.39) is singular if the energy E is equal to an eigenvalue of the Hamiltonian H. To circumvent this problem, it is practical to consider the limit:

$$G_{\mp} = \lim_{\eta \to 0} (E - H \mp i\eta)^{-1}$$

$$\tag{3.40}$$

here η is a positive number and G_- (G_+) is the retarded (advanced) Green's function. Only the retarded Green's functions is used in this thesis and hence choose the positive sign. The retarded Green's function for an infinite, one dimensional chain with the same parameters is defined in equation (3.37):

$$g_{ml} = \frac{1}{i\hbar v_g} e^{ik|m-l|} \tag{3.41}$$

the labels of the sites in the chain are m, l. The appropriate boundary conditions need to be defined in order to obtain the Green's function of a semi-infinite lead. The chain must terminate at a given point (i_o) in this case, the lattice is semi-infinite, so that all points for which $i \leq i_o$ are missing. To mathematically represent this condition it can be achieved by adding a wavefunction to the Green's function. The wave-function is:

$$\Psi^{i_o}_{ml} = -\frac{e^{ik(2i_o - m - l)}}{i\hbar v_g} \tag{3.42}$$

At the boundary ($m = l = i_o - 1$) the Green's function is the sum of equations (3.41) and (3.42) ($\mathscr{g}_{ml} = \mathscr{g}^{\infty}_{ml} + \Psi^{i_o}_{ml}$) will have the following simple form:

$$\mathscr{g}_{i_o - 1, i_o - 1} = -\frac{e^{ik}}{\gamma} \tag{3.43}$$

In case of decoupled leads ($\alpha = 0$) the total Green's function of the system will simply be given by the decoupled Green's function:

$$\mathscr{g} = \begin{pmatrix} -\dfrac{e^{ik}}{\gamma} & 0 \\ 0 & -\dfrac{e^{ik}}{\gamma} \end{pmatrix} = \begin{pmatrix} \mathscr{g}_L & 0 \\ 0 & \mathscr{g}_R \end{pmatrix} \tag{3.44}$$

If the interaction is switched on, then in order to obtain the Green's function of the coupled system (G). Now Dyson's equation is used:

$$G = (\mathscr{g}^{-1} - V)^{-1} \tag{3.45}$$

the operator V describing the interaction connecting the two leads will have the form:

$$V = \begin{pmatrix} 0 & V_c \\ V_c^\dagger & 0 \end{pmatrix} = \begin{pmatrix} 0 & \alpha \\ \alpha^* & 0 \end{pmatrix} \tag{3.46}$$

The solution to Dyson's equation, equation (3.45) reads:

$$G = \frac{1}{\gamma^2 e^{-2ik} - \alpha^2} \begin{pmatrix} -\gamma e^{-ik} & \alpha \\ \alpha^* & -\gamma e^{-ik} \end{pmatrix} \qquad (3.47)$$

In this case the remaining step is to calculate the transmission ($\vec{t}$) and reflection ($\overset{\leftarrow}{r}$) amplitudes from the Green's function equation given in equation (3.47). The Fisher-Lee relation can be used for this purpose which relates the scattering amplitudes of a scattering problem to the Green's function of the problem and it reads [81,86]:

$$\overset{\leftarrow}{r} = G_{1,1} v_g - 1 \qquad (3.48)$$

and

$$\vec{t} = G_{1,2} v_g e^{ik} \qquad (3.49)$$

These amplitudes correspond to particles incident from the left. If those particles are considered coming from the right then similar expressions could be recovered for the transmission ($\overset{\leftarrow}{t}$) and reflection ($\vec{r}$) amplitudes.

After having the full scattering matrix the Landauer formula equation (3.4) can be used to calculate the zero bias conductance. The procedure (by which this analytical solution for the conductance of a one-dimensional scatterer) was found can be generalized for more complex geometries. So to briefly summarize the steps:

1. In the first step the Green's function was calculated describing the surface sites of the leads.

2. From Dyson's equation the total Green's function in the presence of a scatterer is obtained.

3. The Fisher-Lee relation gives the scattering matrix from the Green's function.

4. The zero-bias conductance can be found using the Landauer formula.

It must be noted that the setup considered in this section looks simple but it is quite general as well. By using a technique called decimation all types of scattering regions can be reduced back to the case of two one dimensional leads.

3.4. Generalization of the Scattering Formalism

A more generalized approach to transport calculations following the derivation of Lambert *et al* are discussed in this section [87-89]. In the first step the surface Green's function of crystalline leads is computed, then to reduce the dimensionality of the scattering region the technique of decimation is introduced and finally by means of a generalization of the Fisher-Lee relation the scattering amplitudes are recovered.

Hamiltonian and Green's Function of the Leads

Firstly the term lead needs to be defined and it can be defined as, in general, it is a perfect crystalline object that acts as a perfect wave-guide for carrying excitations from reservoirs to the scattering region. A general semi-infinite crystalline electrode of arbitrary complexity is discussed in this section. The structure of the Hamiltonian is a

generalization of the one-dimensional electrode Hamiltonian in equation (3.15) because of the fact that the leads are crystalline. Figure 3.5 shows the general system.
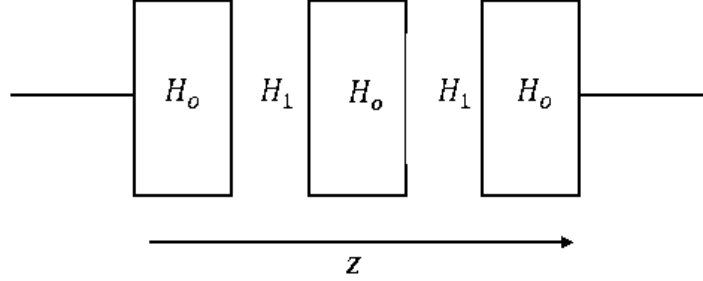
Figure 3.5: Schematic representation of a semi-infinite generalized lead. States described by the Hamiltonian H_o are connected via a generalized hopping matrix H_1. The direction z is defined to be parallel to the axis of the chain. One can assign for each slice a label z.

A Hamiltonian for each repeating layer of the bulk electrode (H_o), and a coupling matrix are used to describe the hopping parameters between these layers (H_1) instead of site energies.

For such a system the Hamiltonian has the form:

$$H = \begin{pmatrix} \bullet & \bullet & 0 & 0 & 0 & 0 & 0 & 0 \\ \bullet & \bullet & H_1 & 0 & 0 & 0 & 0 & 0 \\ 0 & H_1^\dagger & H_o & H_1 & 0 & 0 & 0 & 0 \\ 0 & 0 & H_1^\dagger & H_o & H_1 & 0 & 0 & 0 \\ 0 & 0 & 0 & H_1^\dagger & H_o & H_1 & 0 & 0 \\ 0 & 0 & 0 & 0 & H_1^\dagger & H_o & H_1 & 0 \\ 0 & 0 & 0 & 0 & 0 & H_1^\dagger & \bullet & \bullet \\ 0 & 0 & 0 & 0 & 0 & 0 & \bullet & \bullet \end{pmatrix} \qquad (3.50)$$

where H_o and H_1 are in general complex matrices and the only restriction is that the full Hamiltonian (H) should be Hermitian. The first goal is to calculate the Green's function of such a lead for general H_1 and H_o in this section. To calculate the Green's function it is necessary to calculate the spectrum of the Hamiltonian by solving the Schrödinger equation of the lead:

$$H_1^\dagger \Psi_{(z-1)} + H_o \Psi_{(z)} + H_1 \Psi_{(z+1)} = E \Psi_{(z)} \tag{3.51}$$

the wave-function $\Psi_{(z)}$ describes the layer z. The system is infinitely periodic in the z direction only, so the on-site wavefunction $\Psi_{(z)}$, can be represented in Bloch form; consisting of a product of a propagating plane wave and a wavefunction ($\Phi_{(k)}$), which is perpendicular to the transport direction (z). If the layer Hamiltonian (H_o), has dimensions $M \times M$ (or in other words consists of M site energies and their respective hopping elements), then the perpendicular wavefunction ($\Phi_{(k)}$), will have M degrees of freedom and take the form of a $1 \times M$ dimensional vector. So the wavefunction $\Psi_{(z)}$, takes the form:

$$\Psi_{(z)} = \sqrt{n_{(k)}} e^{ikz} \Phi_{(k)} \tag{3.52}$$

In equation 3.52 n_k is an arbitrary normalization parameter. If equation 3.52 is substituted into the Schrödinger equation given in (3.51), it will yield:

$$(H_o + e^{ik} H_1 + e^{-ik} H_1^\dagger - E) \Phi_{(k)} = 0 \tag{3.53}$$

The eigenvalues $[E = E_l(k)]$, where $l = 1, \ldots \ldots, M$ needs to be calculated after selecting values of k to find the band structure for such a problem. In this case, l denotes the band index. There will be M solutions to the eigenvalue problem for each value of k, and so M energy values. Therefore it is relatively simple to build up a band structure by selecting multiple values for k.

The problem is approached from the opposite direction is a scattering problem; instead of finding the values of E at a given k, the values of k is found at a given E. The wave vectors are obtainedby introducing the function and the energy is the input:

$$\theta_{(k)} = e^{-ikz}\Phi_{(k)} \rightarrow \Phi_{(k)} = e^{ikz}\theta_{(k)} \tag{3.54}$$

and when it is combined with (3.53):

$$\begin{pmatrix} -H_1^{-1}(H_o - E) & -H_1^{-1}H_1^{\dagger} \\ I & 0 \end{pmatrix} \begin{pmatrix} \Phi_{(k)} \\ \theta_{(k)} \end{pmatrix} = e^{ik} \begin{pmatrix} \Phi_{(k)} \\ \theta_{(k)} \end{pmatrix} \tag{3.55}$$

The equation (2.55) will yield $2M$ eigenvalues (e^{ik_l}) and eigenvectors ($\Phi_{(k_l)}$), of size M for a layer Hamiltonian (H_o) of size $M \times M$. According to their propagating or decaying nature and whether they are left going $z \rightarrow -\infty$ or right going $z \rightarrow \infty$ these states can be sorted into four categories. If it has a real value of k_l, and is decaying a state is propagating if it has an imaginary value of k_l. If the imaginary part of the wave

number is positive then it is a left decaying state, if it has a negative imaginary part it is a right decaying state. According to the group velocity of the state the propagating states are sorted as defined in (4.56):

$$v_g^{k_l} = \frac{1}{\hbar} \frac{\partial E_{k,l}}{\partial k}$$

(3.56)

It is a right propagating state if the state has positive group velocity ($v_g^{k_l}$), otherwise it is a left propagating state. They have been summarised in table 3.1:

Table 3.1: Sorting the eigenstates into left and right propagating or decaying states according to the wave number and group velocity.

	Left	Right
Decaying	$Im\ (k_l) > 0$	$Im\ (k_l) < 0$
Propagating	$Im\ (k_l) = 0, v_g^{k_l} < 0$	$Im\ (k_l) = 0, v_g^{k_l} > 0$

From onwards the wave numbers (k_l) which belong to the left propagating/decaying set of wave numbers will be denoted by $\bar{k}_l$ for convenience, and the right propagating/decaying wave numbers will remain plainly k_l. Therefore, $\Phi_{(k_l)}$ is a wave-function which is associated to a "right" state and $\Phi_{(\bar{k}_l)}$ is associated to a "left" state. Hence there must be exactly the same number (M) of left and right going states if H_1 is invertible. For singular H_1, the matrix in (3.55) cannot be constructed, since it relies of the inversion of H_1. To overcome this problem, however any one of several methods can be used. In the first method the decimation technique is used to create an effective, non-singular H_1 [10]. In another technique a singular H_1 is populated with small random numbers, hence introducing an explicit numerical error. This technique is quite

reasonable as the introduced numerical error can be as small as the numerical error introduced by decimation. Another solution is to rewrite equation (3.55) such that there is no need to invert H_1:

$$\begin{pmatrix} -(H_o - E) & -H_1^\dagger \\ I & 0 \end{pmatrix} \begin{pmatrix} \Phi_{(k)} \\ \theta_{(k)} \end{pmatrix} = e^{ik} \begin{pmatrix} H_1 & 0 \\ 0 & I \end{pmatrix} \begin{pmatrix} \Phi_{(k)} \\ \theta_{(k)} \end{pmatrix} \qquad (3.57)$$

However, solving this generalized eigen-problem is more computationally expensive. Any of the aforementioned methods work reasonably in tackling the problem of a singular H_1 matrix, and so can the condition that there must be exactly the same number (M) of left and right going states, whether H_1 is singular or not.

At a given wave number (k) the solutions to the eigen-problem equation (3.53) will form an orthogonal basis set. The eigenstates ($\Phi_{(k_l)}$) obtained by solving the eigen-problem equation (3.55) at a given energy (E), however will not generally form an orthogonal set of states. This is crucial, because when constructing the Green's function the non-orthogonality is to be dealt with. It is, therefore, necessary to introduce the duals to $\Phi_{(k_l)}$ and $\Phi_{(\bar{k}_l)}$ in such a way that they obey:

$$\widetilde{\Phi}_{(k_i)}^\dagger \Phi_{(k_j)} = \widetilde{\Phi}_{(\bar{k}_i)}^\dagger \Phi_{(\bar{k}_j)} = \delta_{ij} \qquad (3.58)$$

This yields the generalized completeness relation:

$$\sum_{l=1}^{M} \widetilde{\Phi}_{(k_l)}^{\dagger} \Phi_{(k_l)} = \sum_{l=1}^{M} \widetilde{\Phi}_{(\bar{k}_l)}^{\dagger} \Phi_{(\bar{k}_l)} = I \tag{3.59}$$

After getting the whole set of eigenstates at a given energy, it becomes possible to calculate the Green's function first for the infinite system and then, by satisfying the appropriate boundary conditions, for the semi-infinite leads at their surface. The Green's function can be built from the mixture of the eigen-states $\Phi_{(k_l)}$ and $\Phi_{(\bar{k}_l)}$ since it satisfies the Schrödinger equation when $z \neq z'$, it:

$$\mathcal{G}(z,z') = \begin{cases} \displaystyle\sum_{l=1}^{M} \Phi_{(k_l)} e^{ik_l(z-z')} \omega_{k_l}^{\dagger}, & z \geq z' \\ \displaystyle\sum_{l=1}^{M} \Phi_{(\bar{k}_l)} e^{i\bar{k}_l(z-z')} \omega_{\bar{k}_l}^{\dagger}, & z \leq z' \end{cases} \tag{3.60}$$

In (3.60) the M-component vectors ω_{k_l} and $\omega_{\bar{k}_l}$ are to be determined. The structural similarities between (3.60) and equation (3.21) and also that all the degrees of freedom in the transverse direction are contained in the vectors $\Phi_{(k)}$ and ω_k.

The task now is to obtain the ω vectors. As for a 1d Greens function, the equation (3.60) must be continuous at $z = z'$ and should fulfill the Green's equation (3.20).

The first condition is expressed as:

$$\sum_{l=1}^{M} \Phi_{(k_l)} \omega_{k_l}^{\dagger} = \sum_{l=1}^{M} \Phi_{(\bar{k}_l)} \omega_{\bar{k}_l}^{\dagger} \tag{3.61}$$

and the second:

$$\sum_{l=1}^{M} \left[(E - H_o)\Phi_{(k_l)}\omega_{k_l}^\dagger + H_1 e^{ik_l}\omega_{k_l}^\dagger + H_1^\dagger \Phi_{(\bar{k}_l)} e^{-i\bar{k}_l}\omega_{\bar{k}_l}^\dagger \right] = I$$

$$\sum_{l=1}^{M} \left[(E - H_o)\Phi_{(k_l)}\omega_{k_l}^\dagger + H_1 \Phi_{(k_l)} e^{ik_l}\omega_{k_l}^\dagger + H_1^\dagger \Phi_{(\bar{k}_l)} e^{-i\bar{k}_l}\omega_{\bar{k}_l}^\dagger + H_1^\dagger e^{-ik_l}\omega_{k_l}^\dagger \right.$$

$$\left. - H_1^\dagger e^{-ik_l}\omega_{k_l}^\dagger \right] = I$$

$$\sum_{l=1}^{N} \left[H_1^\dagger \Phi_{(\bar{k}_l)} e^{i\bar{k}_l}\omega_{\bar{k}_l}^\dagger - H_1^\dagger \Phi_{(k_l)} e^{-ik_l}\omega_{k_l}^\dagger \right]$$

$$+ \sum_{l=1}^{M} \left[(E - H_o) + H_1 e^{ik_l} + H_1^\dagger e^{-ik_l} \right] \Phi_{(k_l)}\omega_{k_l}^\dagger = I$$

and since, from the Schrödinger equation (3.49), it is known that:

$$\sum_{l=1}^{M} \left[(E - H_o) + H_1 e^{ik_l} + H_1^\dagger e^{-ik_l} \right] \Phi_{(k_l)} = 0 \tag{3.62}$$

This yields to:

$$\sum_{l=1}^{N} H_1^\dagger \left[\Phi_{(\bar{k}_l)} e^{i\bar{k}_l}\omega_{\bar{k}_l}^\dagger + \Phi_{(k_l)} e^{-ik_l}\omega_{k_l}^\dagger \right] = I \tag{3.63}$$

Now by making use of the dual vectors defined in equation (3.58). Multiplying equation (3.63) by $\widetilde{\Phi}_{(k_p)}$ yields:

$$\sum_{l=1}^{M} \widetilde{\Phi}_{(k_p)}^{\dagger} \Phi_{(\bar{k}_l)} \omega_{\bar{k}_l}^{\dagger} = \omega_{k_p}^{\dagger} \tag{3.64}$$

similarly multiplying by $\widetilde{\Phi}_{(\bar{k}_p)}^{\dagger}$ gives:

$$\sum_{l=1}^{M} \widetilde{\Phi}_{(\bar{k}_p)}^{\dagger} \Phi_{(k_l)} \omega_{k_l}^{\dagger} = \omega_{\bar{k}_p}^{\dagger} \tag{3.65}$$

Using the continuity equation (3.61) and equations (3.64) and (3.65), the Green's equation (equation (3.61)) becomes:

$$\sum_{l=1}^{M} \sum_{p=1}^{M} H_1^{\dagger} \left(\Phi_{(\bar{k}_l)} e^{-i\bar{k}_l} \widetilde{\Phi}_{(\bar{k}_l)}^{\dagger} - \Phi_{(k_l)} e^{-ik_l} \widetilde{\Phi}_{(k_l)}^{\dagger} \right) \Phi_{(\bar{k}_p)} \omega_{\bar{k}_p}^{\dagger} = I \tag{3.66}$$

From which it follows:

$$\sum_{l=1}^{M} \left[H_1^{\dagger} \left(\Phi_{(\bar{k}_l)} e^{-i\bar{k}_l} \widetilde{\Phi}_{(\bar{k}_l)}^{\dagger} - \Phi_{(k_l)} e^{-ik_l} \widetilde{\Phi}_{(k_l)}^{\dagger} \right) \right]^{-1}$$

$$= \sum_{p=1}^{M} \Phi_{(\bar{k}_p)} \omega_{\bar{k}_p}^{\dagger} = \sum_{p=1}^{M} \Phi_{(k_p)} \omega_{k_p}^{\dagger} \tag{3.67}$$

This immediately gives us an expressions for $\omega_k^{\dagger}$:

$$\omega_k^\dagger = \widetilde{\Phi}_{(k)}^\dagger \nu^{-1} \tag{3.68}$$

where ν is defined as:

$$\nu = \sum_{l=1}^{M} H_1^\dagger \left(\Phi_{(\bar{k}_l)} e^{-i\bar{k}_l} \widetilde{\Phi}_{(\bar{k}_l)}^\dagger - \Phi_{(k_l)} e^{-ik_l} \widetilde{\Phi}_{(k_l)}^\dagger \right) \tag{3.69}$$

The wave number (k) refers to both left and right type of states. Substituting equation (3.68) into (3.60) the Green's function of an infinite system is yielded:

$$\mathcal{G}_{z,z'}^\infty = \begin{cases} \displaystyle\sum_{l=1}^{M} \Phi_{(k_l)} e^{ik_l(z-z')} \widetilde{\Phi}_{(k_l)}^\dagger \nu^{-1}, & z \geq z' \\ \displaystyle\sum_{l=1}^{M} \Phi_{(\bar{k}_l)} e^{i\bar{k}_l(z-z')} \widetilde{\Phi}_{(\bar{k}_l)}^\dagger \nu^{-1}, & z \leq z' \end{cases} \tag{3.70}$$

As with the one dimensional case it is required to add a wave function to the Green's function in order to satisfy the boundary conditions at the edge of the lead in order to get the Green's function for a semi-infinite lead. The Green's function must vanish at a given place ($z = z_o$), is a boundary condition here. In order to achieve this we add:

$$\triangle = - \sum_{l,p=1}^{M} \Phi_{\bar{k}_l} e^{i\bar{k}_l(z-z_o)} \widetilde{\Phi}_{(\bar{k}_l)}^\dagger \, \Phi_{(k_p)} e^{ik_p(z_o-z)} \widetilde{\Phi}_{(k_p)}^\dagger \, \nu^{-1} \tag{3.71}$$

To the Green's function, equation (3.70), $\mathcal{G} = \mathcal{G}^\infty + \triangle$. This yields the surface Green's function for a semi-infinite lead going left:

$$\mathcal{G}_L = \left(I - \sum_{l,p=1}^{M} \Phi_{(\bar{k}_l)} e^{-i\bar{k}_l} \widetilde{\Phi}_{(\bar{k}_l)}^\dagger \, \Phi_{(k_p)} e^{ik_p} \widetilde{\Phi}_{(k_p)}^\dagger \right) \nu^{-1} \tag{3.72}$$

and going right:

$$\mathcal{G}_R = \left(I - \sum_{l,p=1}^{M} \Phi_{(k_l)} e^{ik_l} \widetilde{\Phi}_{(k_l)}^{\dagger} \Phi_{(\bar{k}_p)} e^{-i\bar{k}_p} \widetilde{\Phi}_{(\bar{k}_p)}^{\dagger} \right) v^{-1} \tag{3.73}$$

Using the numerical approach in equation (3.55), a versatile method has been yielded for calculating the surface Green's functions (equations (3.72) and (3.73)) for a semi-infinite crystalline electrode. The next step is to apply this to a scattering problem.

Effective Hamiltonian of the Scattering Region

For a given coupling matrix between the surfaces of the semi-infinite leads, the Dyson equation (3.45) can be used to calculate the Green's function of the scatterer. However, the scattering region is not generally described simply as a coupling matrix between the surfaces. Therefore, it is useful to use the decimation method to reduce the Hamiltonian down to such a structure [90-92]. Some other methods have been developed as discussed in [93,94], but in this thesis the decimation method is used.

Consider again the Schrödinger equation:

$$\sum_j H_{ij} \Psi_j = E\Psi_i \tag{3.74}$$

If separated from the equation (3.74) the dth degree of freedom in the system:

$$H_{id} \Psi_d + \sum_{j \neq d} H_{ij} \Psi_j = E\Psi_i , \qquad i \neq d \tag{3.75}$$

Now the component Ψ_d can be examined by using the latter equation when $j = d$;

84

$$H_{dd}\Psi_d + \sum_{j \neq d} H_{dj}\Psi_j = E\Psi_d \tag{3.76}$$

From equation (3.76) Ψ_d can be expressed as:

$$\Psi_d = \sum_{j \neq d} \frac{H_{dj}\Psi_j}{E - H_{dd}} \tag{3.77}$$

If equation (3.77) is substituted into equation (3.75) then:

$$\sum_{j \neq d} \left[H_{ij} + \frac{H_{id}H_{dj}}{E - H_{dd}} \right] \Psi_j = E\Psi_i \ , \quad i \neq d \tag{3.78}$$

This is an effective Schrödinger equation where the number of degrees of freedom is decreased by one compared to (3.74). Hence a new effective Hamiltonian ($\widetilde{H}$) can be introduced such as:

$$\widetilde{H}_{ij} = H_{ij} + \frac{H_{id}H_{dj}}{E - H_{dd}} \tag{3.79}$$

Produced by simple Gaussian elimination this Hamiltonian is the decimated Hamiltonian showing a notable feature of being energy dependent, which suits the method presented in the previous section very well [82]. The Hamiltonian describing the system in general would take the form without the decimation method:

$$H = \begin{pmatrix} H_L & V_L & 0 \\ V_L^\dagger & H_{scat} & V_R \\ 0 & V_R^\dagger & H_R \end{pmatrix} \tag{3.80}$$

Here, H_L and H_R denote the semi-infinite leads, H_{scatt} denotes the Hamiltonian of the scatterer and V_L and V_R are the coupling Hamiltonians, which couple the original scattering region to the leads. After decimation, we produce an effectively equivalent Hamiltonian:

$$H = \begin{pmatrix} H_L & V_c \\ V_c^\dagger & H_R \end{pmatrix} \tag{3.81}$$

V_c denotes an effective coupling Hamiltonian, which now describes the whole scattering process.

Similar to the one-dimensional case now the same steps can be applied; using the Dyson equation (equation (3.45)). Hence, the Green's function for the whole system is described by the surface Green's functions (equations (3.72) and (3.73)) and the effective coupling Hamiltonian from equation (3.81):

$$G = \begin{pmatrix} \mathscr{G}_L^{-1} & V_c \\ V_c^\dagger & \mathscr{G}_R^{-1} \end{pmatrix}^{-1} = \begin{pmatrix} G_{00} & G_{01} \\ G_{10} & G_{11} \end{pmatrix} \tag{3.82}$$

Scattering Matrix

We now proceed to the calculation of the scattering amplitudes. A generalization of the Fisher-Lee relation [86,88,95], assuming that states are normalized to carry unit flux, will give the transmission amplitude from the left lead to the right lead as:

$$\vec{t}_{hl} = \widetilde{\Phi}^{\dagger}_{(k_h)} G^{hl}_{RL} v^{hl}_L \Phi_{(k_l)} \sqrt{\left|\frac{v_h}{v_l}\right|} \tag{3.83}$$

In this case $\Phi_{(k_h)}$ is a right moving state vector in the right lead and $\Phi_{(k_l)}$ is a right moving state vector in the left lead. The corresponding group velocities are denoted v_h and v_l respectively. The reflection amplitudes in the left lead similarly reads:

$$\overleftarrow{r}_{hl} = \widetilde{\Phi}^{\dagger}_{(\bar{k}_h)} \left(G^{hl}_L v^{hl}_L - I \right) \Phi_{(k_l)} \sqrt{\left|\frac{v_h}{v_l}\right|} \tag{3.84}$$

Here $\Phi_{(\bar{k}_h)}$ is a left moving state vector in the left lead and $\Phi_{(k_l)}$ is a right moving state vector in the left lead. In both cases, v_{gL} is the v operator defined by equation (3.69) for the left lead.

Similarly we can define the scattering amplitudes for particles coming from the right:

$$\overleftarrow{t}_{hl} = \widetilde{\Phi}^{\dagger}_{(\bar{k}_h)} G^{hl}_{LR} v^{hl}_R \Phi_{(\bar{k}_l)} \sqrt{\left|\frac{v_h}{v_l}\right|} \tag{3.85}$$

$$\vec{r}_{hl} = \widetilde{\Phi}^{\dagger}_{(k_h)}\left(G_R^{hl}v_R^{hl} - I\right)\Phi_{(\bar{k}_l)}\sqrt{\left|\frac{v_h}{v_l}\right|} \qquad (3.86)$$

Here the definitions are identical, but for the obvious notation that what was left in the previous case is now right and vice versa.

So now a scattering matrix can be built and it is possible to calculate the conductance, using the Landauer formula (3.5) presented in section xx. H_1 and H_{scatt} is very general and since this method is valid for any choice of the Hamiltonians H_o.

Calculation in Practice

So far in this chapter the method presented is quite reasonable, and has been used in many areas of mesoscopic transport in the last decade. It has been successfully applied to molecular electronics [88,96,97], spintronics [88,98] and mesoscopic superconductivity [99-101]. For finite bias employing the non-equilibrium Green's function technique the same method has also been extended [102]. A Hamiltonian, which describes the system, can be created manually or can be an output of a numerical calculation, such as HF, DFT code or density functional tight-binding method.

3.5. Generic Features of the Transmission Coefficient

Before continuing, with the use of simple toy models, it would be useful to briefly study a few key features that might have been expected to see in the more complicated transport curves of real systems. For this, the decimation method described in equation

(3.75) has been used to reduce the discussed systems down to an effective Hamiltonian with the structure shown in figure 3.4. From there, it is simply a matter of using the Green's function (equation (3.47)) to calculate the transmission coefficient using equation (3.49) and then the transmission probability. Three features will be studied: Breit-Wigner Resonances [103], Fano Resonances [104,105] and antiresonances due to quantum interference [106,107].

Breit-Wigner Resonance

The simplest feature to understand is the Breit-Wigner resonance. This is a Lorentzian peak in the transmission probability which occurs when the energy of the incident wave resonates with an energy level within the scatterer. Figure 3.6 shows the simplest example of such a system. Two one-dimensional semi-infinite crystalline chains with site energies (ε_o) and hopping elements ($-\gamma$) are coupled to a scatting region with a single site energy (ε_1) by hopping elements ($-\alpha$).
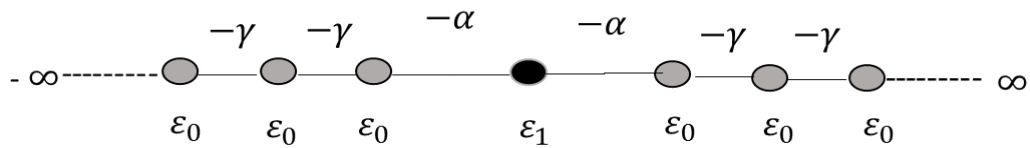
Figure 3.6: Simple model to study Fano resonance. Two one-dimensional semi-infinite crystalline chains coupled to a scatting region of site energy ε_1 by hopping elements $-\alpha$.

The red line in figure 3.9 shows the transmission probability for this system when $\varepsilon_o = \varepsilon_1 = 0$, $\gamma = 0.1$ and $\alpha = 0.01$. The width of the resonance is defined by the coupling component α and its location by the site energy ε_1. Typically, the scatterer has many

energy levels, but in a sufficiently weakly coupled system, they are easy to identify. Resonances corresponding to the HOMO and LUMO levels of the system are most notable because the Fermi energy, and therefore the conductance of the scatterer, is usually between these two peaks. In general, if the coupling element $(-\alpha)$ is large, the resonances are wider and the conductance is larger.

Fano Resonance

Fano resonances occurs when a continuum of states interacts with a bound state (the resonant process) and the two states interfere [108]. For example, when the energy (E) of the incident electron is close to an energy level of a side group of a molecule a Fano resonance appears. A toy-model approximation is shown in figure 3.7. Two one-dimensional semi-infinite crystalline chains with site energies (ε_o) and hopping elements $(-\gamma)$ are coupled to a scatting region with two site energies ε_1 (site one) and ε_2 (site two). Site one binds to the leads with hopping elements $(-\alpha)$. Site two, the side-group, is bound to site one by hopping element $(-\beta)$.
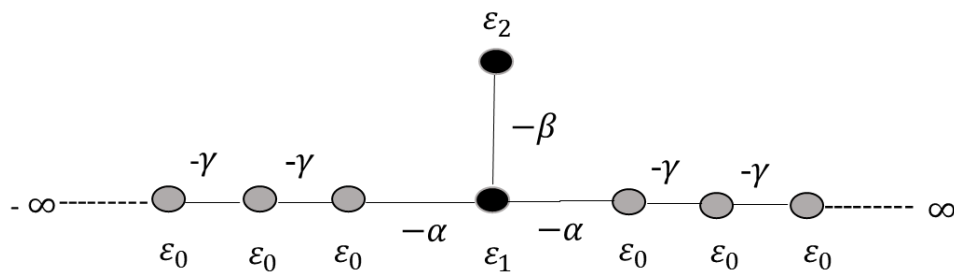
Figure 3.7: Simple model to study Fano resonances. Two one-dimensional semi-infinite crystalline chains coupled to a scatting region of site energy (ε_1) by hopping elements ($-\alpha$). An extra energy level (ε_2) is coupled to the scattering level by hopping element ($-\beta$).

In figure 3.9 the green curve shows the transmission probability for this system when $\varepsilon_1 = 0$, $\varepsilon_2 = 0.5$, $\gamma = 0.1$ and $\alpha = \beta = 0.01$. The shape of the curve closely resembles that of the Breit-Wigner curve (Figure 3.9, red), except that a Fano resonance occurs at $E \approx \varepsilon_2$.

Fano resonances have been shown to be tuneable via the molecular side groups [105] or gate voltages [109] and have been shown to give the molecules interesting thermoelectric properties [89,110].

Anti-Resonance

When the system is multibranched and destructive interference occurs between propagating waves at the nodal point an anti-resonance also appears in the transmission probability. In figure 3.8 a simple example is shown. Two one-dimensional semi-infinite crystalline chains with site energies (ε_o) and hopping elements ($-\gamma$) are coupled to two non-interacting scatting regions with site energies ε_1 (site one) and ε_1 (site two) by the hopping parameter ($-\alpha$).
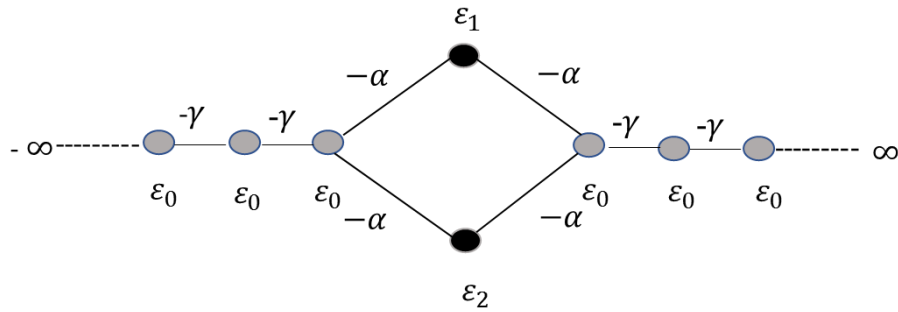
Figure 3.8: Simple model to study antiresonances. Two one-dimensional semi-infinite crystalline chains coupled to two independent scatting regions of site energies ε_1 and ε_2, by hopping elements ($-\alpha$).

When $\varepsilon_o = \varepsilon_1 = 0$, $\varepsilon_2 = -0.5$, $\gamma = 0.1$ and $\alpha = 0.01$ the blue curve in figure 3.9 shows the analytical transmission probability for this system. Corresponding to the site

energies of each scatterer as expected the curve shows two Breit-Wigner peaks at $E = 0$ and $E = 0.5$. Where the transmission probability drops to $T(E) \approx 0$ the antiresonance occurs between these points $E = 0.25$. This drastic change in electron transmission is utilised in quantum interference effect transistors (QuIET) [111], data storage [112] and molecular switches [113].
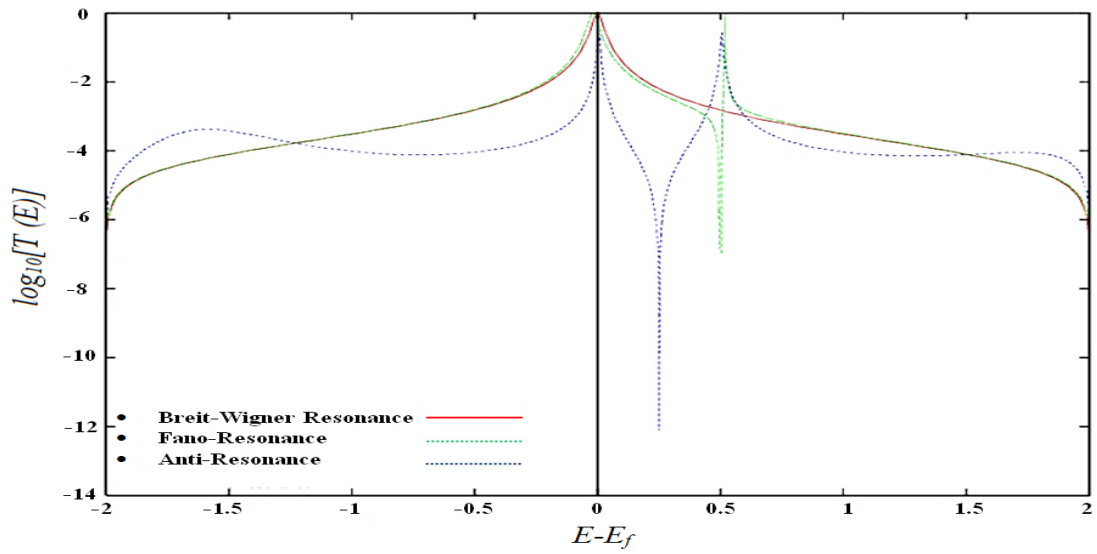
Figure 3.9: Transmission coefficients for the systems describe in sections Breit –Wigner (Red), Fano (Green) and Anti (Blue) Resonances.

Chapter 4

Transport through molecular junctions formed from monomers or chains of C_{50}, C_{60} or $C_{50}Cl_{10}$

4.1. Introduction

In this thesis, I address the possibility of using fullerenes and exohedral fullerenes as building blocks in molecular electronics devices. To examine this question I have looked at possibilities to enhance the electronic communication between the buckminsterfullerene and Decachlorofullerene. The methods used in this work are based on density functional theory followed by Green's functions quantum transport calculations.

C_{60} and C_{50} are the isomeric structure of carbon, whereas exohedral fullerene $C_{50}Cl_{10}$ is obtained when bonds are removed chemically by addition of Cl, to yield open cage fullerenes (see their optimized in figure 4.1).

In this chapter, I compute the transmission coefficient , transport properties, the thermopower of these structures. The work below is a systematic theoretical study of electron transport through molecular bridges attached via C_{50}, C_{60} and $C_{50}Cl_{10}$ anchor to flat gold electrodes. The C_{50}, C_{60} and $C_{50}Cl_{10}$ were oriented with a C-C bond between a hexagon and a pentagon facing the substrate.

The focus of this chapter is the comparison between the fullerene C_{60} and the exohedral-fullerene $C_{50}Cl_{10}$ which consists of a smaller fullerene C_{50} surrounding by 10 equatorial chlorines. In a molecular junction using gold lead as electrodes, direct bonding between the molecule and the could lead to clearly defined contact geometries and the stronger binding which will enhance conductance.

4.2. Computational Methods

To undertake a comparative study of their electronic properties, when placed between two gold electrodes, we used the density functional theory (DFT) code SIESTA [114] which employs Troullier-Martins pseudopotentials [115] to represent the potentials of the atomic cores, and a local atomic-orbital basis set. A double-zeta polarized basis set was used for all atoms and the generalized gradient approximation (GGA-PBE) for the exchange and correlation functionals [116,117]. The Hamiltonian and overlap matrices were calculated on a real-space grid defined by a plane-wave cut-off of 250 Ry. Each molecule was relaxed to the optimum geometry until the forces on the atoms were smaller than 0.02 eV/Å and in case of the isolated molecules, a sufficiently-large unit cell was used.

4.3. DFT Calculation and Numerical Simulation

Optimized geometries and Binding Energy

The ground state energy of the total system is calculated using SIESTA and is denoted E_{AB}^{AB}, The energy of each monomer is then calculated in a fixed basis, which is achieved by the use of ghost atoms in SIESTA. Hence the energy of the individual

buckminsterfullerene in the presence of the fixed basis is defined as E_A^{AB} and another one is E_B^{AB}.

The binding energy is then calculated using the following equation:

$$\text{Binding Energy} = E_{AB}^{AB} - E_A^{AB} - E_B^{AB} \tag{4.1}$$
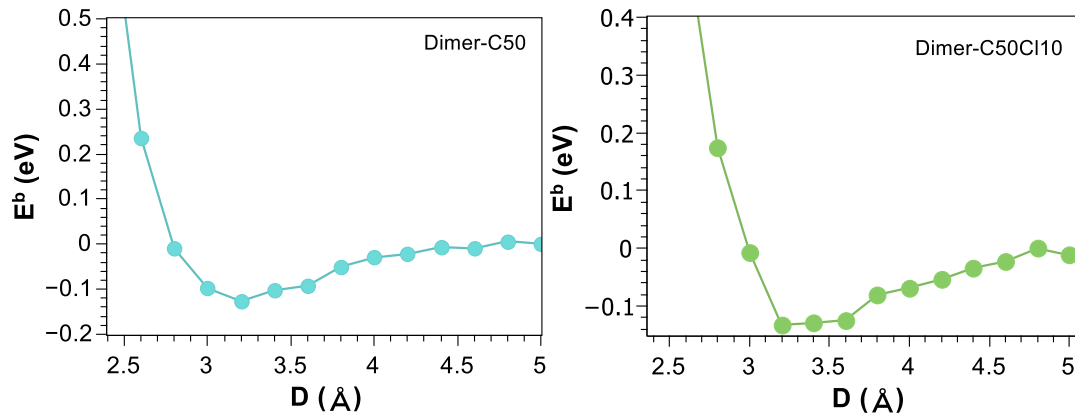
Figure 4.2 DFT calculation of the binding energy as a function of distance between two C50, C50Cl10.

For the dimers, I varied the distance between two molecules from 1.2 to 5 Å and computed their binding energy as a function of distance. As shown in figure 4.2, for a C_{60} dimer, the optimum separation of the C_{60}s is 3.5 Å and the binding energy is (~-0.05 eV), while for the C_{50} and $C_{50}Cl_{10}$ dimer, the optimum separation is 3.2 Å and the binding energy is (~-0.03 eV).

Transmission Coefficient.

As previously described, the Green's function formalism is used to calculate the single electron transport properties and to do this I use the transport package Gollum, which

is based upon equilibrium transport theory. It calculates the transmission coefficients T(E) for electrons of energy E and the temperature dependence to calculate thermoelectric properties uses the Fermi distribution function defined as

$$f(E, T) = [e^{(E-E_F)/k_B T} + 1]^{-1} \qquad (4.2)$$

where k_B is the Boltzmann constant.

For the DFT calculations presented in this Chapter, I have used a Generalised Gradient Approximation (GGA) with a double zeta polarized basis set and an energy cutoff of 250 Ry to define the real space grid. During all my calculations the fullerenes and exohedral fullerenes between the electrodes were relaxed with a 0.02 eV/Å force tolerance. The electrodes were fixed in their relaxed configuration to obtain more systematic results and to facilitate the effect of the different bonding sites of the molecule to the gold surface without having to use excessively large lead surfaces in periodic boundary conditions in one direction.

To investigate the stability of the transport properties against a movement of fullerenes and exohedral fullerenes out of the equilibrium C_{50}, C_{60} or $C_{50}Cl_{10}$ electrode separation conductance curves were obtained to find the relaxed molecule to lead separation of r = 2.2 Å for monomers placed between two gold <111> electrodes, as shown in Figures 4.6.
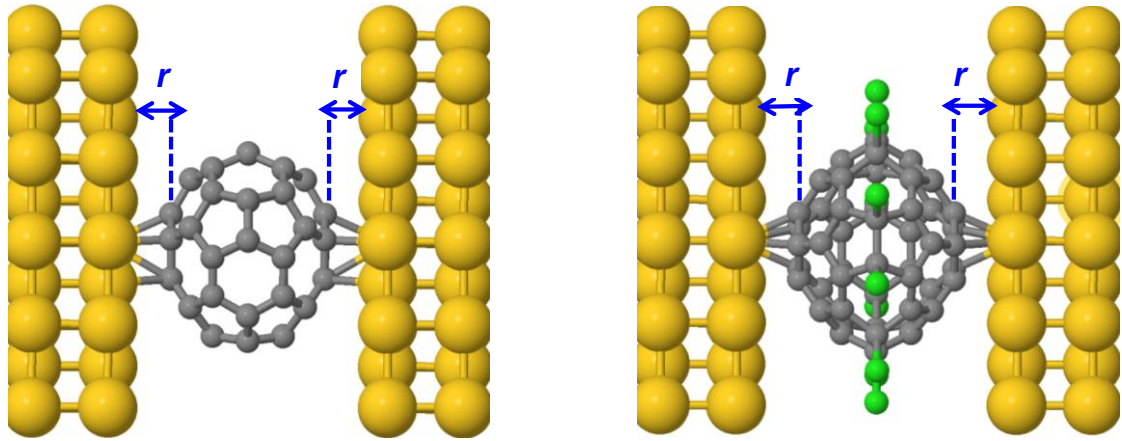
Figure 4.6 : *The C_{50}, C_{60} ^{a}nd $C_{50}Cl_{10}$ were oriented with a C-C bond between a hexagon and a pentagon facing the substrate with respect to the flat gold leads. A single C_{50}, C_{60} or $C_{50}Cl_{10}$ attached to Au <111> surfaced electrodes, r=2.2 Å and is fixed with periodic boundary conditions PBC applied in all three direction.*

To investigate the dependence of the conductance on the orientation of monomers, dimers and trimers, the Hamiltonian of the system was obtained from the DFT calculations and passed onto to Gollum for the transport calculations.

The zero basis transmission curves for dimer and trimer C_{50}, C_{60} and $C_{50}Cl_{10}$ molecules at the equilibrium dimer and trimer distances are plotted on Figure 4.7, 4.9, 4.12 and 4.14.

To investigate the effects of the separation d between buckyballs upon the tranport, I have plotted the transmission curves as a function of $E-E_F$ for various seperations between the C_{50}, C_{60} or $C_{50}Cl_{10}$ dimers and trimers, for each geometrical configuration. Results are shown in figures 4.8, 4.10, 4.11, 4.13, 4.15 and 4.16.
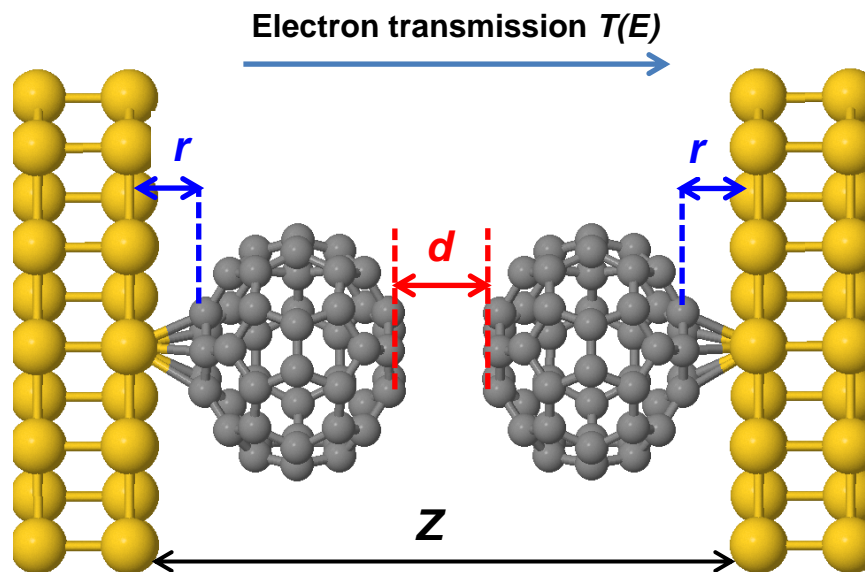
Figure 4.7: *A geometry for C50-bare (dimers). Red arrows indicate moving variables, whereas blue arrows indicate fixed distances. Z is the electrode separation, r=2.2 Å and is fixed, d is varied from (1.6 -5.0) Å.*
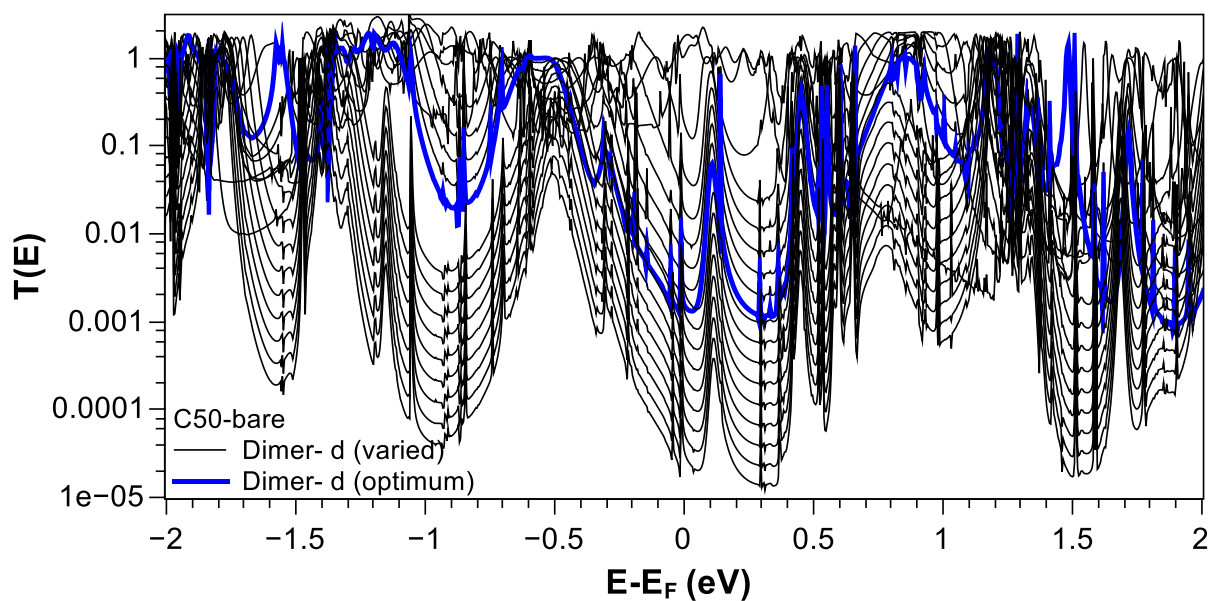
Figure 4.8: *DFT caculations of transmission coeffecients as a function of energy T(E) for varied configuration of dimer C50-bare (black) and (blue) for optimum configuration. r=2.2 Å and is fixed, d is varied from (1.6 -5.0) Å.*
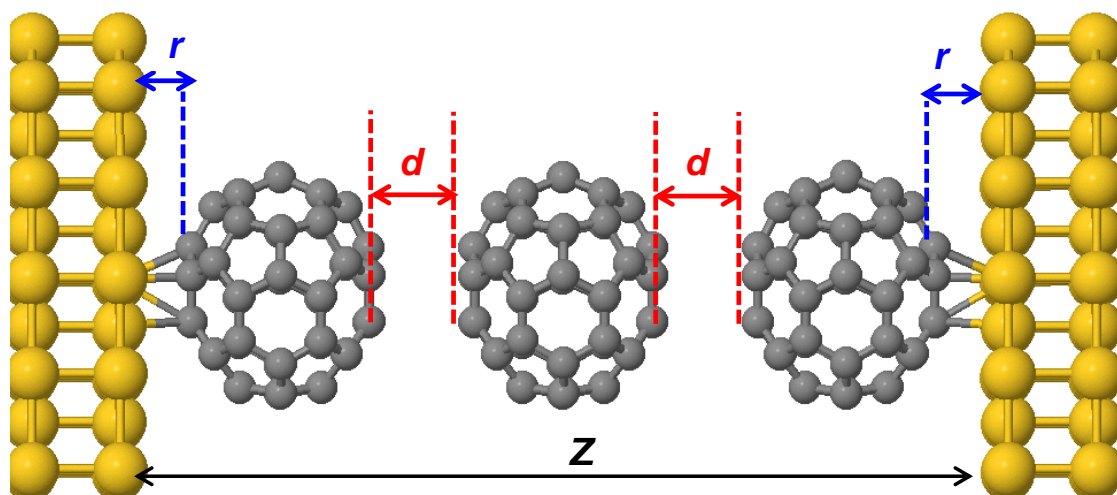
Figure 4.9: *A geometry for C50-bare (Trimers). Red arrows indicate moving variables, whereas blue arrows indicate fixed distances. Z is the electrode separation, r=2.2 Å and is fixed, d is varied from (1.6 -5.0) Å.*
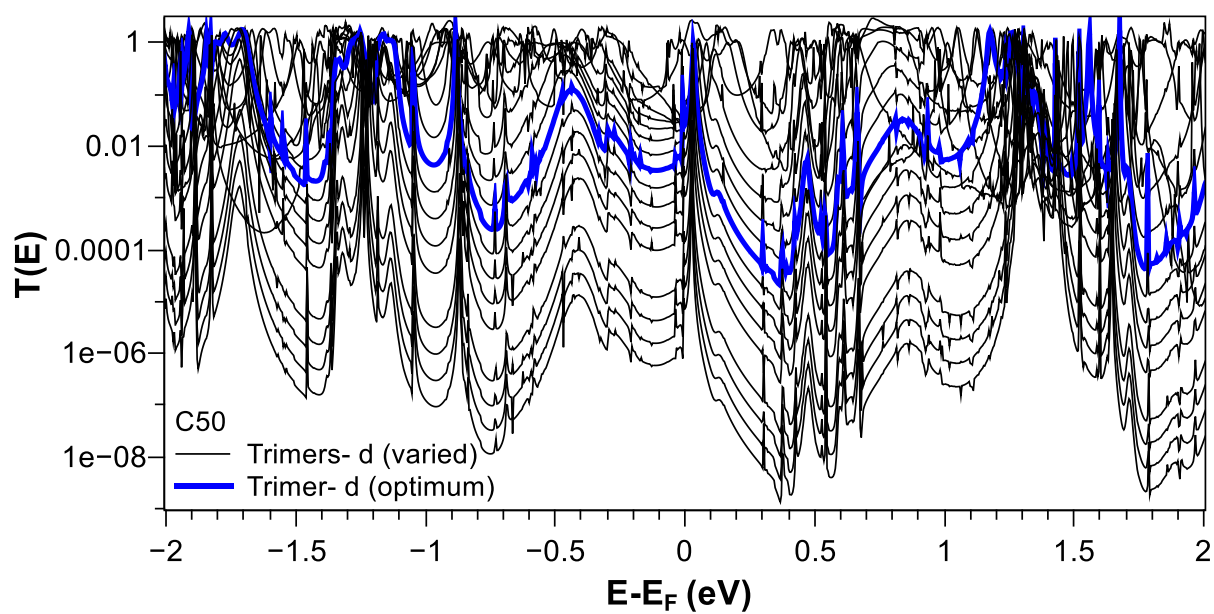
Figure 4.10: *DFT caculations of transmission coeffecients as a function of energy T(E) for varied configuration of trimer C_{50}-bare (black) and (blue) for optimum configuration. r=2.2 Å and is fixed, d is varied from (1.6 -5.0) Å.*
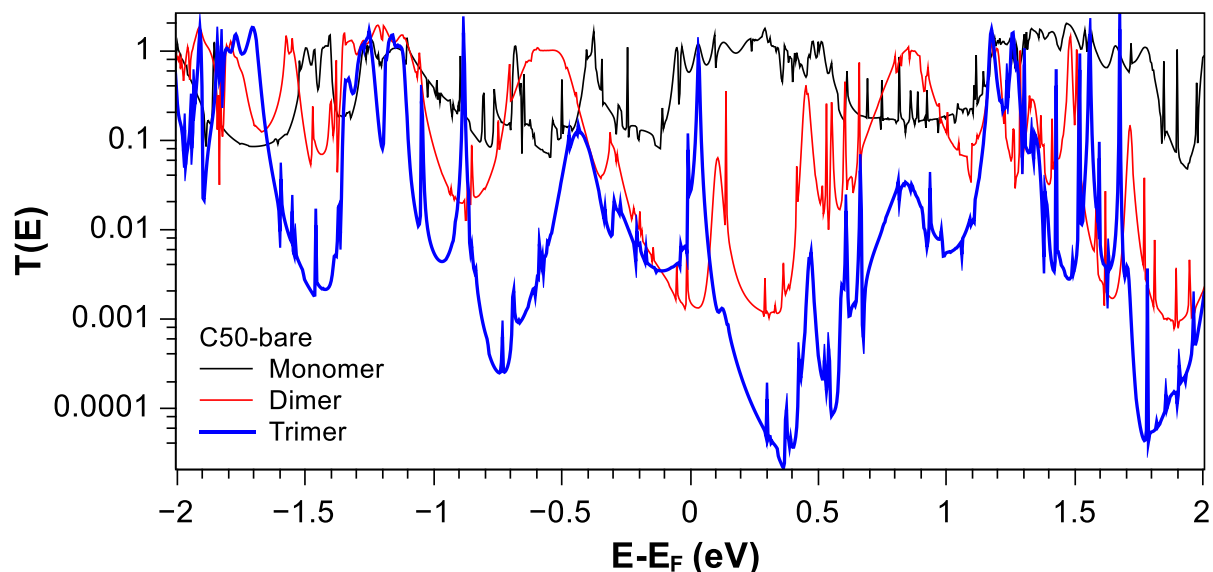
Figure 4.11: *DFT caculations of transmission coeffecients as a function of energy T(E) for single C50-bare (black dots), the optimum configuration of C50 dimer (red dots) and C50 trimer (blue line). r=2.2 Å and is fixed, d is varied from (1.6 -5.0) Å.*

The curves corresponding to the optimum geometries are summarised in Figure 4.11 for the monomer, dimer and trimer C_{50}. To interpret the curves I will refer to the positions of the transmission peaks relative to $(E-E_F) = 0.0$ eV. The highest occupied molecular orbital (HOMO) levels are below the Fermi energy and the lowest unoccupied molecular orbital (LUMO) levels are above the Fermi energy. Since these define the relevant energies for transport, I will concentrate only on the peaks located close to $(E-E_F) = 0.0$ eV.

Fig. 4.11 shows that for bare C_{50} the monomer has at least a two-orders of magnitude higher transmission coefficient at the Fermi energy than the dimer and trimer. Furthermore, the LUMO resonance is rather broad and the transmission near the Fermi energy is close to unity. For the dimer and trimer, LUMO peaks in their transmission curves are located between 0.1 and 0.2 eV for the dimer (red curve and arrow) and the

trimer (blue curve and arrow). Furthermore the peaks are stable i.e. do not shift over many configurations as show in Figures 4.8 and 4.10. One might have expected that the transmission of the trimer at $(E-E_F) = 0.0$ eV would be lower than that of the dimer, but the since the LUMO resonance moves closer to $(E-E_F) = 0.0$ eV this is not the case.

These results are now compared to those for the case of $C_{50}Cl_{10}$ monomer, dimer and trimer in figures 4.12, 4.13 , 4.14 and 4.15. The optimumised results are shown in Figure 4.16.
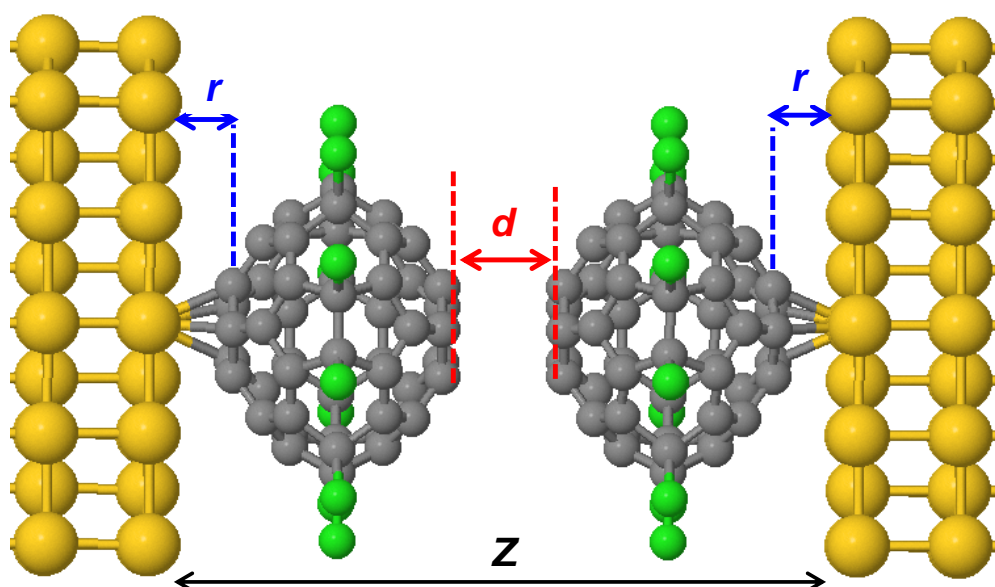
Figure 4.12: *A geometry for $C_{50}Cl_{10}$ (Dimers). Red arrows indicate moving variables, whereas blue arrows indicate fixed distances. Z is the electrode separation, r=2.2 Å and is fixed, d is varied from (1.6 -5.0) Å.*
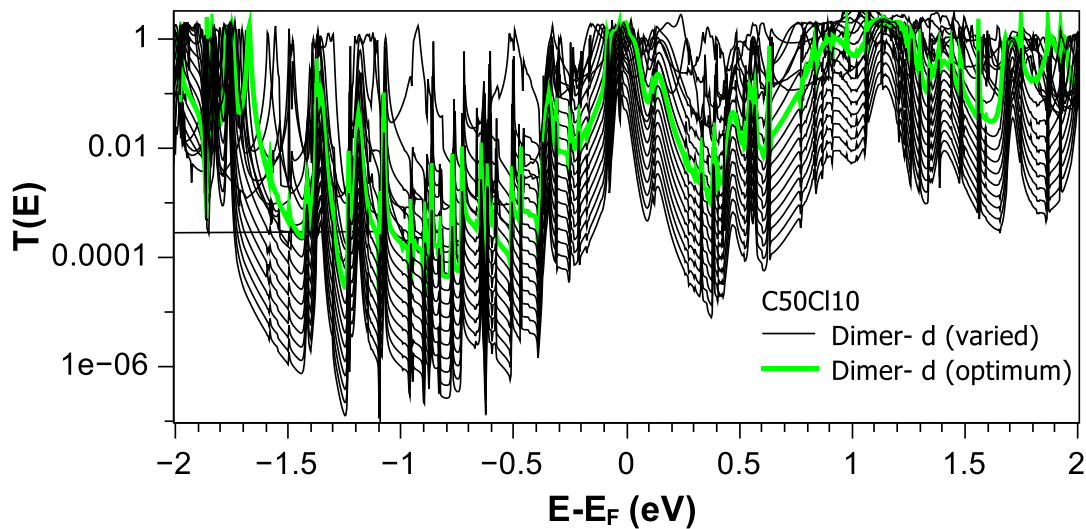
Figure 4.13: *DFT caculations of transmission coeffecients as a function of energy T(E) for varied configuration of dimer $C_{50}Cl_{10}$ (black) and (green) for optimum configuration.*
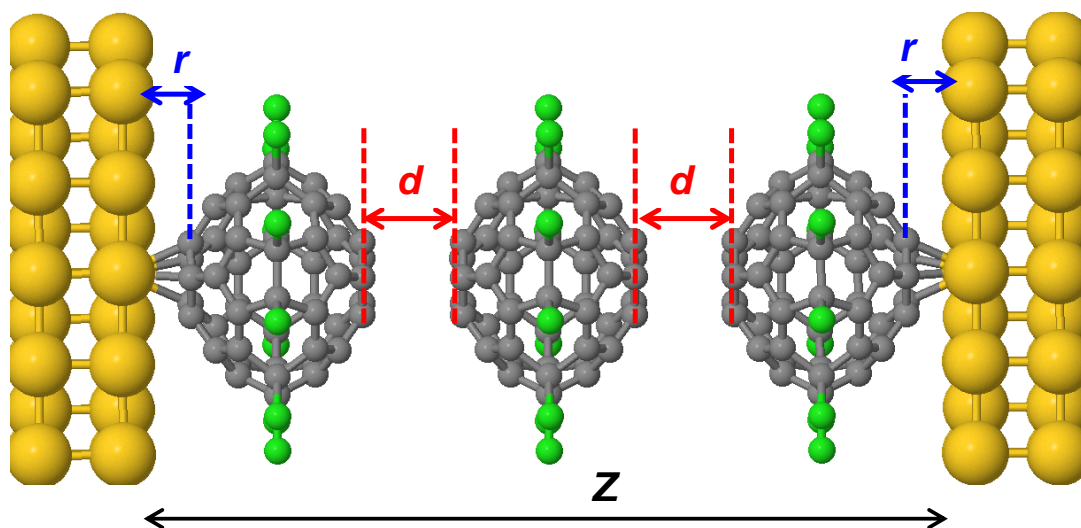
Figure 4.14: *A geometry for $C_{50}Cl_{10}$ (trimer). Red arrows indicate moving variables, whereas blue arrows indicate fixed distances. Z is the electrode separation, r=2.2 Å and is fixed, d is varied from (1.6 -5.0) Å.*
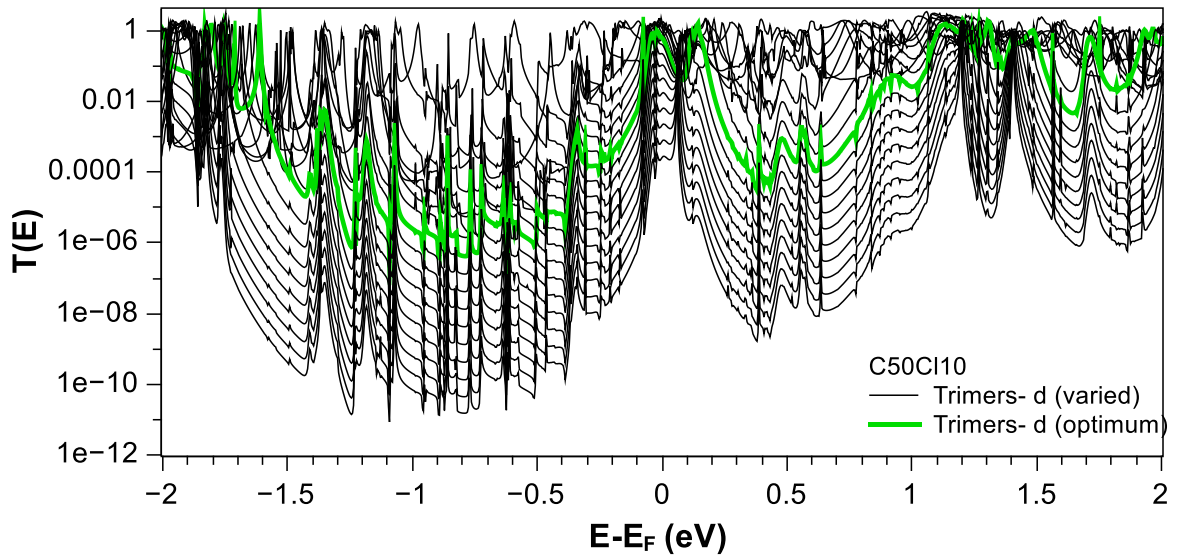
Figure 4.15: *DFT caculations of transmission coeffecients as a function of energy T(E) for varied configuration of trimer $C_{50}Cl_{10}$ (black) and (green) for optimum configuration.*
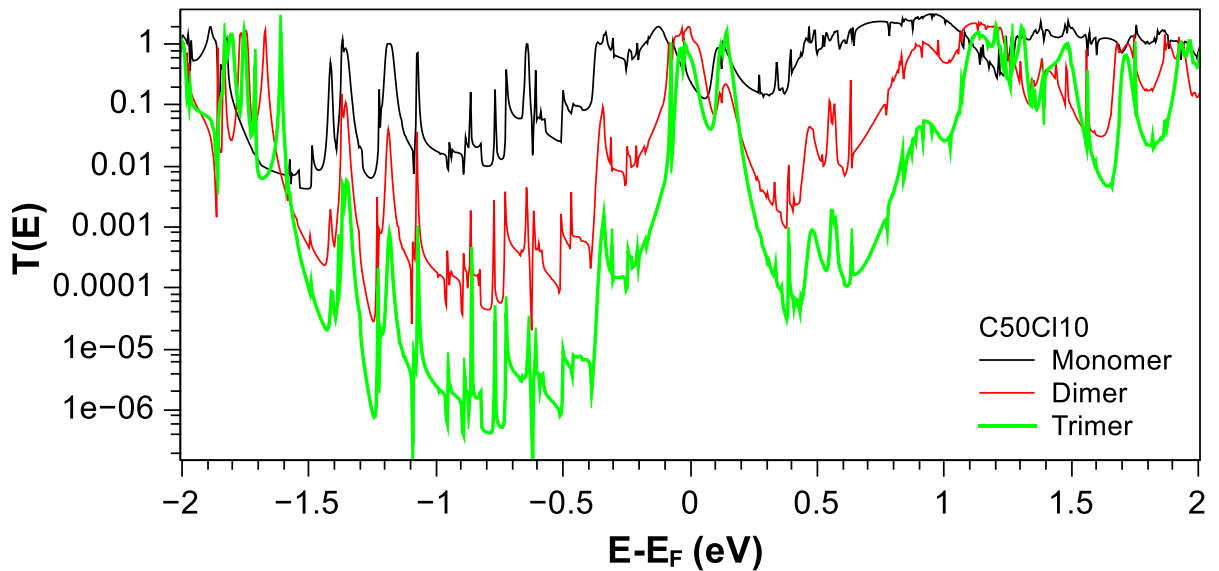
Figure 4.16: *Below the caculation of T(E) for single C50Cl10 (black dots), the optimum configuration of C50Cl10 dimer (red dots) and C50Cl10 trimer (green line).*

Here the general trend is that at energies that do not coincide with the transmission resonance at the Fermi energy, T(E) decreases as the number of units increases. However in contrast with bare C_{50}, the resonance peaks for the dimer and trimer are located around the Fermi energy (E-E$_F$) = 0.0 eV. The peaks are again stable i.e. do not shift over many different configurations as shown in Figures 4.13 and 4.15. In the

$C_{50}Cl_{10}$ molecule the energy levels are almost degenerate due to the overlap of the Chlorine and Carbon levels resulting in the possibility of high conductance as the number of units increases.

Figure 4.17 summarises the above results and includes the case of the tetramer to further illustrtae the trends with increasing number of fullerenes.
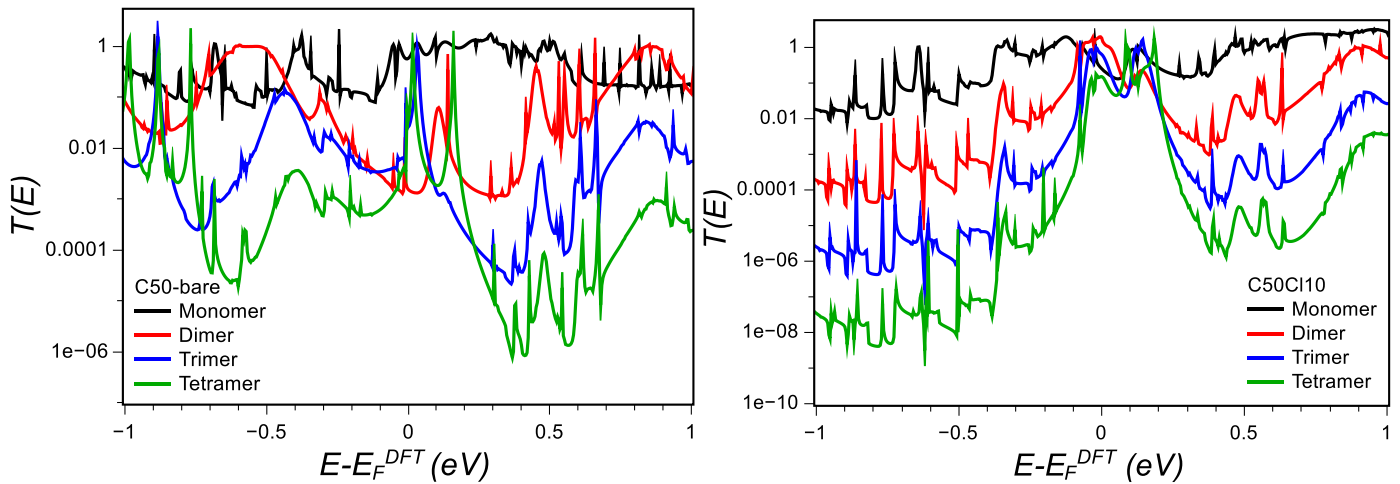
Figure 4.17 *(Up) DFT caculations of transmission coeffecients as a function of energy T(E) for single C50-bare (black dots), C50 dimer (red dots) and C50 trimer (blue line). Below the caculation of T(E) for single C50Cl10 (black dots), C50Cl10 dimer (red dots) and C50Cl10 trimer (green line).*

For comparison, I have calculated the the zero bias transmission for the monomer, dimer and trimer for the case of the buckminster fullerene C_{60} in figures 4.18and 4.19 the transmission curves as a function of the seperation between the C_{60} for each geometrical configuration where a geometry for C_{60} dimer and trimer. The distance between C_{60} and electrodes r =2.2 Å is fixed, d is varied between 1.6 and 5.0 Å. Again we see that bthere is a braod LUMO resonance near the Fermi energy.
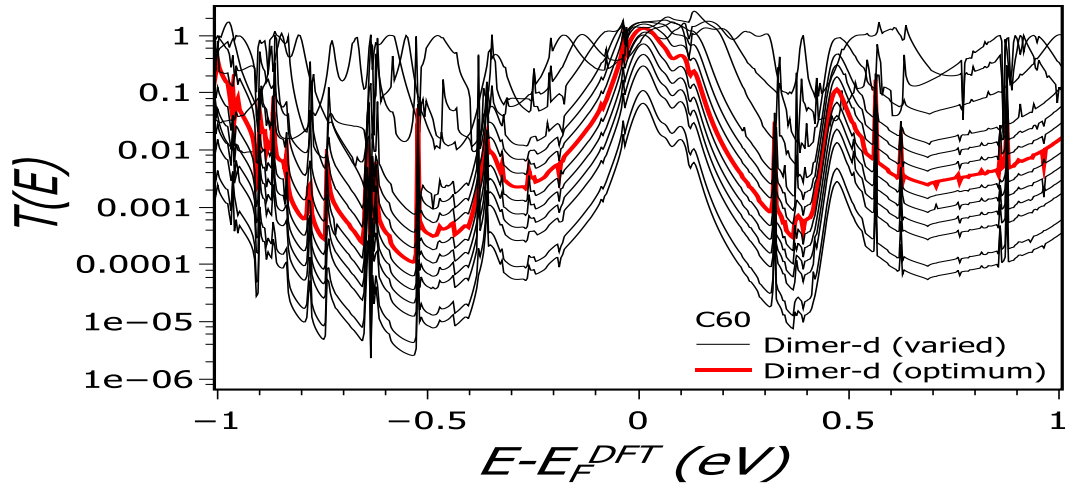
Figure 4.18: *DFT caculations of transmission coeffecients as a function of energy T(E) for varied configuration of dimer C_{60} (black) and (red) for optimum configuration.*
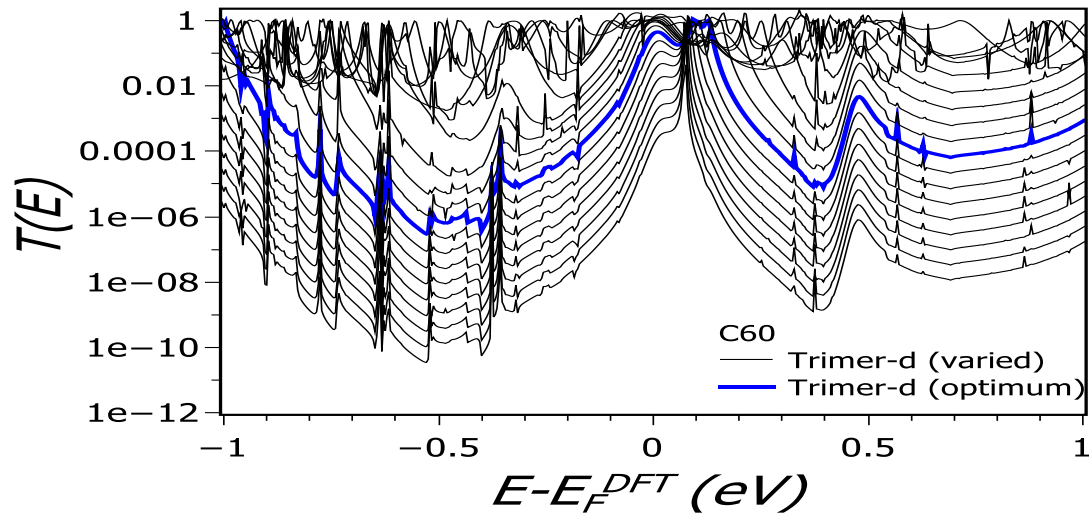
Figure 4.19: *DFT caculations of transmission coeffecients as a function of energy T(E) for varied configuration of trimer C_{60} (black) and (blue) for optimum configuration.*

4.4. Summary

I addressed the question of using fullerenes and exohedral fullerenes as possible building blocks in molecular electronics devices. Experimentally buckyballs were already suggested as potential high stability anchor by Martin et al. [119].

The $C_{50}Cl_{10}$ should have distinct properties to those of other fullerenes. The exohedral fullerene $C_{50}Cl_{10}$ provides slightly charged in $C_{50}Cl_{10}$ to that C_{50} and $C_{50}Cl_{10}$ is an insulator. Furthermore, the fan of ten chlorine atoms stabilise the C_{50} and HOMO – LUMO energy gap of $C_{50} \approx C_{60}$.

In all cases the transport is dominated by the LUMO resonances. The conductance of the monomer is approximately G_0, while that of the bare C_{50} dimers and trimers is substantially lower. . On the other hand, due to the presence of LUMO resonances near the Fermi energy, the conductances of C_{60} or $C_{50}Cl_{10}$ dimers and trimers are predicted to be significantly higher than those of bare C_{50}. It is worth noting that C_{60} and $C_{50}Cl_{10}$ are stable fullerenes, but the bare C_{50} is an unstable fullerene and can only be studied theoretically.

Having discussed their electrical conductance, in the next chapter, the thermopower of the above junction will be studied, which provides information about slope of the transmission function near the Fermi energy.

Chapter 5

Thermoelectric Properties of C_{60} and $C_{50}Cl_{10}$

Motivation

During the past few years, several groups have explored the thermoelectric properties of single-molecules placed between nanogap electrodes, driven both by a desire to understand fundamental thermoelectric effects at the nanoscale and by an expectation that knowledge of thermoelectricity at the single-molecule level will underpin the design of new high-performance thin-film materials.

The recent joint theory/experimental papers "Engineering the thermopower of C_{60} molecular junctions," Nano Lett., vol. 13, no. 5, pp 2141-2145, (2013), "Molecular design and control of fullerene-based bi-thermoelectric materials," Nature Mater. 15, 289–293 (2016) and my recent theory paper "Identification of a positive- Seebeck-Coefficient exohedral fullerene," NanoScale., vol. 8, no. 28, pp 13597-602, (2016) demonstrate that fullerenes exhibit surprising thermoelectrical effects, which can be controlled by mechanical manipulation. However for these effects to be utilised in practical devices, fullerenes exhibiting a positive Seebck coefficient are needed. My study below reveals that this obstacle is overcome by exohedral fullerenes, which provide a new class of materials, with thermoelectric properties which complement those of endohedral and all-carbon fullerenes.

5.1. Introduction

Tuning the thermoelectric properties of single molecules is of great interest, because they are potential building blocks for new materials with enhanced electrical and thermal functionality. When a single molecule is connected across a nano gap between two electrodes, whose temperatures differ by an amount ΔT, the resulting voltage difference $\Delta V = -S\,\Delta T$ is determined by the Seebeck coefficient (S) of the junction. This molecular-scale Seebeck effect has stimulated a recent outpouring of fundamental research aimed at controlling and increasing the efficiency of the effect using combinations of mechanical, electrostatic, chemical and electrochemical gating [120-142].

As an example of such control, recent scanning tunnelling microscope (STM) experiments [129] measured the conductance and thermopower of C_{60} molecules and found that compared with a single C_{60}, the Seebeck coefficient could be almost doubled by placing C_{60}s in series to form dimers. These experiments suggest that thin molecular films of fullerenes may be excellent thermoelectric materials. However to build a usable all-fullerene device, it will necessary to boost the thermovoltage in a tandem arrangement, by placing materials with Seebeck coefficients of opposite signs in series. Since C_{60} is found to have a negative Seebeck coefficient, in the present paper I address the challenge of identifying a fullerene with a positive Seebeck coefficient. Recent experiments on the endohedral fullerene [132] $Sc_3N@C_{80}$ demonstrated that the Seebeck coefficient of this material could be either positive or negative, depending on the applied pressure. Although this compound does not meet my challenge, because the sign of the Seebeck coefficient is variable, it does suggest that chemical modification

may solve the problem of identifying positive-Seebeck-coefficient fullerenes. Therefore in the present chapter I examine for the first time the possibility of controlling thermoelectricity in exohedral fullerenes. In particular, I study the exohedral decachlorofullerene $C_{50}Cl_{10}$, which is chemically stable and was first fabricated in milligram quantities in 2004 [143,144]. My aim is to explore the potential for thermoelectricity of molecular junctions formed from one or two decachlorofullerenes attached to gold electrodes and to determine if their properties can be controlled by mechanical gating.

To compute the thermoelectric properties of such junctions, I note that in the linear-response regime, the electric current I and heat current $\dot{Q}$ passing through a device is related to the voltage difference ΔV and temperature difference ΔT by [120]:

$$\begin{pmatrix} I \\ \dot{Q} \end{pmatrix} = \frac{2}{h} \begin{pmatrix} e^2 L_0 & \frac{e}{T} L_1 \\ e L_1 & \frac{1}{T} L_2 \end{pmatrix} \begin{pmatrix} \Delta V \\ \Delta T \end{pmatrix} \tag{5.1}$$

where T is the reference temperature and

$$L_n = \int_{-\infty}^{\infty} (E - E_F)^n \, T(E) \left(-\frac{\partial f(E,T)}{\partial E} \right) dE \tag{5.2}$$

In this expression e=-|e| is the electronic charge, $T(E)$ is the transmission coefficient for electrons of energy E, passing through the molecule from one electrode to the other and $f(E,T)$ is Fermi distribution defined as $f(E,T) = [e^{(E-E_F)/k_B T} + 1]^{-1}$ where k_B is Boltzmann's constant.

When $\Delta T = 0$, equation (5.1) yields for the electrical conductance $G = \left(\frac{I}{\Delta V} \right)_{\Delta T = 0}$,

$$G = \frac{2e^2}{h} L_0 \qquad (5.3)$$

Similarly when $I = 0$, equation (5.1) yields for the Seebeck coefficient $S = -(\frac{\Delta V}{\Delta T})_{I=0}$,

$$S = \frac{-1}{|e|T} \frac{L_1}{L_0} \qquad (5.4)$$

whereas the Peltier coefficient (Π), and the electronic contribution to the thermal conductance (κ_e) are given by

$$\Pi = \frac{-1}{|e|} \frac{L_1}{L_0} \qquad (5.5)$$

$$\kappa_e = \frac{2}{hT} \left(L_2 - \frac{(L_1)^2}{L_0} \right) \qquad (5.6)$$

From the above expressions, the electronic thermoelectric figure $ZT_e = S^2 GT/\kappa_e$ is given by

$$ZT_e = \frac{(L_1)^2}{L_0 L_2 - (L_1)^2} \qquad (5.7)$$

For E close to E_F, if $T(E)$ varies only slowly with E on the scale of $k_B T$ then these formulae take the form [120,121]

$$G(T) \approx \left(\frac{2e^2}{h} \right) T(E_F), \qquad (5.8)$$

$$S(T) \approx -\alpha |e| T \left(\frac{d \ln T(E)}{dE} \right)_{E=E_F}, \qquad (5.9)$$

$$\kappa_e \approx \alpha T G, \qquad (5.10)$$

where $\alpha = \left(\frac{k_B}{e}\right)^2 \frac{\pi^2}{3} = 2.44.10^{-8}$ WΩK^{-2} is the Lorentz number. Equation (5.9) demonstrates that S is enhanced by increasing the slope of ln $T(E)$ near $E=E_F$.

To compute their thermoelectric properties, when placed between two gold electrodes, I used the density functional theory (DFT) code SIESTA [145] which employs Troullier-Martins pseudopotentials [146] to represent the potentials of the atomic cores, and a local atomic-orbital basis set. A double-zeta polarized basis set was used for all atoms and the generalized gradient approximation (GGA-PBE) for the exchange and correlation functionals [147,148]. The Hamiltonian and overlap matrices were calculated on a real-space grid defined by a plane-wave cut-off of 250 Ry. Each molecule was relaxed to the optimum geometry until the forces on the atoms were smaller than 0.02 eV/Å and in case of the isolated molecules, a sufficiently-large unit cell was used.

5.2. Results and Discussion

For the dimers, I varied the distance between two molecules from 1.6 to 5 Å and computed their binding energy as a function of distance. As shown in figure 2, for a C_{60} dimer, the optimum separation of the C_{60}s is 3.5 Å and the binding energy is (~-0.05 eV), while for the $C_{50}Cl_{10}$ dimer, the optimum $C_{50}Cl_{10}$ separation is 3.2 Å and the binding energy is (~-0.03 eV).
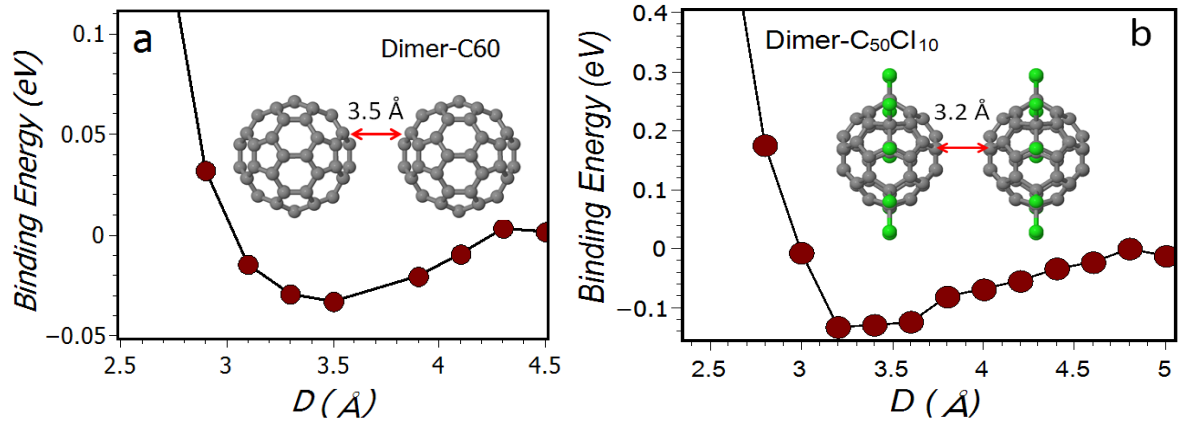
Figure 5.1. *DFT calculation of the binding energy as a function of distance between (Left) two C60 and (Right) two C50Cl10. The inset figures show the optimum structure for the dimer.*

Next, each relaxed molecule or dimer was placed between two gold <111> electrodes, as shown in Figures 3a and 3b. After geometry relaxation, the distance between each molecule and the gold electrode was found to be 2.2 Å. Figure 5.1, show optimum configurations of single and dimer C_{60} junctions, in which the distance between two C_{60}s is d =3.5 Å and the distance between the C_{60}s and electrodes is r=2.2 Å. To compute their thermoelectric properties, I used the quantum transport code Gollum [149], which combines the Hamiltonian provided by the DFT code SIESTA with a Green's function scattering formalism. Figure 5.2 shows the transmission coefficient *T(E)* as a function of energy *E* for the junctions in Figures 5.2a and 5.2b.
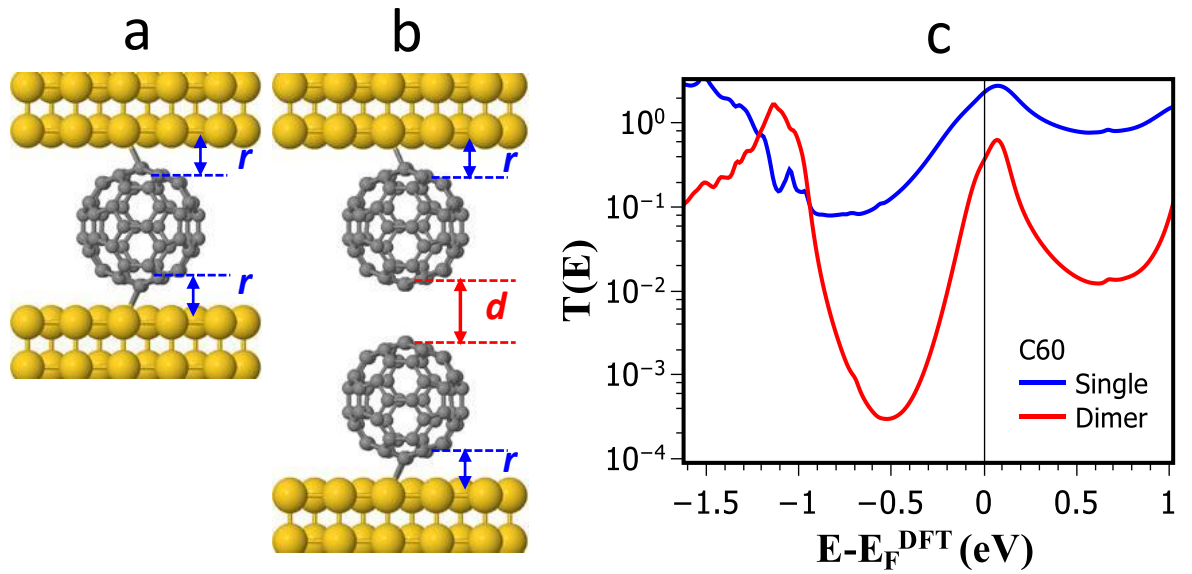
Figure 5.2. *Left panel shows an example of an optimized junction configuration for the systems containing (a) single C60 and (b) a C60 dimer placed between two gold electrodes. Right panel, (c) shows a DFT calculation of their transmission coefficients T(E) as a function of energy E relative to the DFT-predicted Fermi energy E_F^{DFT}.*

For both the monomer and the dimer, in agreement with ref [129], electrons near the Fermi energy transmit through the tail of the LUMO. Furthermore the dimer transmission (red line) is much smaller than that of the monomer, due to the increase in length of the molecular bridge, leading to a higher slope at the Fermi energy and a higher thermopower for the dimer.

Figure 5.3a and 5.3b show the corresponding $C_{50}Cl_{10}$ junctions, whose optimum dimer separation is d=3.2 Å and optimum distance between the $C_{50}Cl_{10}$s and electrodes is r=2.2 Å. Figure 5.3c shows the transmission coefficient *T(E)* of the monomer (blue) and dimer (red) and as expected the transmission of the dimer is lower than that of the monomer. Figure 5 shows a comparison between the transmission coefficients and corresponding

room-temperature electrical conductances of the $C_{50}Cl_{10}$ and C_{60} monomers and dimers, while Figures 5.6a-5.6d show the comparison between their room-temperature Seebeck coefficients (thermopower) S and power factors (σS^2).
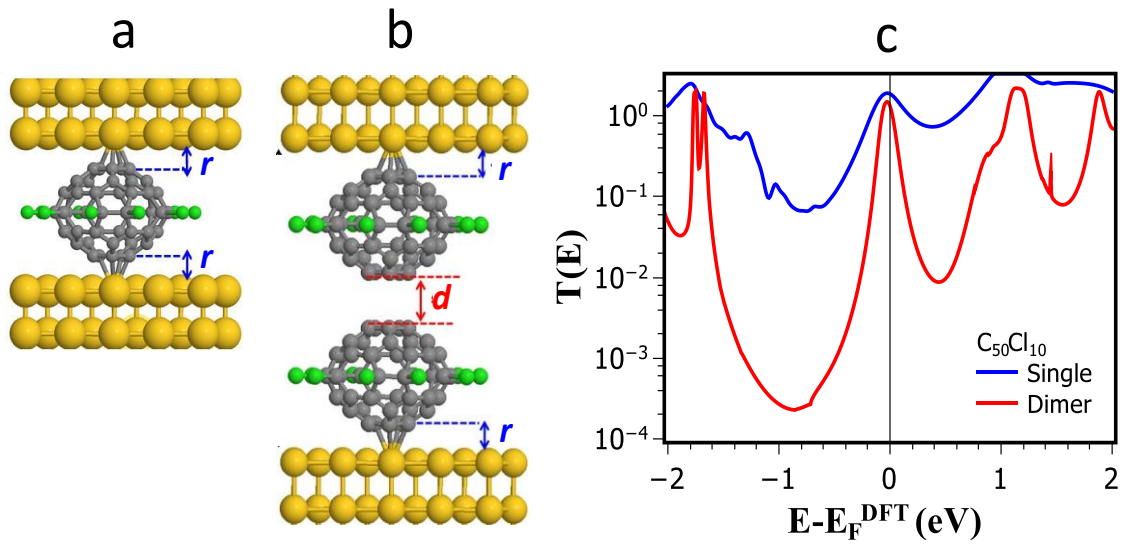
Figure 5.3. *Left panel shows an example of an optimized junction configuration for the systems containing (a) single and (b) dimer fullerene-$C_{50}Cl_{10}$ placed between two gold electrodes. Right panel, (c) shows DFT calculation of transmission coefficient as a function of energy for the structures in Figures 4a and 4b.*

Figure 5.6. *The left column, Figures (a and c) show the room-temperature Seebeck coefficient (thermopower S) and power factor (σS^2) over a range of Fermi energies E_F relative to the DFT-predicted Fermi energy E_F^{DFT} for the monomers in Figures 3a and 4a. The right column, (Figs b and d) shows the room-temperature Seebeck coefficient and power factor (σS^2) for the dimers in Figures 3b and 4b.*

The optimum separation of d= 3.2 Å for the $C_{50}Cl_{10}$ dimer and d= 3.5 Å for the C_{60} dimer is chosen for illustrative purposes. In the STM experiment of ref [129], in which the conductance and Seebeck coefficient of a C_{60} dimer was measured, one C_{60} molecule was located on the gold substrate and the other was attached to the STM tip. The distance between them was then varied by varying the position of the STM tip and many hundreds of curves of conductance and Seebeck coefficient versus d were obtained. These curves all differ, because the tip shape, the motion of the tip and the orientations of the molecules vary from measurement to measurement. Since these details are not known, this variation cannot be calculated. Nevertheless as an indication of how transport properties depend on the dimer separation d, figure 5.4 shows transmission curves for various values of d.

It is well-known [120] that DFT can give an inaccurate value for the Fermi energy and therefore Figures 5.6a-5.6c show results for a range of Fermi energies E_F relative to the DFT-predicted Fermi energy E_F^{DFT}. Figure 5.6a demonstrates that both the magnitude and sign of Seebeck coefficient S is changed by replacing the C_{60} with $C_{50}Cl_{10}$. For example at the DFT-predicted Fermi energy E_F^{DFT}, the Seebeck coefficient of single C_{60} is -21 µV/K and for C_{60} dimer, it increases to -56 µV/K. On the other hand the Seebeck coefficient of the single $C_{50}Cl_{10}$ is +8 µV/K and while for $C_{50}Cl_{10}$ dimer, it increases to +30 µV/K.

For a bulk material, the power factor P is defined by as $P = S^2\sigma$, where σ is the electrical conductivity. The notion of conductivity is not applicable to transport through single molecules, but to compare with literature values for bulk materials, I define $\sigma = GL/A$, where L and A are equal to the length and the cross-sectional area of the molecule respectively. In what follows, for single (dimer) C_{60} the values L=1.13 (2.12) nm and A=2.1 nm^2 are used, whereas for single (dimer) $C_{50}Cl_{10}$ I assign values L=1 (1.85) nm and A=2.1 nm^2. From the results of Figure 5.6a and 5.6b, the temperature dependence of the power factors $P = S^2GL/A$ computed using the DFT-predicted Fermi energy are shown in Figure 7c and 7d. These results show that C_{60} monomer and dimer have room-temperature factors of 8.8×10^{-5} W/m.K^2 and 6.3×10^{-5} W/m.K^2 respectively, whereas the $C_{50}Cl_{10}$ monomer and dimer have power factors of 0.5×10^{-5} W/m.K^2 and 6.0×10^{-5} W/m.K^2 respectively.
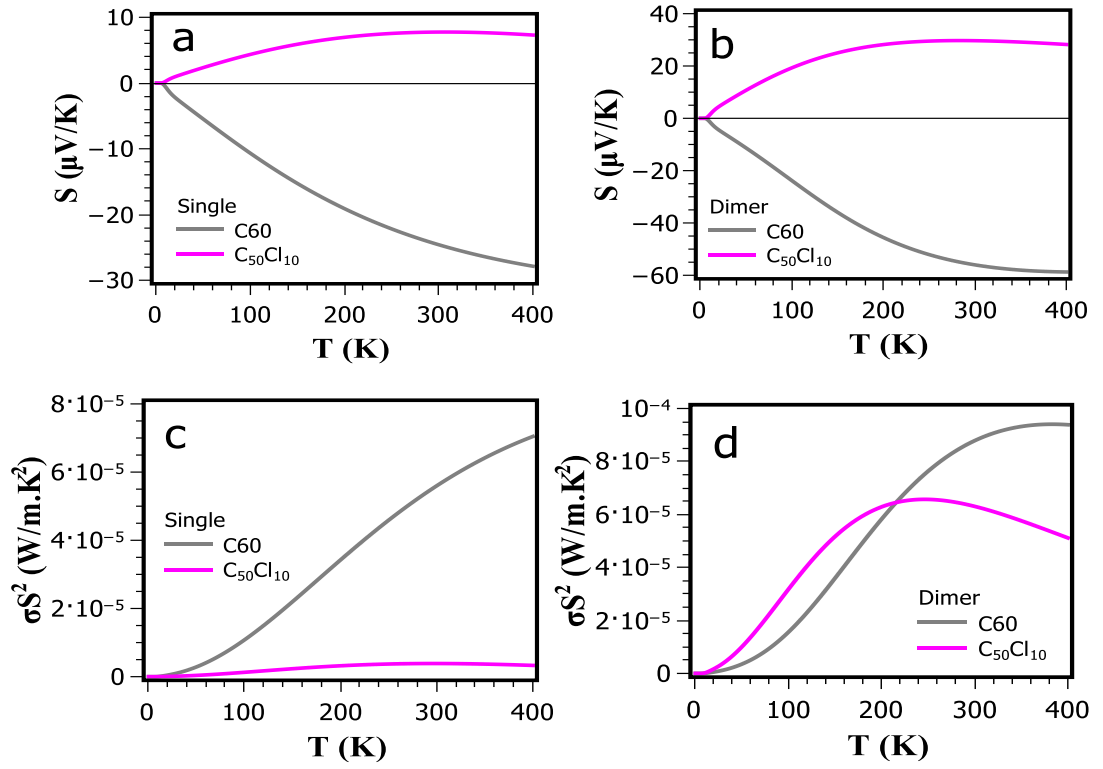
Figure 5.7. *The left column (Figs. a and c) show the Seebeck coefficients S and power factors σS² as a function of temperature at DFT-predicted Fermi energy E_F^{DFT} for the monomers in Figures 3a and 4a. The right column, (Figs. b and d) show the Seebeck coefficient and power factors for the dimers in Figures 3b and 4b.*
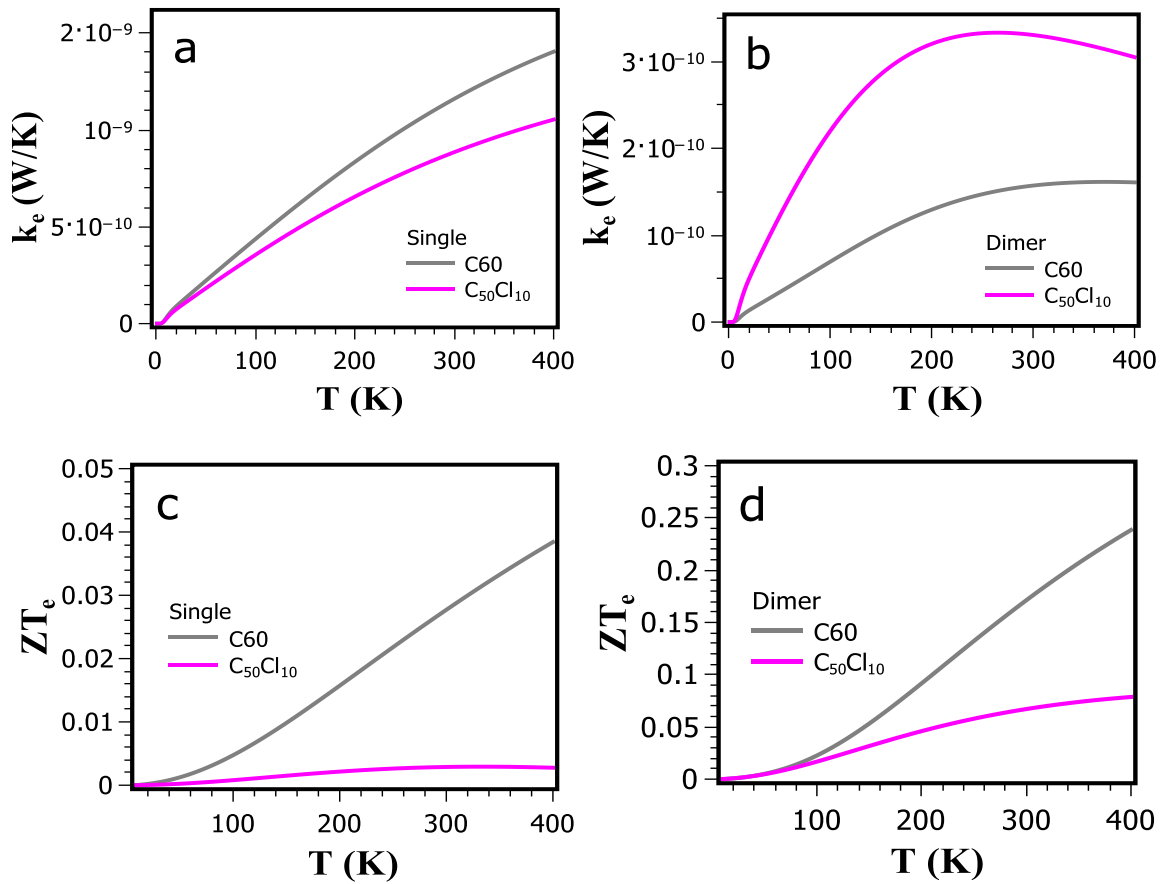
Figure 5.8. *The left column, Figures (a and c) shows a comparison of electronic thermal conductance (k_e) and electronic figure of merit (ZT_e) as a function of temperature at DFT-predicted Fermi energy E_F^{DFT} between the systems in Figures 3a and 4a. The upper panel, Figures (a and b) show the comparison of electronic thermal conductance (k_e) the lower panel, Figures (c and d) show electronic figure of merit (ZT_e) for the systems in Figures 3b and 4b.*

At present there are no experiments addressing the thermoelectric properties of exohedral fullerenes. Our intention is that this will be the first in the field and will stimulate a series of new experiments and theoretical studies in this direction. Indeed, I are already discussing this and other potential exohedral fullerenes with experimentalists in the Fullerene Factory in the Materials Department of Oxford University, but it will be another year before these are synthesised and measured. I'm

confident in my predictions and do calculate the power factor and the electron figure of merit ZTe. To calculate ZT, a separate study of phonon thermal transport needed.

5.3. Summary

In this chapter, I have computed that the thermopower and electronic contribution to the figure of merit ZT of molecular junctions and shown that they can be enhanced by the manipulation of inter-molecular interactions at ambient conditions. I have found that the exohedral fullerene $C_{50}Cl_{10}$ provides a thermoelectric material with a positive Seebeck coefficient of opposite sign to that of C_{60}. Furthermore, in common with C_{60}, the Seebeck coefficient can be increased by placing more than one $C_{50}Cl_{10}$ in series. For a single $C_{50}Cl_{10}$, I find S=+8 µV/K and for two $C_{50}Cl_{10}$'s in series I find S=+30 µV/K. These are comparable with the Seebeck coefficients of pristine C_{60}, which I predict to be S=-21 µV/K and S=-56 µV/K for a C_{60} monomer and C_{60} dimer respectively. Fullerenes smaller than C_{60} are predicted to have unusual electronic and mechanical properties that arise mainly from the high curvature of their molecular surface [150-156]. The above results suggest that thermoelectricity should be added to this list of fascinating properties and that exohedral fullerenes provide a new class of thermoelectric materials with desirable properties, which complement those of all-carbon fullerenes.

Chapter 6

Conclusion

In conclusion, to build the concept in this thesis as a first step I introduced the methods used through my work. Starting with density functional theory and scattering theory of quantum transport, I discussed how to calculate electronic and thermoelectric properties of molecular systems. In particular, I have focused on the electronic and thermoelectric properties of buckyballs. First, I addressed the possible of use fullerenes as molecular electronic components and the possibility of using C_{60} and $C_{50}Cl_{10}$ as anchors for molecular junctions. Then, I discussed using them as actual thermoelectric devices and demonstrated that the exohedral fullerene $C_{50}Cl_{10}$ provides a thermoelectric material with a positive Seebeck coefficient of opposite sign to that of C_{60}. Furthermore, in common with C_{60}, the Seebeck coefficient can be increased by placing more than one $C_{50}Cl_{10}$ in series. Fullerenes smaller than C_{60} are predicted to have unusual electronic and mechanical properties that arise mainly from their molecular surface. My thesis demonstrates that thermoelectricity should be added to this list of fascinating properties and that exohedral fullerenes provide a new class of thermoelectric materials with desirable properties, which complement those of all-carbon fullerenes.

The field of molecular thermoelectrics is in its infancy and ongoing studies are needed to highlight how chemical modifications of molecules can be used to tune the thermopower and reverse its sign. $C_{50}Cl_{10}$ is only one of a large number of available

exohedral fullerenes and it remains to be seen what levels of performance are attainable. For $C_{50}Cl_{10}$, the change in sign arises because the Fermi energy is located above the LUMO resonance, whereas in C_{60}, it is located below the LUMO resonance. The geometrical and electronics structure $C_{50}Cl_{10}$ is very different from that of C_{60} and therefore it is not possible to consider a smooth change, which connects the electronic structure of one with the other. For the future it would be of interest to study exohedral fullerenes obtained by adding eg metal atoms to the outside of the cage, without changing the number of carbon atoms. Since the Seebeck coefficient is an intrinsic property, studies of single molecules inform the design of thin film materials formed from monolayer of multi-layers of molecules. The increase in Seebeck coefficient for the dimer compared with the monomer suggests that performance can be increased by increasing the number of layers in such molecular films, at least until the film thickness reaches the inelastic scattering length.

Having demonstrated fullerenes could also form unique molecular structures with non-trivial shapes. Furthermore, buckyballs have the potential to overcome one of the biggest challenges in the molecular electronics which is how to connect the scatterer to the leads. Based on the above positive aspects of carbon fullerenes open a wide and unparalleled opportunity to be key components of future nanoelectronics devices such as nanofluidic devices or sub-10-nm circuitry, because there is a need to design new materials with a high Seebeck coefficient and a high thermoelectric figure of merit.

The work presented in this thesis is only a beginning and there are many suggestions for future study. One interesting study would be an assessment of the transport properties when using buckyballs and exohedral buckyballs in peapods systems, as

outlined in the appendix, which should increase their electronic communication. Another would involve a study of defects in the cage structure, which are common features of networks of three-fold vertices [159] and in particular graphene [160]. It would also be of interest to study how transport properties change when alternative electrode materials are used such as platinum, palladium or iron [161,162] or even superconducting electrodes [163-165]. More recently, electroburnt graphene-based electrodes have been developed for molecular-scale electronics [166-169], which when combined with the fullerenes discussed in this thesis, may form a basis for future carbon-based electronic devices. Finally, for the purpose of computing the full thermoelectric figure of merit, it would be of interest to utilise methods for computing phonon transport through nanostructures [170,171] to obtain the contribution from phonons to the thermal conductance through fullerene-based molecular junctions.

In appendix, I have presented a study of the electronic and thermoelectric properties of three kinds of nanotube (11,11) materials, carbon nanotube peapods. The calculation shows that for both the magnitude and sign on thermopower S are changed by introducing $C_{50}Cl_{10}$. In the (11,11) CNTs. I also found that electron transport is sensitive to the orientation of $C_{50}Cl_{10}$. Hopefully, my research will be widely read in the future, because there is a need to design new materials with a high Seebeck coefficient and a high thermoelectric figure of merit, this is an expanding and vibrant area of research.

Bibliography

1.	Saito, R., G. Dresselhaus, and M.S. Dresselhaus, Physical properties of carbon nanotubes. Vol. 35. 1998: World Scientific.
2.	Burchell, T.D., Carbon materials for advanced technologies. 1999, Elsevier science.
3.	Diudea, M.V. and C.L. Nagy, Periodic nanostructures. 2007: Springer Publishing Company, Incorporated.
4.	Biswas, C. and Y.H. Lee, Graphene versus carbon nanotubes in electronic devices. Advanced Functional Materials, 2011. 21(20): p. 3806-3826.
5.	Kroto, H.W., et al., C 60: buckminsterfullerene. Nature, 1985. 318(6042): p. 162-163.
6.	Krätschmer, W., et al., C 60: a new form of carbon. Nature, 1990. 347(6291): p. 354-358.
7.	Iijima, S., Helical microtubules of graphitic carbon. nature, 1991. 354(6348): p. 56-58.
8.	Ebbesen, T. and P. Ajayan, Large-scale synthesis of carbon nanotubes. Nature, 1992. 358(6383): p. 220-222.
9.	Wong, H., and Akinwande, D. (2010). Carbon Nanotube and Graphene Device Physics, Cambridge: Cambridge University press.
10.	Norbert N. Quantum Transport in Carbon-based Nanostructures. Ph.D. thesis, Universität Regensburg (2007)
11.	A.K. Geim and K.S. Novoselov. The Rise of Graphene. Nature Materials, 6:193–191, 2007.
12.	R. Saito, Physical Properties of Carbon Nanotubes, World Scientific Publishing Company, London, 1998.
13.	Burchell, T.D., Carbon materials for advanced technologies. 1999, Elsevier science.
14.	Diudea, M.V. and C.L. Nagy, Periodic nanostructures. 2007: Springer Publishing Company, Incorporated.
15.	Bernier, P., Science and Technology of Fullerene Materials: Symposium Held November 28-December 2, 1994, Boston, Massachusetts, USA. 1995: Materials Research Society.
16.	Oliveras, S. O. (2009). Theoretical Studies of Exohedrals Reactivity of Fullerene Compounds. Universitat De Girona.
17.	Thakral, S., & Mehta, M. (2006). Fullerenes: An Introduction and Overview of Their ullerenes: An Introduction and Overview of Their. Indian Journal of Pharmaceutical Sciences .
18.	Troyanov, & Kemnitz, E. (2016). Synthesis and Structure of Halogenated Fullerenes. Current Organic Chemistry .
19.	Simeonov, K. S., Amsharov, K. Y., & Jansen, M. (2008). Chlorinated Derivatives of C78-Fullerene Isomers with Unusually Short

Intermolecular Halogen–Halogen Contacts. Chem. Eur. J. 14, , 9585 – 9590.

20. u, X., Chen, Z., Thiel, W., Schleyer, P. V., Huang, R., & Zheng, L. (2004). Properties of Fullerene[50] and D5h Decachlorofullerene[50]: A Computational Study. Journal of Americal Chemical Society

21. Xie, S.-Y., Gao, F., Lu, X., Huang, R. B., Wang, C. R., Zhang, X., et al. (2004). Capturing the Labile Fullerene[50] as C50Cl10. SCIENCE VOL 304

22. Laith Algharagholy, S.W.D.B., Thomas Pope, and Colin J. Lambert, Sculpting molecular structures from bilayer graphene and other materials. Phys. Rev. B, 2012. 86(7): p. 075427.

23. Feynman, R.P., There's plenty of room at the bottom. Engineering and Science, 1960. 23(5): p. 22-36.

24. Moore, G., Cramming more components onto integrated circuits. Electronics, 1965. 38(8).

25. Sparks, R.E., MECHANICAL AND ELECTRICAL CONTROL OF TRANSPORT THROUGH SINGLE MOLECULES in Physics. 2012, PhD thesis, Lancaster University.

26. M., G.I., QUANTUM TRANSPORT IN CARBON NANOTUBES AND SINGLE MOLECULES, in Physics. 2004, PhD thesis, Lancaster University.

27. Oroszlany, L., CARBON BASED NANODEVICE, in Physics. 2009, PhD thesis, Lancaster University.

28. Joachim, C., J. Gimzewski, and A. Aviram, Electronics using hybrid-molecular and mono-molecular devices. Nature, 2000. 408(6812): p. 541-548.

29. Fritzsche, W., et al., Making electrical contact to single molecules. Nanotechnology, 1998. 9(3): p. 177.

30. Hipps, K., It's all about contacts. Science, 2001. 294(5542): p. 536-537.

31. Cui, X., et al., Reproducible measurement of single-molecule conductivity. Science, 2001. 294(5542): p. 571-574.

32. Argaman, N. and G. Makov, Density Functional Theory--an introduction. arXiv preprint physics/9806013, 1998.

33. Dronskowski, R., Computational chemistry of solid state materials2005: Wiley Online Library.

34. Eschrig, H., The Fundamentals of Density Functional Theory (revised and extended version). Edition am Gutenbergplatz, Leipzig, Germany, 2003. 9.

35. Kohn, W., A.D. Becke, and R.G. Parr, Density functional theory of electronic structure. The Journal of Physical Chemistry, 1996. 100(31): p. 12974-12980.

36. Martin, R.M., Electronic structure: basic theory and practical methods2004: Cambridge university press.

37. Parr, R.G. and Y. Weitao, Density-functional theory of atoms and molecules. Vol. 16. 1994: Oxford University Press, USA.

38. Kumar, A., A Brief Introduction to Thomas-Fermi Model in Partial Differential Equations. 2012.

39. Lieb, E.H., Thomas-Fermi and related theories of atoms and molecules. Reviews of Modern Physics, 1981. 53(4): p. 603.

40. Gross, E.K. and R.M. Dreizler, Density functional theory. Vol. 337. 1995: Springer.

41. Hohenberg, P.a.W.K., Inhomogeneous Electron Gas. Physical Review, 1964. 136(3B): p. B864-B871.

42. Kohn, W. and L.J. Sham, Self-Consistent Equations Including Exchange and Correlation Effects. Physical Review, 1965. 140(4A): p. A1133-A1138.

43. Koch, W. and M.C. Holthausen, A chemist's guide to density functional theory. Vol. 2. 2001: Wiley-Vch Weinheim.

44. Geerlings, P., F. De Proft, and W. Langenaeker, Conceptual density functional theory. Chemical Reviews-Columbus, 2003. 103(5): p. 1793-1874.

45. Eschrig, H., K. Koepernik, and I. Chaplygin, Density functional application to strongly correlated electron systems. Journal of Solid State Chemistry, 2003. 176(2): p. 482-495.

46. Ziesche, P. and F. Tasnádi, Methods for electronic-structure calculations: Overview from a reduced-density-matrix point of view. International journal of quantum chemistry, 2004. 100(4): p. 495-508.

47. Thomas, L.H. The calculation of atomic fields. in Mathematical Proceedings of the Cambridge Philosophical Society. 1927. Cambridge Univ Press.

48. Burke, K., the ABC of DFT. Department of Chemistry, University of California, 2007.

49. Walker, B., C. Molteni, and N. Marzari, Ab initio molecular dynamics of metal surfaces. Journal of Physics: Condensed Matter, 2004. 16(26): p. S2575.

50. Kohn, W., Nobel Lecture: Electronic structure of matter—wave functions and density functionals*. Reviews of Modern Physics, 1999. Vol. 71, No. 5: p. 1253-1266.

51. Levy, M., Electron densities in search of Hamiltonians. Physical Review A, 1982. 26(3): p. 1200.

52. Lima, N., L. Oliveira, and K. Capelle, Density-functional study of the Mott gap in the Hubbard model. EPL (Europhysics Letters), 2007. 60(4): p. 601.

53. March, N.H., Self-consistent fields in atoms. 1975.

54. Kohn, W. and L.J. Sham, Self-consistent equations including exchange and correlation effects1965: APS.

55. Ceperley, D.M. and B. Alder, Ground state of the electron gas by a stochastic method. Physical Review Letters, 1980. 45(7): p. 566-569.

56. Perdew, J.P. and A. Zunger, Self-interaction correction to density-functional approximations for many-electron systems. Physical Review B, 1981. 23(10): p. 5048-5079.

57. Naghavi, S.S., Theoretical Study of correlated systems using hybrid functionals2011.

58. Hedin, L. and S. Lundqvist, Effects of electron-electron and electron-phonon interactions on the one-electron states of solids. Solid State Physics, 1970. 23: p. 1-181.

59. Vosko, S.H., L. Wilk, and M. Nusair, Accurate spin-dependent electron liquid correlation energies for local spin density calculations: a critical analysis. Canadian Journal of Physics, 1980. 58(8): p. 1200-1211.

60. Perdew, J.P., K. Burke, and M. Ernzerhof, Generalized gradient approximation made simple. Physical Review Letters, 1996. 77(18): p. 3865-3868.

61. Becke, A.D., Density-functional exchange-energy approximation with correct asymptotic behavior. Physical Review A, 1988. 38(6): p. 3098.

62. Hammer, B., L.B. Hansen, and J.K. Nørskov, Improved adsorption energetics within density-functional theory using revised Perdew-Burke-Ernzerhof functionals. Physical Review B, 1999. 59(11): p. 7413.

63. Perdew, J.P. and Y. Wang, Accurate and simple analytic representation of the electron-gas correlation energy. Physical Review B, 1992. 45(23): p. 13244-13249.

64. Soler, J.M., et al., The SIESTA method for ab initio order-N materials simulation. Journal of Physics: Condensed Matter, 2002. 14(11): p. 2745.

65. Sánchez-Portal, D., et al., Density-functional method for very large systems with LCAO basis sets. International journal of quantum chemistry, 1998. 65(5): p. 453-461.

66. E. Artacho, J.D.G., A. Junquera, R. M. Martin, P. Ordejon, D. Sanchez-Portal, and J. M. Soler. SIESTA 3.1 User's Guide. 2011.

67. Ordejón, P., et al., Unconstrained minimization approach for electronic computations that scales linearly with system size. Physical Review B, 1993. 48(19): p. 14646.

68. Kleinman, L. and D. Bylander, Efficacious form for model pseudopotentials. Physical Review Letters, 1982. 48(20): p. 1425-1428.

69. Hamann, D., M. Schlüter, and C. Chiang, Norm-conserving pseudopotentials. Physical Review Letters, 1979. 43(20): p. 1494-1497.

70. Troullier, N. and J.L. Martins, Efficient pseudopotentials for plane-wave calculations. Physical Review B, 1991. 43(3): p. 1993.

71. Troullier, N. and J. Martins, A straightforward method for generating soft transferable pseudopotentials. Solid State Communications, 1990. 74(7): p. 613-616.

72. Boys, S. and F.d. Bernardi, The calculation of small molecular interactions by the differences of separate total energies. Some procedures with reduced errors. Molecular Physics, 1970. 19(4): p. 553-566.

73. Haynes, P., et al., Elimination of basis set superposition error in linear-scaling density-functional calculations with local orbitals optimised in situ. Chemical physics letters, 2006. 422(4): p. 345-349.

74. Mierzwicki, K. and Z. Latajka, Basis set superposition error in *N*-body clusters. Chemical physics letters, 2003. 380(5): p. 654-664.

75.	Senent, M. and S. Wilson, Intramolecular basis set superposition errors. International journal of quantum chemistry, 2001. 82(6): p. 282-292.

76.	Daza, M.C., et al., Basis set superposition error-counterpoise corrected potential energy surfaces. Application to hydrogen peroxide··· X (X= F−, Cl−, Br−, Li+, Na+) complexes. The Journal of Chemical Physics, 1999. 110(24): p. 11806-11813.

77.	Boese, A.D., et al., Effects of counterpoise correction and basis set extrapolation on the MP2 geometries of hydrogen bonded dimers of ammonia, water, and hydrogen fluoride. Phys. Chem. Chem. Phys., 2010. 13(3): p. 1230-1238.

78.	Feynman, R., Forces in molecules. Physical Review, 1939. 56(4): p. 340.

79.	Landauer, R., Spatial variation of currents and fields due to localized scatterers in metallic conduction. IBM Journal of Research and Development, 1957. 1(3): p. 223-231.

80.	Büttiker, M., et al., Generalized many-channel conductance formula with application to small rings. Physical Review B, 1985. 31(10): p. 6207.

81.	Datta, S., Electronic transport in mesoscopic systems1997: Cambridge university press.

82.	Brouwer, P., Scattering approach to parametric pumping. Physical Review B, 1998. 58(16): p. R10135-R10138.

83.	Finch, C.M., AN UNDERSTANDING OF THE ELECTRICAL CHARACTERISTICS OF ORGANIC MOLECULAR DEVICES, in Physics Department2008, Lancaster University.

84.	Economou, E.N., Green's functions in quantum physics1984: Springer.

85.	Mello, P.A. and N.K. Kumar, Quantum transport in mesoscopic systems: complexity and statistical fluctuations: a maximum-entropy viewpoint. Vol. 4. 2004: Oxford University Press on Demand.

86.	Fisher, D.S. and P.A. Lee, Relation between conductivity and transmission matrix. Physical Review B, 1981. 23(12): p. 6851-6854.

87.	Visontai, D., Quantum and Classical Dynamics of Molecule Size Systems, in Physics Department2013, Lancaster University.

88.	Sanvito, S., Giant Magnetoresistance and Quantum Transport in Magnetic Hybrid Nanostructures, in Physics Department2008, Lancaster University.

89.	Finch, C.M., An understanding of electrical characteristics of organic molecular devices, in Physics Department2008, Lancaster University.

90.	Aoki, H., Real-space renormalisation-group theory for Anderson localisation: Decimation method for electron systems. Journal of Physics C: Solid State Physics, 1980. 13(18): p. 3369.

91.	Lema, F. and C. Wiecko, Multifractality of the Anderson and binary alloy localized eigenstates by the improved decimation method. Physica Scripta, 1993. 47(2): p. 129.

92.	Leadbeater, M. and C.J. Lambert, A decimation method for studying transport properties of disordered systems. Annalen der physik, 1998. 7(5-6): p. 498-502.

93. MacKinnon, J.G. and H. White, Some heteroskedasticity-consistent covariance matrix estimators with improved finite sample properties. Journal of Econometrics, 1985. 29(3): p. 305-325.

94. Ryndyk, D., et al., Green function techniques in the treatment of quantum transport at the molecular scale, in Energy Transfer Dynamics in Biomaterial Systems2009, Springer. p. 213-335.

95. Lambert, C., V. Hui, and S. Robinson, Multi-probe conductance formulae for mesoscopic superconductors. Journal of Physics: Condensed Matter, 1993. 5(25): p. 4187.

96. Finch, C.M., et al., Conformation dependence of molecular conductance: chemistry versus geometry. Journal of Physics: Condensed Matter, 2008. 20(2): p. 022203.

97. I. M. Grace, S.W.B., C. J. Lambert, and J. H. Jefferson, Molecular Nanowires and Other Quantum Objects. NATO ASI Series, 2004: p. pages 13-21.

98. Athanasopoulos, S., Electronic Properties of Hybrid Carbon Nanotubes, in Physics Department2005, Lancaster University.

99. Leadbeater, M. and C. Lambert, Superconductivity-induced phase-periodic transport in nanoscale structures. Physical Review B, 1997. 56(2): p. 826-831.

100. Koltai, J., J. Cserti, and C. Lambert, Andreev bound states for a superconducting-ferromagnetic box. Physical Review B, 2004. 69(9): p. 092506.

101. Polinák, P., et al., Andreev drag effect via magnetic quasiparticle focusing in normal-superconductor nanojunctions. Physical Review B, 2006. 74(13): p. 132508.

102. Rocha, A.R., et al., Spin and molecular electronics in atomically enerated orbital landscapes. Physical Review B, 2006. 73(8): p. 085414.

103. Breit, G. and E. Wigner, Capture of slow neutrons. Physical Review, 1936. 49(7): p. 519.

104. Fano, U., Effects of configuration interaction on intensities and phase shifts. Physical Review, 1961. 124(6): p. 1866.

105. Papadopoulos, T., I. Grace, and C. Lambert, Control of electron transport through Fano resonances in molecular wires. Physical Review B, 2006. 74(19): p. 193306.

106. Ke, S.-H., W. Yang, and H.U. Baranger, Quantum-interference-controlled molecular electronics. Nano letters, 2008. 8(10): p. 3257-3261.

107. Stadler, R., Quantum interference effects in electron transport through nitrobenzene with pyridil anchor groups. Physical Review B, 2009. 80(12): p. 125401.

108. Fano, U., Effects of Configuration Interaction on Intensities and Phase Shifts. Physical Review, 1961. 124(6): p. 1866-1878.

109. Kobayashi, K., et al., Tuning of the Fano effect through a quantum dot in an Aharonov-Bohm interferometer. Physical Review Letters, 2002. 88(25): p. 256806.

110. Finch, C., V. Garcia-Suarez, and C. Lambert, Giant thermopower and figure of merit in single-molecule devices. Physical Review B, 2009. 79(3): p. 033405.

111. Stafford, C.A., D.M. Cardamone, and S. Mazumdar, The quantum interference effect transistor. Nanotechnology, 2007. 18(42): p. 424014.

112. Stadler, R., M. Forshaw, and C. Joachim, Modulation of electron transmission for molecular data storage. Nanotechnology, 2003. 14(2): p. 138.

113. Baer, R. and D. Neuhauser, Phase coherent electronics: a molecular switch based on quantum interference. Journal of the American Chemical Society, 2002. 124(16): p. 4200-4201.

114. Soler, José M., et al. "The SIESTA method for ab initio order-N materials simulation." Journal of Physics: Condensed Matter 14.11 (2002): 2745.

115. Troullier, Norman, and José Luís Martins. "Efficient pseudopotentials for plane-wave calculations." Physical review B 43.3 (1991): 1993.

116. Perdew, John P., Kieron Burke, and Matthias Ernzerhof. "Generalized gradient approximation made simple." Physical review letters 77.18 (1996): 3865.

117. Hammer, B. H. L. B., Lars Bruno Hansen, and Jens Kehlet Nørskov. "Improved adsorption energetics within density-functional theory using revised Perdew-Burke-Ernzerhof functionals." Physical Review B 59.11 (1999): 7413.

118. C. Evangeli, K. Gillemot, E. Leary, M. T. González, G. Rubio-Bollinger, C. J. Lambert, and N. Agraït, "Engineering the thermopower of C60 molecular junctions," Nano Lett., vol. 13, no. 5, pp. 2141–2145, 2013.

119. C. A. Martin, D. Ding, J. K. Sø rensen, T. Bjø rnholm, J. M. V. Ruitenbeek, and H. S. J. V. D. Zant, _Fullerene-Based Anchoring Groups for Molecular Electronics,_ pp. 13198_13199, 2008.

120. C. J. Lambert, "Basic concepts of quantum interference and electron transport in single-molecule electronics," Chem. Soc. Rev., vol. 44, no. 4, pp. 875–888, 2015.

121. K. Baheti, J. a. Malen, P. Doak, P. Reddy, S. Y. Jang, T. D. Tilley, A. Majumdar, and R. a. Segalman, "Probing the chemistry of molecular heterojunctions using thermoelectricity," Nano Lett., vol. 8, no. 2, pp. 715–719, 2008.

122. S. K. Yee, J. A. Malen, A. Majumdar, and R. A. Segalman, "Thermoelectricity in Fullerene–Metal Heterojunctions," Nano Lett., vol. 11, no. 10, pp. 4089–4094, 2011.

123. S. K. Lee, T. Ohto, R. Yamada, and H. Tada, "Thermopower of benzenedithiol and C60 molecular junctions with Ni and Au electrodes.," Nano Lett., vol. 14, no. 9, pp. 5276–80, 2014.

124. J. Malen, P. Doak, and K. Baheti, "Identifying the length dependence of orbital alignment and contact coupling in molecular heterojunctions," Nano Lett., vol. 9, no. 3, pp. 1164–1169, 2009.

125. A. Tan, J. Balachandran, S. Sadat, V. Gavini, B. D. Dunietz, S.-Y. Jang, and P. Reddy, "Effect of length and contact chemistry on the electronic structure and thermoelectric properties of molecular junctions.," J. Am. Chem. Soc., vol. 133, no. 23, pp. 8838–41, 2011.

126. J. Balachandran and P. Reddy, "End-group-induced charge transfer in molecular junctions: effect on electronic-structure and thermopower," J. Phys. Chem. Lett., vol. 3, no. 15, pp. 1962–1967, 2012.

127. J. R. Widawsky, W. Chen, H. Vázquez, T. Kim, R. Breslow, M. S. Hybertsen, and L. Venkataraman, "Length-dependent thermopower of highly conducting Au-C bonded single molecule junctions," Nano Lett., vol. 13, no. 6, pp. 2889–2894, 2013.

128. W. B. Chang, C. Mai, M. Kotiuga, J. B. Neaton, G. C. Bazan, and R. A. Segalman, "Controlling the Thermoelectric Properties of Thiophene-Derived Single-Molecule Junctions," Chem. Mater., vol. 26, no. 24, pp. 7229–7235, Nov. 2014.

129. C. Evangeli, K. Gillemot, E. Leary, M. T. González, G. Rubio-Bollinger, C. J. Lambert, and N. Agraït, "Engineering the thermopower of C60 molecular junctions," Nano Lett., vol. 13, no. 5, pp. 2141–2145, 2013.

130. Y. Kim, W. Jeong, K. Kim, W. Lee, and P. Reddy, "Electrostatic control of thermoelectricity in molecular junctions.," Nat. Nanotechnol., vol. 9, no. 11, pp. 881–5, 2014.

131. Víctor M García-Suárez, Colin J Lambert, David Zs Manrique andThomas Wandlowski, "Redox control of thermopower and figure of merit in phase-coherent molecular wires," Nanotechnology 25 205402 (2014)

132. L. Rincón-García, A. K. Ismael, C. Evangeli, I. Grace, G. Rubio-Bollinger, K. Porfyrakis, N. Agraït, and C. J. Lambert, "Molecular design and control of fullerene-based bi-thermoelectric materials," Nature Mater. 15, 289–293 (2016

133. A. Ismael, I. Grace, and C. Lambert, "Increasing the thermopower of crown-ether-bridged anthraquinones," Nanoscale, 2015.

134. A. Shakouri, "Thermoelectric power factor for electrically conductive polymers," Eighteenth Int. Conf. Thermoelectr. Proceedings, ICT'99 (Cat. No.99TH8407), no. c, pp. 402–406, 1999.

135. Al-Galiby, Q. H.; Sadeghi, H.; Algharagholy, L. A.; Grace, I.; Lambert, C.J."Tuning the thermoelectric properties of metallo-porphyrins" Nanoscale, 8, (4), 2428-2433 2016.

136. P. Reddy, S.-Y. Jang, R. A. Segalman, and A. Majumdar, "Thermoelectricity in Molecular Junctions," Science (80-.)., vol. 315, no. 5818, pp. 1568–1571, 2007.

137. J. a. Malen, S. K. Yee, A. Majumdar, and R. a. Segalman, "Fundamentals of energy transport, energy conversion, and thermal properties in organic-inorganic heterojunctions," Chem. Phys. Lett., vol. 491, no. 4–6, pp. 109–122, 2010.

138. J. a. Malen, P. Doak, K. Baheti, T. D. Tilley, A. Majumdar, and R. a. Segalman, "The nature of transport variations in molecular

heterojunction electronics," Nano Lett., vol. 9, no. 10, pp. 3406–3412, 2009.

139. J. R. Widawsky, P. Darancet, J. B. Neaton, and L. Venkataraman, "Simultaneous determination of conductance and thermopower of single molecule junctions," Nano Lett., vol. 12, no. 1, pp. 354–358, 2012.

140. H. Sadeghi, S. Sangtarash, and C. J. Lambert, "Oligoyne Molecular Junctions for Efficient Room Temperature Thermoelectric Power Generation," Nano Lett., vol. 15, no. 11, pp. 7467–7472, Oct. 2015.

141. David Zsolt Manrique, Qusiy Hibbeb Al-Galiby, Wenjing Hong, Colin J Lambert "A new approach to materials discovery for electronic and thermoelectric properties of single-molecule junctions" Nano Lett. 16, 1308−1316 2016

142. Algharagholy, L. A.; Al-Galiby, Q.; Marhoon, H. A.; Sadeghi, H.; Abduljalil, H. M.; Lambert, C. J. "Tuning thermoelectric properties of graphene/boron nitride heterostructures" Nanotechnology 26, (47), 475401 2015

143. Xie, S.-Y.; Gao, F.; Lu, X.; Huang, R.-B.; Wang, C.-R.; Zhang, X.; Liu, M.-L.; Deng, S.-L.; Zheng, L.-S. Science 2004, 304, (5671), 699-699.

144. Chen, Zhongfang. "The smaller fullerene C50, isolated as C50Cl10." Angewandte Chemie International Edition 43.36 (2004): 4690-4691.

145. Soler, José M., et al. "The SIESTA method for ab initio order-N materials simulation." Journal of Physics: Condensed Matter 14.11 (2002): 2745.

146. Troullier, Norman, and José Luís Martins. "Efficient pseudopotentials for plane-wave calculations." Physical review B 43.3 (1991): 1993.

147. Perdew, John P., Kieron Burke, and Matthias Ernzerhof. "Generalized gradient approximation made simple." Physical review letters 77.18 (1996): 3865.

148. Hammer, B. H. L. B., Lars Bruno Hansen, and Jens Kehlet Nørskov. "Improved adsorption energetics within density-functional theory using revised Perdew-Burke-Ernzerhof functionals." Physical Review B 59.11 (1999): 7413.

149. Ferrer, Jaime, et al. "GOLLUM: a next-generation simulation tool for electron, thermal and spin transport." New Journal of Physics 16.9 (2014): 093029.

150. K. M. Kadish, R. S. Ruoff, Eds., Fullerene: Chemistry, Physics and Technology (Wiley, New York, 2002).

151. Guo, Ting, et al. "Uranium Stabilization of C~ 2~ 8: A Tetravalent Fullerene." Science 257.5077 (1992): 1661-1664.

152. Kroto, H. W. "The stability of the fullerenes Cn, with n= 24, 28, 32, 36, 50, 60 and 70." Nature 329.6139 (1987): 529-531.

153. Piskoti, C., J. Yarger, and A. Zettl. "C36, a new carbon solid." Nature 393.6687 (1998): 771-774.

154. Koshio, Akira, et al. "A preparative scale synthesis of C36 by high-temperature laser-vaporization: purification and identification of

C36H6 and C36H6O." Journal of the American Chemical Society 122.2 (2000): 398-399.

155. Koshio, Akira, et al. "In situ laser-furnace TOF mass spectrometry of C36 and the large-scale production by arc-discharge." The Journal of Physical Chemistry B 104.33 (2000): 7908-7913.

156. Heath, James R. "Fullerenes: C60's smallest cousin." Nature 393.6687 (1998): 730-731.

157. Sedghi, G.; García-Suárez, V. M.; Esdaile, L. J.; Anderson, H. L.; Lambert, C. J.; Martín, S.; Bethell, D.; Higgins, S. J.; Elliott, M.; Bennett, N. "Long-range electron tunnelling in oligo-porphyrin molecular wires." Nat. Nanotechnol. (2011), 6, 517.

158. Zhao, X.; Huang, C.; Gulcur, M.; Batsanov, A. S.; Baghernejad, M.; Hong, W.; Bryce, M. R.; Wandlowski, T. "Oligo(aryleneethynylene)s with Terminal Pyridyl Groups: Synthesis and Length Dependence of the Tunnelling to Hopping Transition in Single-Molecule Conductances." Chem. Mat. (2013), 25, 4340.

159. CJ Lambert, DL Weaire, "Theory of the arrangement of cells in a network, " Metallography 14 (4), 307-318 (1981)

160. XH Zheng, GR Zhang, Z Zeng, VM García-Suárez, CJ Lambert, "Effects of antidots on the transport properties of graphene nanoribbons, " Physical Review B 80 (7), 075413 42 (2009)

161. VM García-Suárez, AR Rocha, SW Bailey, CJ Lambert, S Sanvito, J Ferrer, "Single-channel conductance of H 2 molecules attached to platinum or palladium electrodes," Physical Review B 72 (4), 045437 (2005)

162. VM García-Suárez, CM Newman, CJ Lambert, JM Pruneda, J Ferrer, "Optimized basis sets for the collinear and non-collinear phases of iron." Journal of Physics: Condensed Matter 16 (30), 5453 44 (2004)

163. VI Fal'Ko, CJ Lambert, AF Volkov, "Andreev reflections and magnetoresistance in ferromagnet-superconductor mesoscopic structures," Journal of Experimental and Theoretical Physics Letters 69 (7), 532-538 (1999)

164. VC Hui, CJ Lambert, "Andreev scattering, universal conductance fluctuations and phase periodic transport," Europhysics Letters 23 (3), 203 (1993)

165. CJ Lambert, R Raimondi, V Sweeney, AF Volkov "Boundary conditions for quasiclassical equations in the theory of superconductivity" Physical Review B 55 (9), 6015 (1997)

166. Sadeghi, H.; Algharagholy, L.; Pope, T.; Bailey, S.; Visontai, D.; Manrique, D.; Ferrer, J.; García-Suárez, V.; Sangtarash, S.; Lambert, C. J. "Graphene sculpturene nanopores for DNA nucleobase sensing. " The Journal of Physical Chemistry B 118 (24), 6908-6914 (2014)

167. JA Mol, CS Lau, WJM Lewis, H Sadeghi, C Roche, A Cnossen, JH Warner, C.J. Lambert, H.L. Anderson and G.A.D. "Graphene-porphyrin single-molecule transistors." Nanoscale 7 (31), 13181-13185 (2015)

168. S Bailey, D Visontai, CJ Lambert, MR Bryce, H Frampton, D Chappell, "A study of planar anchor groups for graphene-based single-molecule electronics.", Journal of chemical physics 140 (5), 054708 (2014)

169. Hatef Sadeghi, Gregory Rogers, Sara Sangtarash, Panagiotis Dallas, Kyriakos Porfyrakis, Jamie H Warner, Colin J Lambert, G Andrew D Briggs, Jan Mol, "Redox-dependent Franck–Condon blockade and Avalanche transport in a

graphene–fullerene single-molecule transistor. " Nano Letters 16 (1), 170-176 (2015)

170.   G. Fagas, A.G. Kozorezov, C.J. Lambert, J.K. Wigmore, A. Peacock,A. Poelaert, R. den Hartog, "Lattice dynamics of a disordered solid-solid interface" Physical Review B 60 (9), 6459 52 (1999)

171.   H Han, Y Zhang, N Wang, MK Samani, Y Ni, ZY Mijbil, M Edwards, … "Functionalization mediates heat transport in graphene nanoflakes. "Nature Communications 7 11281 (2016)

Appendix

Table. DFT calculation of the charge transferred between the chlorine atoms and fullerene C_{50}

	Neutral	With Cl	ΔN
C_{50}	200	198.67	+1.32
Cl_{10}	70	71.318	-1.318
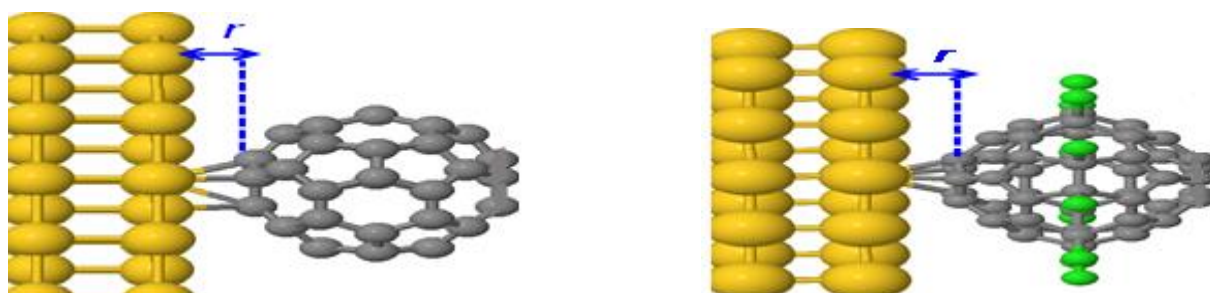
Figure. *Optimize distance between one gold electrode <111> and Buckyballs found r = 2.2 A*

After geometry relaxation, the distance between each molecule and the gold electrode was found to be 2.2 Å.

The Figures below show optimum configurations of single dimer, trimer and tetramer C_{50}, C_{60} and C50Cl10 junctions, in which the distance between two C_{50}s and C50Cl10s is $d = 3.2$ Å and the distance between C_{60} $d = 3.5$ Å. The distance between them and the electrodes is $r = 2.2$ Å. To compute their properties, we used the quantum transport code Gollum[30], which combines the Hamiltonian provided by the DFT code SIESTA with a Green's

function scattering formalism. Figures show the transmission coefficient $T(E)$ as a function of energy E for the junctions.
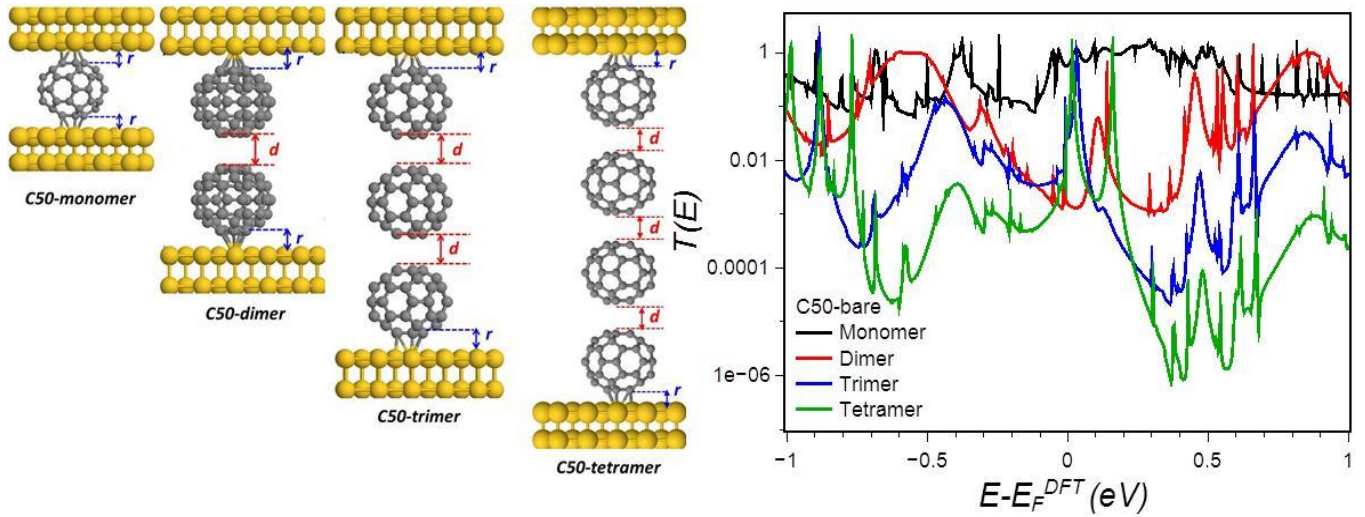
Figure. *(Right) the cofigurations of the systems containing C_{50} (single, dimer, trimer and tetramer) attached to the gold electrodes. (Left) DFT caculations of transmission coeffecients as a function of energy $T(E)$ for optimum configuration of single C_{50} (black), dimer (red), trimer (blue) and tetramer (green).*
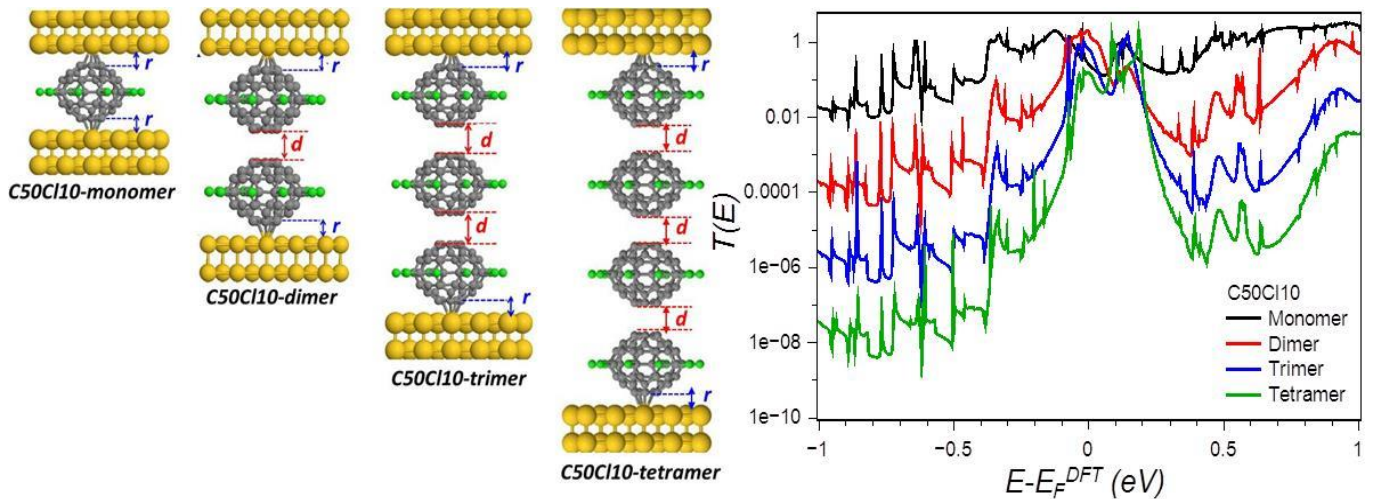
Figure. *(Right) the cofigurations of the systems containing $C_{50}Cl_{10}$ (single, dimer, trimer and tetramer) attached to the gold electrodes. (Left) DFT caculations of transmission coeffecients as a function of energy $T(E)$ for optimum configuration of single $C_{50}Cl_{10}$ (black), dimer (red), trimer (blue) and tetramer (green).*

136
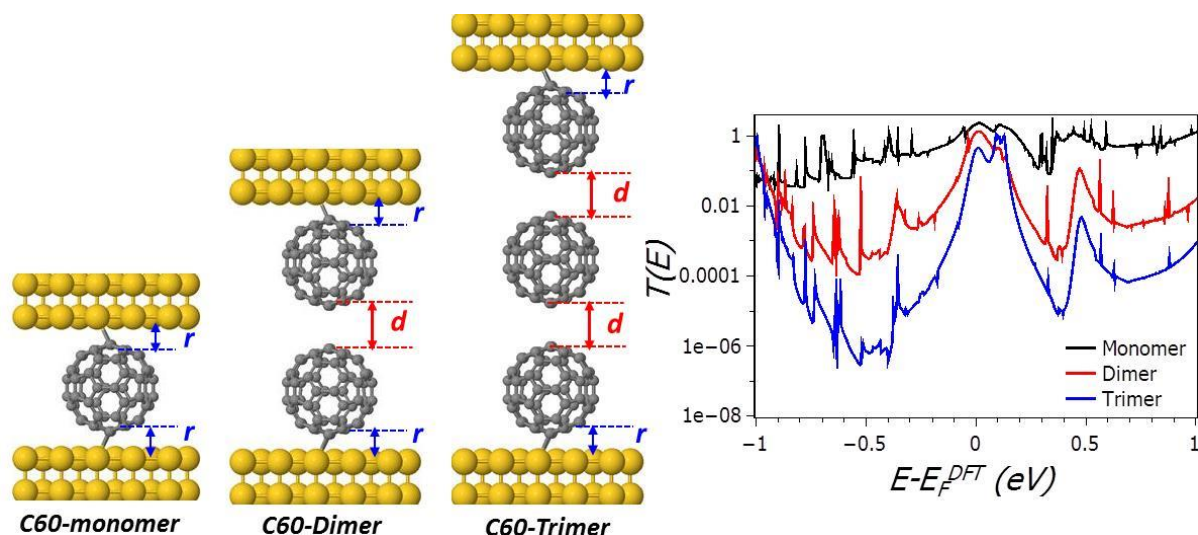
Figure. (Right) the cofigurations of the systems containing C_{60} (single, dimer and trimer) attached to the gold electrods. (Left) DFT caculations of transmission coeffecients as a function of energy $T(E)$ for optimum configuration of single C_{60} (black), dimer (red), trimer (blue) and tetramer (green).

For all the monomer dimer, trimer and tetramer, in agreement with, electrons near the Fermi energy transmit through the tail of the LUMO. Furthermore, the dimer transmission (red line) is much smaller than and lower than that of the monomer (black line) and sequentially for trimer and tetramer, due to the increase in length of the molecular bridge, leading to a higher slope at the Fermi energy and a higher thermopower for the dimer, trimer and then tetramer.
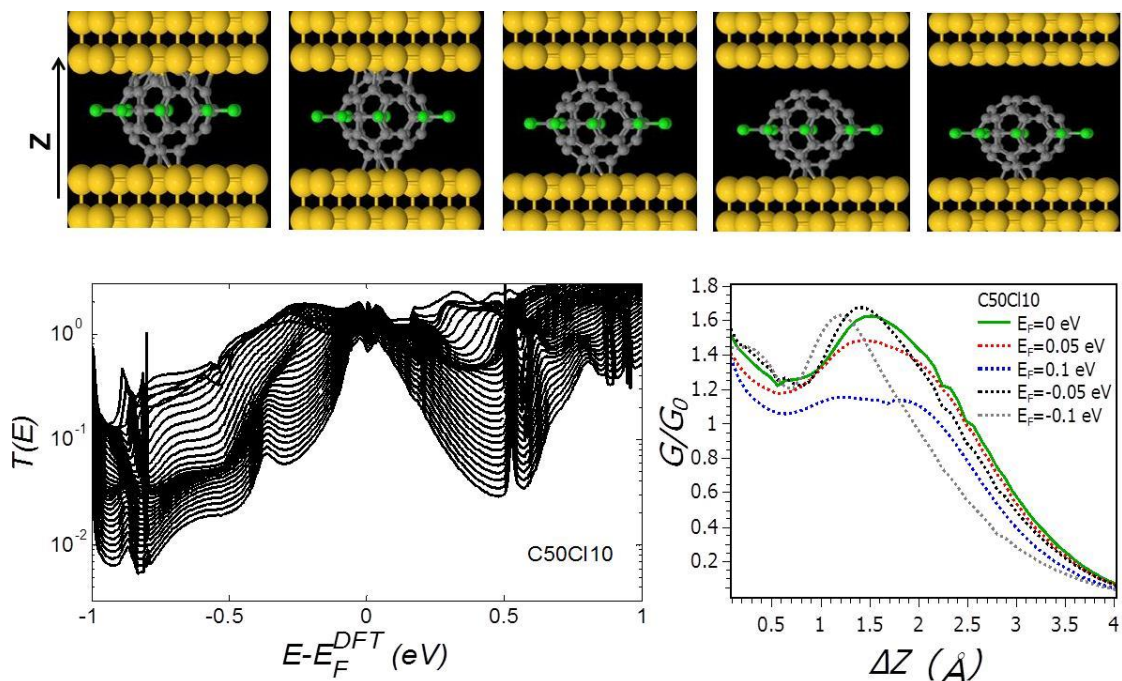
Figure. *Orientation of the $C_{50}Cl_{10}$ molecule with respect to the gold leads. Example transmission curves and Transmission coefficient as a function of orientation conductance for all orientations and binding sites as a function of the electrode separation in the case of a single $C_{50}Cl_{10}$.*
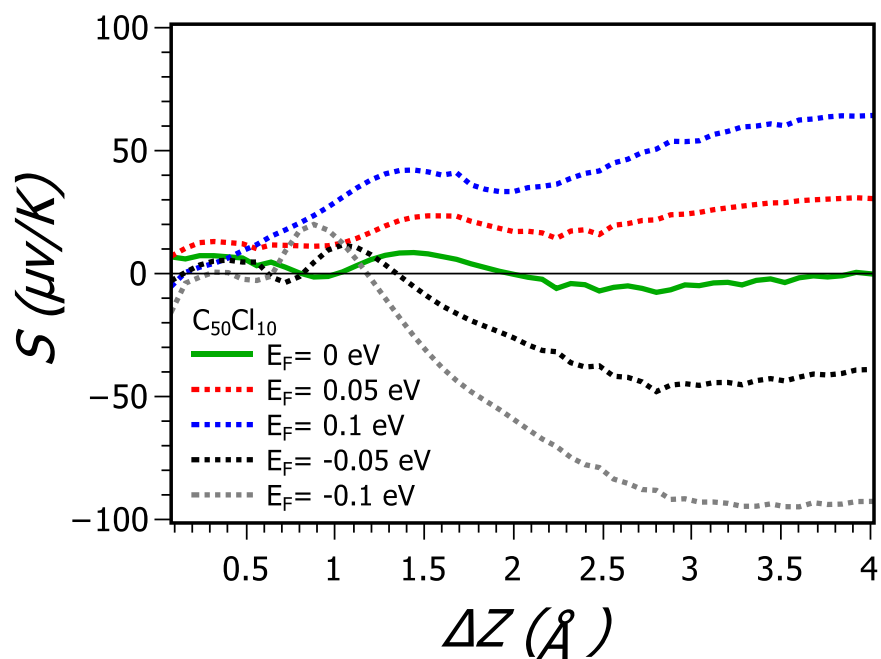
Figure. *Theoretical approaching curves of the thermopower for a single $C_{50}Cl_{10}$ obtained by recalculating S at a number of different E_F. Thermopower S versus orientation different substrate distances z at a value of E_F.*

C$_{50}$Cl$_{10}$ Rotation at CNT (11,11):
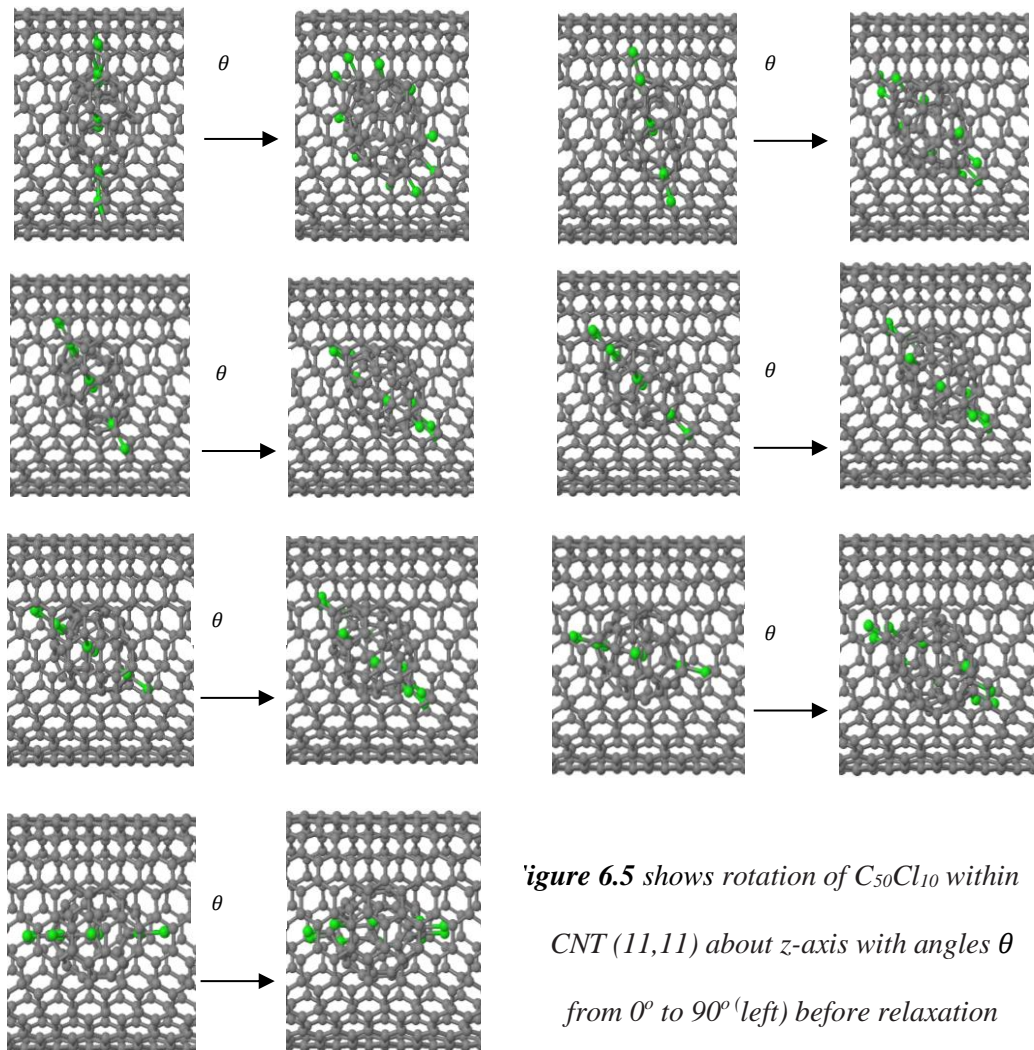
Figure 6.5 shows rotation of C$_{50}$Cl$_{10}$ within CNT (11,11) about z-axis with angles θ from 0° to 90° (left) before relaxation and (right) after relaxation.

Peapods:
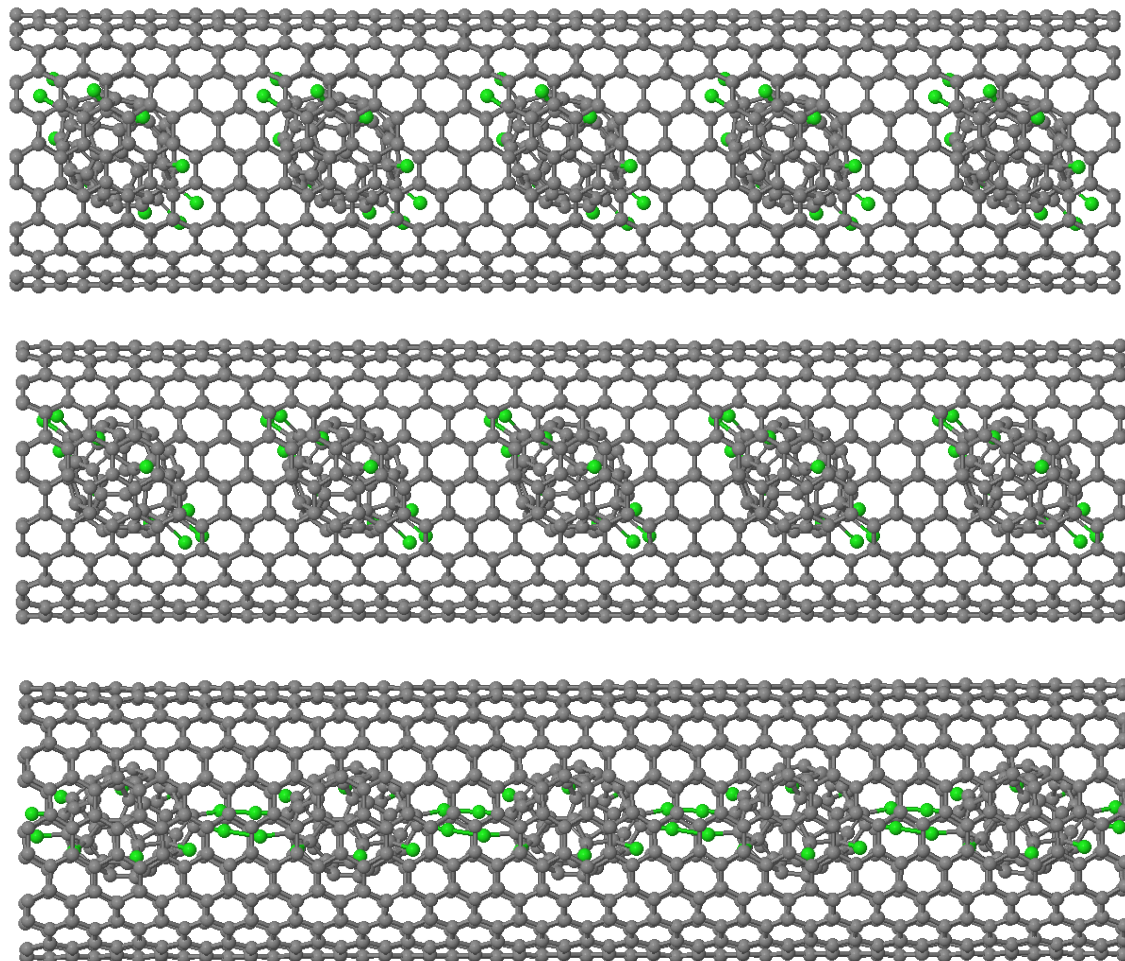
Figure 6.6 *shows the encapsulation a wire of $C_{50}Cl_{10}$s within CNT (11,11) in z-axis and the change of angles with a rotation of $C_{50}Cl_{10}$ from angles $\theta = 0^o$ to angles $\theta = 45^o$ but 90° not change of angle after relaxation.*

Band Structure

(a)

(b)

(c)

θ=0

(d)

θ=45

(e)

θ=90
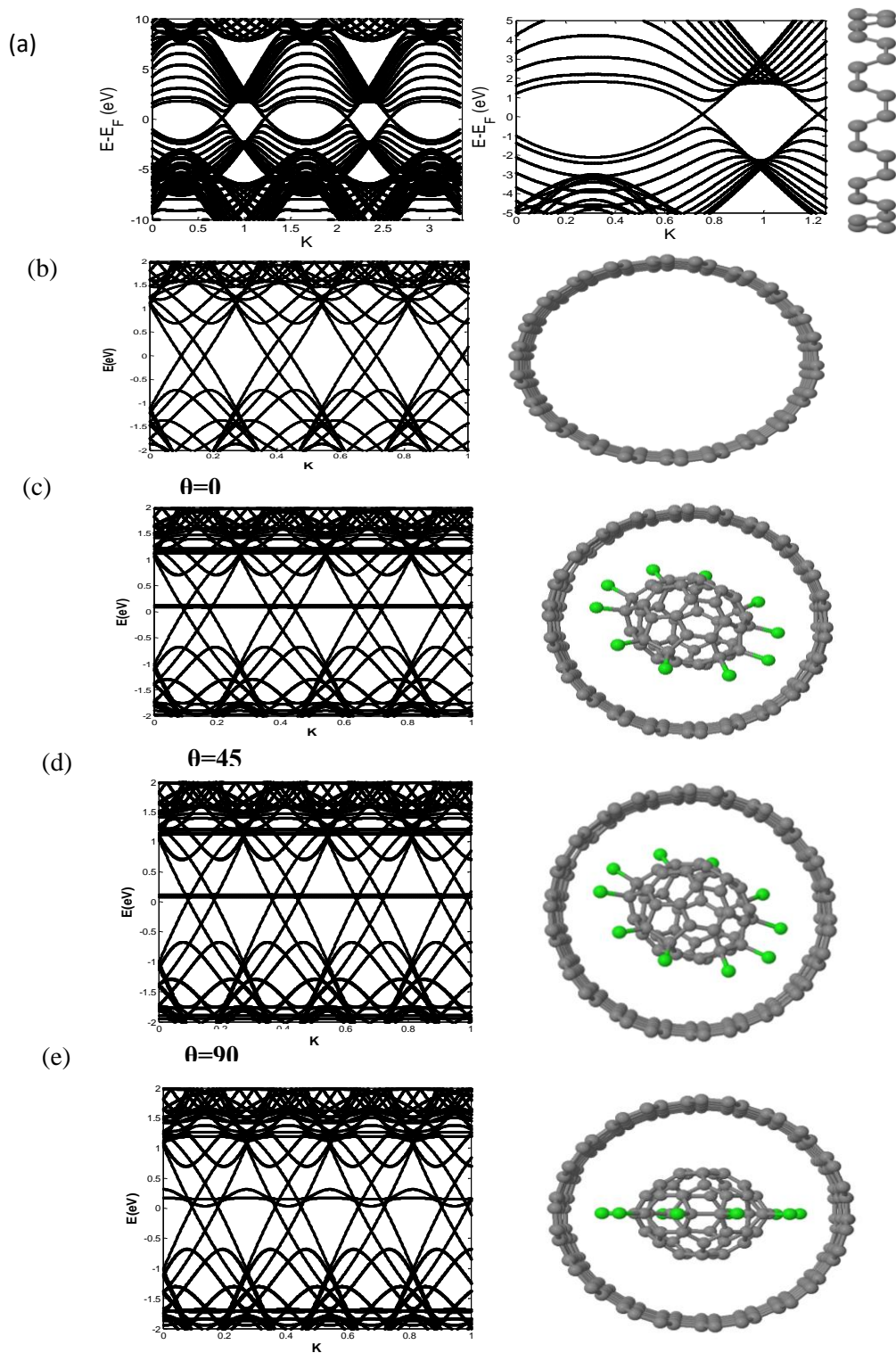
Figure 6.7 *The band structure of CNT (11,11) unit cell, CNT(11,11) bare and C₅₀Cl₁₀ within CNT(11,11) at different angles θ= 0,45,90.*

Transmission
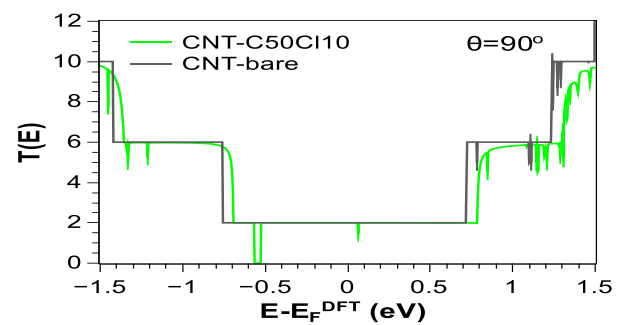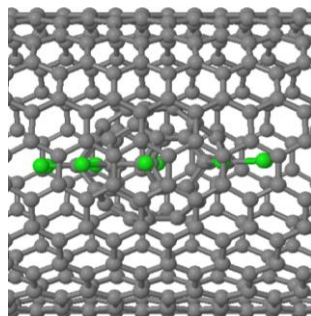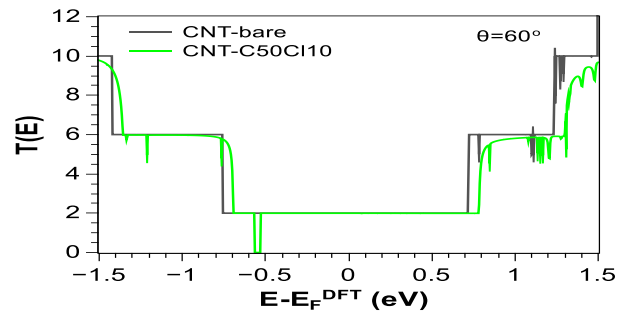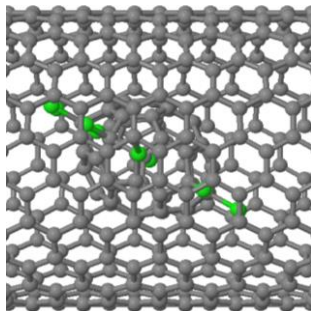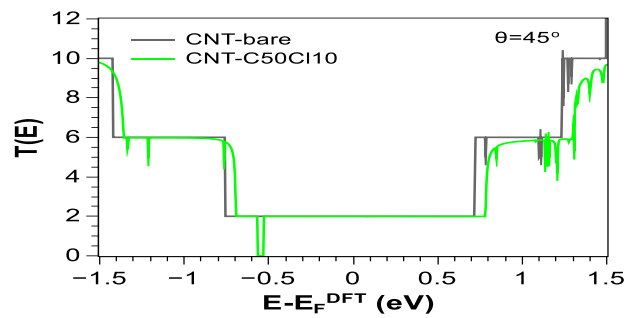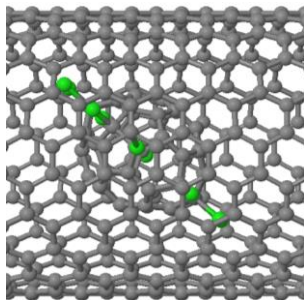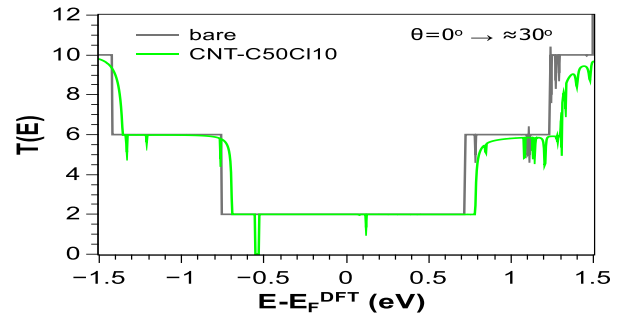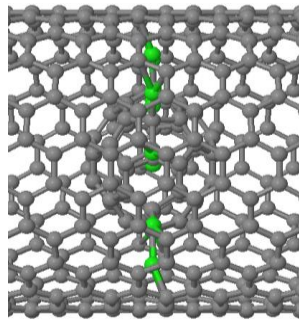
Figure 6.8 Transmission coefficient and open channel for C_{50}Cl_{10} within CNT (11,11) at θ= 0-90 with their angles change before and after relaxation

Transmission and open channels
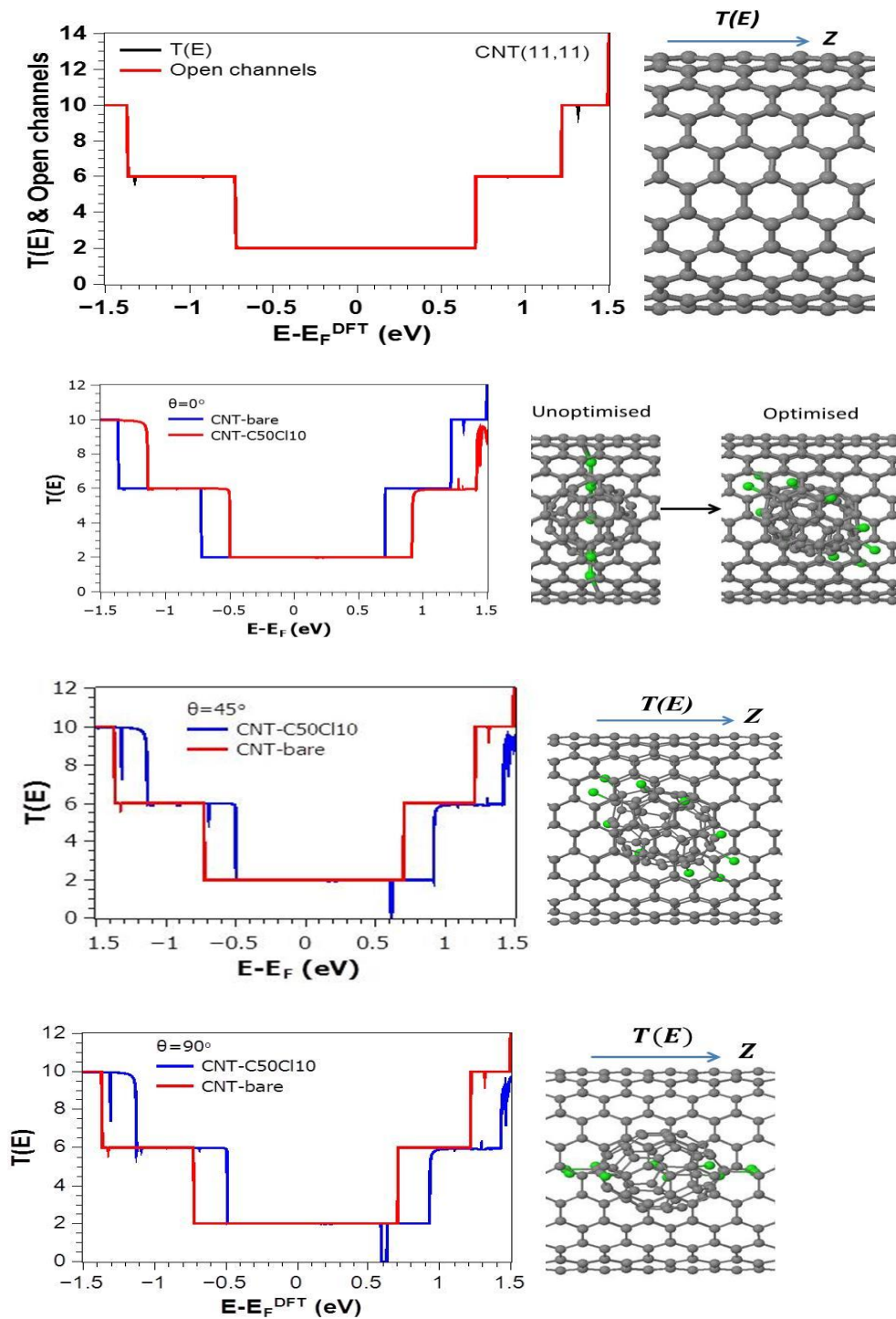
Figure 6.9 *(right) Geometry of a CNT (11,11) bare and C50Cl10 @ CNT (11,11) in angles θ= 0, 45 and 90 (left) Zero bias transmission coefficient T(E) and open channel after relax.*

Transmission and open channels for long CNT

Bare CNT(11,11)-conductor

(a)

CNT(11,11)-conductor

(b)
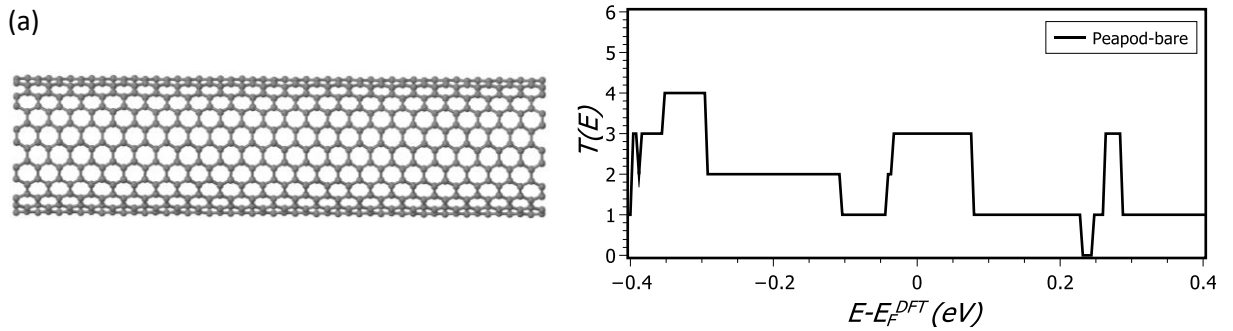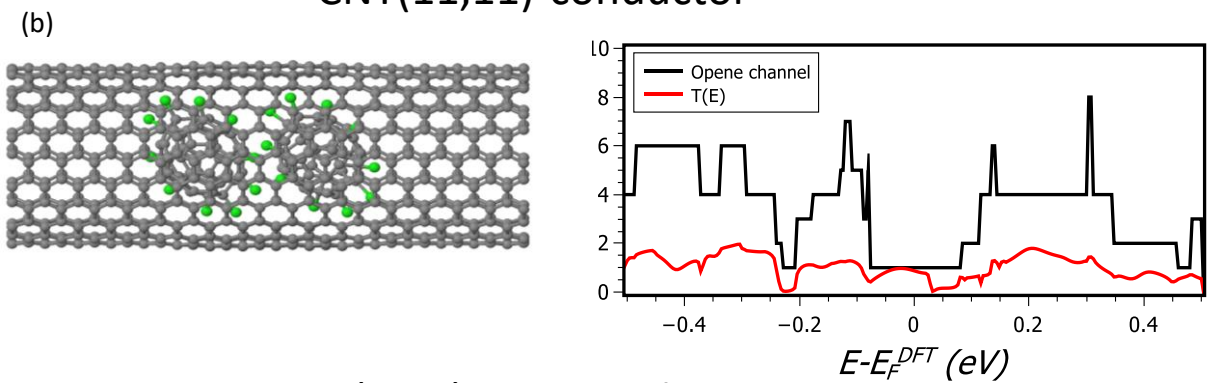
CNT(22,0)-Semiconductor

(c)
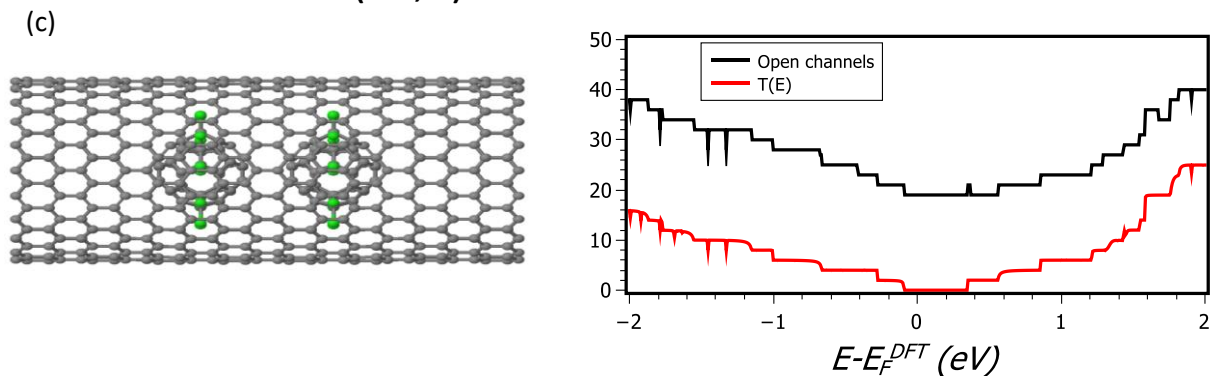
Figure 6.10 *(up) Geometry of a CNT (11,11) bare and dimer C50Cl10 within CNT in conductor and semiconductor CNT (down) Zero bias transmission coefficient T(E) and open channel after*

Thermoelectric Properties
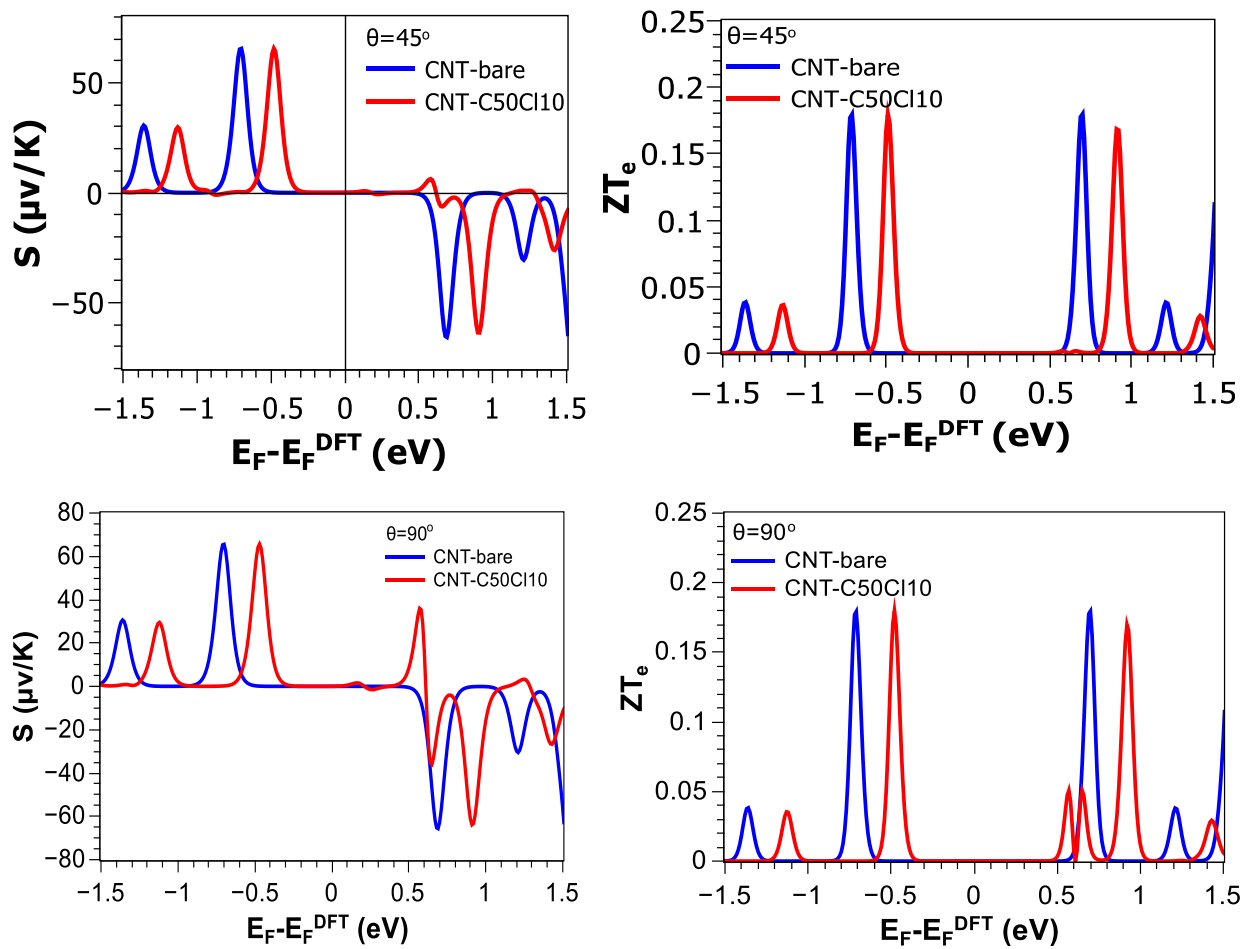
Figure 6.11 *the room temperature thermopower S and the figure of merit ZT and their results*

using different values of E_F.